

A Thesis Submitted for the Degree of PhD at the University of Warwick

Permanent WRAP URL:

<http://wrap.warwick.ac.uk/149154>

Copyright and reuse:

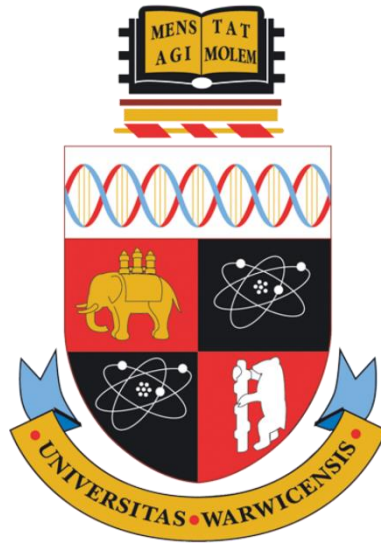
This thesis is made available online and is protected by original copyright.

Please scroll down to view the document itself.

Please refer to the repository record for this item for information to help you to cite it.

Our policy information is available from the repository home page.

For more information, please contact the WRAP Team at: wrap@warwick.ac.uk



Recyclability of aluminium and aluminium alloys

James Mathew

A thesis submitted in the fulfilment of the requirements for the degree of

Doctor of Philosophy in Engineering

University of Warwick

Warwick Manufacturing Group

August 2020

Table of Contents

Table of Contents	2
Acknowledgement	5
Declarations	7
Published work.....	8
Abstract	9
List of Symbols and Abbreviations	11
List of Tables.....	13
List of Figures	14
Chapter 1 . Introduction.....	21
1.1 Background and Challenges	21
1.2 Motivation.....	22
1.2 Research Objectives	23
Chapter 2 . Literature review	24
2.1 Importance of Aluminium recycling	24
2.2 Major problems in recycling.....	25
2.3 Iron based intermetallic particles.....	25
2.3.1 Pure aluminium.....	26
2.3.2 Aluminium-silicon alloys	27
2.4 Mechanism of formation of β -phase iron intermetallic particles.....	30
2.4.1 Reactions leading to the formation of intermetallics.....	31
2.5 Effect of cooling rate and concentration of Fe and Si in the formation of iron based intermetallic particles	32
2.6 Effect of melt treatments in the formation of iron based intermetallic particles	34
2.7 Effect of heat treatment on the microstructural changes of aluminium alloys containing iron based intermetallic particles.....	35

2.8 Effect of iron based intermetallic particles in the castability of aluminium alloys	36
2.9 Effect of superheating in the iron based intermetallic particles in aluminium alloys.....	37
2.10 Effect of iron based intermetallic particles in the mechanical properties of aluminium alloys.....	38
2.11 Chemical modification of iron based intermetallic particles	40
Chapter 3 . Research Methodology	46
3.1 Research Outline	46
3.2 Samples under investigation	46
3.3 Experimental procedure-preparing the cast alloys	47
3.3.1 Chemical modification	48
3.3.2 Vacuum induction melting (VIM).....	49
3.4 Microstructure Analysis.....	49
3.4.1 Sample Preparation for Microstructure Analysis	49
3.4.2 Optical Microscopy	50
3.4.3 Scanning electron microscope (SEM)	51
3.4.4 Three Dimensional FIB-SEM.....	51
3.4.5 Transmission electron microscopy (TEM).....	52
3.4.6 Three Dimensional X-ray computed tomography	53
3.5 Differential scanning calorimetry (DSC)	54
3.6 Mechanical property analysis.....	55
3.6.1 Nano-indentation.....	55
3.6.2 Mechanical Property Characterisation	56
Chapter 4 . Effect of silicon and iron concentration in the formation and growth of iron intermetallic particles	59
4.1 Prediction of phase formation using Thermo-Calc	59
4.2 Microstructural studies	61
4.3 Mechanical properties.....	67
4.4 Fracture surface analysis	68
Chapter 5 . Mechanism behind the failure of Al-Si alloys due to the iron intermetallic particles.....	71
5.1 Microstructure Analysis.....	71

5.2 Mechanical properties.....	73
5.3 Fracture surface analysis	76
5.4 X-ray tomography studies	77
Chapter 6 . Effect of melt treatments in the formation and growth of iron intermetallic particles	81
6.1 Effect of cooling rate on the microstructure and mechanical properties of Al-Fe and Al-7Si-Fe alloys.....	81
6.1.1 Optical microscopy	82
6.1.2 Mechanical properties	84
6.2 Effect of superheat on the microstructure and mechanical properties of Al-7Si-2Fe alloy.....	87
6.2.1 Microstructure Analysis	87
6.2.1 Three Dimensional X-ray computed tomography	92
6.2.2 Mechanical property analysis	98
6.3 Vacuum induction casting of aluminium alloys.....	100
6.3.1 Optical microscopy	100
6.3.2 Mechanical property analysis	105
Chapter 7 . Chemical modification of iron intermetallic particles in aluminium alloy	108
7.1 Effect of manganese and strontium on iron intermetallic particles in Al alloy	108
7.1.1 Microstructure analysis	108
7.1.2 3-dimensional FIB-SEM studies	117
7.2 Effect of Lanthanum addition on iron intermetallic particles in Al alloy	118
7.2.1 Microstructure Analysis of Al-Fe-La alloys.....	119
7.2.2 3-dimensional FIB-SEM studies of Al-Fe-La alloy.....	122
7.2.3 Mechanical properties of Al-Fe-La.....	126
Chapter 8 . Conclusion and suggestions for future work.....	132
8.1 Conclusions.....	132
8.1.1 Major findings.....	133
8.2 Suggestions for future work	134
References.....	136

Acknowledgement

It is my obligation to take this opportunity to express my deep gratitude to the incredible people who have helped to sail through my PhD journey with all sorts of patience and immense support. Without your care and encouragement I would not have achieved this mile stone. Above all I thank God Almighty for being there with me and guiding me through all the hardships and obstacles.

Firstly, I would like to convey my sincere gratitude to my supervisor, Dr Prakash Srirangam for his continuous support throughout the process of research with his patience, motivation and substantial knowledge. Your unlimited enthusiasm and zeal have guided me throughout my PhD life. Your moral support as well as advices all the way encouraged me to enjoy the work and push my limits.

I would like to thank my co-supervisors Professor Mark. A. Williams and Dr Greg Gibbons for their extensive concern and encouragement in completing this PhD work.

I would also like to express my heartfelt regards to all my colleagues and staff in AMMC, all the technicians and staff in IMC workshop, Metallography and Microscopy labs, WMG IT Services, WMG Facilities, WMG Finance and HR, for providing me a smooth work environment and all the timely supports.

I would like to thank my PhD reviewer Professor Barbara Shollock for her valuable suggestions, insightful comments, corrections in upgrade report and generous support with catapult money for the purchase of project materials.

I gratefully acknowledge the undergraduate students Bolaji Akinola-Alli and Ed Jones for helping me in my experiments.

I am particularly thankful to all my friends and housemates for stimulating and encouraging me whenever I felt low.

Last of all, I would like to thank my grandparents, parents, brothers and relatives, who have consistently been there for me and supported me. Papa and Amma I know

it was my responsibility to stay with you at all the hard times of your life and I am sorry couldn't do much. Thank you for all the sacrifices, support and care you have given me throughout these years. To my brothers and cousins, thanks for all your support and love. I promise I will compensate for all those days we missed. Thanks to my wife Pooja and to my new-born baby Janae, you showered your invincible love towards me always without any hesitance. I am also thankful to my in laws who stood with me, with great care and prayers. I have no valuable words to express my thanks, but my heart is full of the favours received from each and every one.

Declarations

I, James Mathew, confirm that the work presented in this thesis is my own. It has been written and compiled by myself and has not been submitted anywhere else. The work in this thesis has been undertaken by me except where otherwise stated.

James Mathew

August 2020.

Published work

Mathew James, Guillaume Remy, Mark A. Williams, Fengzai Tang, and Prakash Srirangam. "Effect of Fe intermetallics on microstructure and properties of Al-7Si alloys." JOM (2019): 1-8.

Mathew, James, and Prakash Srirangam. "The effect of Manganese and Strontium on Iron intermetallics in recycled Al-7% Si alloy." Light Metals 2019. Springer, Cham, 2019. 235-240.

Manuscripts in preparation:

James Mathew, Fengzai Tang, Geoff West and Prakash Srirangam. "On the formation and growth of Iron intermetallic phases in Aluminium in presence of Lanthanum."

Mathew, James, and Prakash Srirangam. "Effect of superheating in the formation of Iron intermetallic particles and mechanical properties of Al-7Si alloy."

Abstract

Aluminium and aluminium silicon alloys are widely used materials for the automobile, structural and aerospace applications due to its effective weight reduction compared to other materials. The increase in demand of cast aluminium alloys and the surge in aluminium waste scraps leads to the secondary production/recycling of aluminium waste scraps. The total production cost and energy usage required for the production of primary Al from the bauxite ores is high compared to the secondary production of aluminium. One of the major concerns in aluminium recycling is the detrimental effect of iron impurities which generally cannot be removed completely by physical separation techniques. The iron in the scrap combines with other elements to form Fe-rich intermetallic compounds. The iron content should not exceed a particular level/critical iron content (Fe_{crit}) to prevent the weakening effects of Fe-rich intermetallic compounds. This critical iron content (Fe_{crit}) is different for different alloy compositions. Higher percent of iron presence beyond an optimum limit would result in deterioration of mechanical property of the alloys.

In this work, pure aluminum, aluminium-7 wt% silicon and aluminium-12 wt% silicon alloys were studied using 0 wt% , 0.6 wt% (Fe_{crit} of Al-7Si) and 2 wt% Fe cast at 740°C for understanding the effect of silicon and iron content in the formation of intermetallic particles. The increase in iron content and silicon content increases the thickness and quantity of iron intermetallic particles formed. The microstructure and mechanical properties of these alloys were studied to understand the mechanism behind the failure of these alloys and to mitigate its deteriorating effects by suitable modification methods. Because of its sharp edged platelet morphology, the brittle iron intermetallic compounds act as stress raisers, help in crack propagation and deteriorate the mechanical properties of the cast. Hence the effective methods of modification of these iron intermetallic particles in order to reduce its weakening effects are either by refining them or by changing its morphology. The melt treatment processes such as varying cooling rates and superheat is found to refine these intermetallic particles. The effect of cooling rate is studied with a water cooled copper wedge mold, cast iron mold and a graphite mold. Even though high cooling rate refines the particles and grain size compared to the low cooling rates, the mechanical properties of Al-7Si alloy with high iron content (2%) is still significantly low compared to the low iron content (0.6%). Therefore the superheat effect on Al-7Si-2Fe alloys were studied using the alloy samples prepared at 700°C, 800°C and 900°C. The microstructure studies using optical microscopy, SEM-EDS and XCT confirmed the refinement of intermetallic phases in Al-7Si-2Fe alloys upon superheating at 900°C compared to the 700°C and 800°C. But the porosity is more for 900°C cast compared to 700°C cast, which results in reduced mechanical properties for 900°C cast compared to 700°C cast.

The most commonly used economically and industrially viable modification method of iron intermetallic particles is by the addition of chemicals/elements which can react with the Al, Si and Fe phases. In this work one of the rarely studied rare earth element, lanthanum, is used for the modification of iron intermetallic particles in Al-Fe and Al-7Si-Fe alloys. Lanthanum is found to form $La(AlSi)_2$ and $Al_{11}La_3$ phases prior to the formation of iron intermetallic phases during solidification. The addition of 1%

of La to the Al-2Fe alloy resulted in the refinement of iron intermetallic particles along with the formation of Al-La based particles. The SEM-EDS, TEM-EDS and TEM-SAD patterns identified the particles in Al-2Fe alloy as $\text{Al}_{13}\text{Fe}_4$ and the particles in Al-2Fe-1La alloy as Al_5Fe_2 and $\text{Al}_{11}\text{La}_3$. The 3D FIB-SEM images shows the morphological modification of iron intermetallic particles by preventing the formation of platelet shaped $\text{Al}_{13}\text{Fe}_4$ phase from Al_5Fe_2 phase after the addition of lanthanum. This helps in improving the mechanical properties of Al-2Fe alloy. Further, the addition of 1% La to the Al-7Si-Fe alloy resulted in the refinement of silicon particles and thereby improves the mechanical properties. The mechanism of modification of iron intermetallic particles on addition of lanthanum is explained based on the intermetallic phase formation sequence in low silicon and high silicon aluminium alloys and found that addition of lanthanum cannot modify the iron intermetallic particles in high silicon Al-Si alloys. The modification of iron intermetallic particles using Mn and Sr addition to Al-Si alloys were studied to understand its limits and found the formation of large sharp edged brittle $\alpha\text{-AlFeMnSi}$ particles at higher fractions of iron content (2%) which culminates the modification effect.

List of Symbols and Abbreviations

Symbol	Definition
Al	Aluminium
Fe	Iron
wt%	Weight percentage
Si	Silicon
β	Beta phase
α	Alpha phase
θ	Theta phase
η	Eta phase
γ	Gamma phase
δ	Delta phase
$^{\circ}\text{C}$	Degree Celsius
XCT	X-ray compute tomography
SEM	Scanning Electron Microscope
HRTEM	High Resolution Transmission Electron Microscope
DSC	Differential Scanning Calorimetry
FIB	Focussed Ion Beam
EDS	Energy-Dispersive Spectroscopy
2D	Two-Dimensional
3D	Three-Dimensional
Cu	Copper
Mg	Magnesium
Mn	Manganese

Sr	Strontium
La	Lanthanum
ASTM	American Society for Testing and Materials
ppm	parts per million
MPa	Mega Pascal
kg	Kilogram
MJ	Mega joules
bct	body-centered tetragonal
Fe _{crit}	Critical iron content
K/s	Kelvin per second
μm	Micrometre
mm	Millimetre
nm	Nanometre
N	Newton
Cr	Chromium
Be	Beryllium
Co	Cobalt
Mo	Molybdenum
Ni	Nickel
Ce	Cerium
Nd	Neodymium
RE	Rare earth
SAD	Selected Area Diffraction

List of Tables

Table 2.1 Crystallographic data of the identified iron intermetallic particles in aluminium and aluminium silicon alloys.....	26
Table 3.1 Elemental composition analysis of master alloys(wt%).....	47
Table 3.2 Polishing procedure.....	50
Table 3.3 X-ray tomography scanning parameters.....	54
Table 3.4 Chemical composition of alloys prepared (wt%)	58
Table 4.1 Solidification sequence/microstructure evolution of aluminium and aluminium silicon alloys upon cooling from liquid state	60
Table 7.1 Phase identification from spectrum data.....	111

List of Figures

Figure 2.1 Optical micrograph showing iron intermetallics in Al-1Fe alloy [23].	27
Figure 2.2 Microstructure of common iron intermetallic particles in Aluminium-silicon alloys, arrows showing their typical morphologies (a) β -Al ₅ FeSi needles, (b) script-like α -Al ₈ Fe ₂ Si[24].	28
Figure 2.3 Three Dimensional reconstructed image of a group of β -Al ₅ FeSi intermetallic platelets[25].	29
Figure 2.4 (a) Photomicrograph showing nucleation of the β -AlFeSi platelets on the oxide particles. (b) Sympathetic nucleation (branching) of β -Al ₅ FeSi platelets on the surface of already formed β -Al ₅ FeSi platelets[28].	30
Figure 2.5 Cooling curve (Temperature vs. time) and cooling rate curve (dT/dt vs. time) for an Al-9Si-3Cu-0.5Mg-1.0Fe alloy. The labels in the peaks are the following reactions: (1) Primary aluminium dendrites, (2) β -Al ₅ FeSi, (3) Al-Si eutectic, (4) complex Mg ₂ Si eutectic, (5) Al ₂ Cu eutectic[36].	33
Figure 2.6 Microstructures of Al-2Fe alloy (a) without melt treatment (b) with melt treatment[22].	35
Figure 2.7 Shrinkage porosity in a cylindrical casting of Al-Si-Cu-Mg alloy with iron levels (a) 0.1% iron, (b) 1.0% iron[24].	37
Figure 2.8 Microstructure showing the intermetallic particles in Al-Si alloy with an iron content of 1.94% (a) 710°C, (b)1000°C[50].	38
Figure 2.9 Simplified liquidus projection of the ternary Al-Si-Fe system for Al-Si alloys with critical iron levels[24].	39
Figure 3.1 Mould for casting (a) water cooled wedge copper mould, (b) cast iron mould (c) clay graphite crucible mould.	48
Figure 3.2 Schematic representation of a loading-unloading curve[79]	56

Figure 3.3 Tensile testing sample prepared as per ASTM E-8M[83].....	57
Figure 4.1 ThermoCalc plots showing the expected phases in equilibrium conditions, (a) Al-Si alloy with 0.6 wt% Fe, (b) Al-Si alloy with 2 wt% Fe.	61
Figure 4.2 Optical microstructure of (a) Al-0.6Fe, (b) Al-2Fe.....	62
Figure 4.3 Optical microstructure of (a) Al-7Si-0.6Fe, (b) Al-7Si-2Fe.....	62
Figure 4.4 Optical microstructure of (a) Al-12Si-0.6Fe, (b) Al-12Si-2Fe.....	63
Figure 4.5 SEM images of (a) Al-0.6Fe, (b) Al-2Fe.....	63
Figure 4.6 SEM images of (a) Al-7Si-0.6Fe, (b) Al-7Si-2Fe.....	64
Figure 4.7 SEM images of (a) Al-12Si-0.6Fe, (b) Al-12Si-2Fe.....	64
Figure 4.8 EDS elemental mapping of Al-0.6Fe (violet colour represents distribution of aluminium and the green colour represents distribution of iron).	65
Figure 4.9 EDS elemental mapping of Al-2Fe (violet colour represents distribution of aluminium and the green colour represents distribution of iron).	65
Figure 4.10 EDS elemental mapping of Al-7Si-0.6Fe (violet colour represents distribution of aluminium, the yellow colour represents distribution of silicon and the green colour represents distribution of iron).	66
Figure 4.11 EDS elemental mapping of Al-7Si-2Fe (violet colour represents distribution of aluminium, the yellow colour represents distribution of silicon and the green colour represents distribution of iron).	66
Figure 4.12 EDS elemental mapping of Al-12Si-0.6Fe (violet colour represents distribution of aluminium, the yellow colour represents distribution of silicon and the green colour represents distribution of iron).	66
Figure 4.13 EDS elemental mapping of Al-12Si-2Fe (violet colour represents distribution of aluminium, the yellow colour represents distribution of silicon and the green colour represents distribution of iron).	67

Figure 4.14 Tensile stress vs strain curve of aluminium alloys with different iron and silicon contents	68
Figure 4.15 SEM image showing the fracture surface of (a) Al-0.6Fe (b) Al-2Fe (c) Al-7Si-0.6Fe (d) Al-7Si-2Fe (e) Al-12Si-0.6Fe (f) Al-12Si-2Fe alloy.	69
Figure 5.1 SEM images of (a) Al-7Si, (b) Al-7Si-0.6Fe and (c) Al-7Si-2Fe alloys	71
Figure 5.2 SEM-EDS elemental mapping of (a) Al-7% Si alloy, (b) Al-7% Si-0.6% Fe alloy and (c) Al-7% Si-2% Fe alloy (green colour represents aluminium matrix, yellow colour represents the silicon phase and blue colour represents iron)	72
Figure 5.3 Loading – Unloading curve of Al-7Si-2Fe alloy.....	74
Figure 5.4 Tensile properties, Tensile stress vs strain of Al-7Si with different iron content.	76
Figure 5.5 Fracture surface of (a) Al-7Si, and (b) Al-7Si-2Fe alloys.....	77
Figure 5.6 2D slices showing the crack propagation (top to centre of the fracture region)	78
Figure 5.7 3D reconstructed XCT images (a) showing porosity (blue colour) as well as particles (red colour) in Al matrix (white), (b) showing particles (red colour) in Al matrix (white).....	79
Figure 6.1 Microstructure of Al-0.6Fe alloy cast in (a) watercooled copper mould (b) cast iron mold (c) graphite mould.....	82
Figure 6.2 Microstructure of Al-2Fe alloy cast in (a) watercooled copper mould (b) cast iron mold (c) graphite mould.....	83
Figure 6.3 Microstructure of Al-7Si-0.6Fe alloy cast in (a) watercooled copper mould (b) cast iron mold (c) graphite mould	83
Figure 6.4 Microstructure of Al-7Si-2Fe alloy cast in (a) water cooled copper mould (b) cast iron mold (c) graphite mould	84

Figure 6.5 Tensile stress vs Strain curve of aluminium alloys with different cooling rate	86
Figure 6.6 Microstructure of alloys cast with a melt temperature of 700°C (a) Al-7Si (b) Al-7Si-2Fe	87
Figure 6.7 Microstructure of alloys cast with a melt temperature of 800°C (a) Al-7Si (b) Al-7Si-2Fe	88
Figure 6.8 Microstructure of alloys cast with a melt temperature of 900°C (a) Al-7Si (b) Al-7Si-2Fe	88
Figure 6.9 SEM elemental analysis of Al-7Si alloy cast with a melt temperature of 700°C (red colour shows the distribution of aluminium, the green colour shows the distribution of silicon).	89
Figure 6.10 SEM elemental analysis of Al-7Si alloy cast with a melt temperature of 800°C (red colour shows the distribution of aluminium, the green colour shows the distribution of silicon).	89
Figure 6.11 SEM elemental analysis of Al-7Si alloy cast with a melt temperature of 900°C (red colour shows the distribution of aluminium, the green colour shows the distribution of silicon).	90
Figure 6.12 SEM elemental analysis of Al-7Si-2Fe alloy cast with a melt temperature of 700°C (red colour shows the distribution of aluminium, the green colour shows the distribution of silicon, the blue colour shows the distribution of iron).....	91
Figure 6.13 SEM elemental analysis of Al-7Si-2Fe alloy cast with a melt temperature of 800°C (red colour shows the distribution of aluminium, the green colour shows the distribution of silicon, the blue colour shows the distribution of iron).....	91
Figure 6.14 SEM elemental analysis of Al-7Si-2Fe alloy cast with a melt temperature of 900°C (red colour shows the distribution of aluminium, the green colour shows the distribution of silicon, the blue colour shows the distribution of iron).....	91

Figure 6.15 3D reconstructed x-ray CT images of Al-7Si alloys cast at (a) 700°C and (b) 900°C.....	93
Figure 6.16 3D reconstructed x-ray CT images of Al-7Si-2Fe alloys cast at (a) 700°C and (b) 900°C.....	94
Figure 6.17 Particle distribution in Al-7Si-2Fe alloys cast at 700°C and 900°C.....	95
Figure 6.18 3D reconstructed x-ray CT images of (a) Al-7Si alloy cast from melt of 700°C (b) Al-7Si alloy cast from melt of 900°C (c) Al-7Si-2Fe alloy cast melt of 700°C (d) Al-7Si-2Fe alloy cast from melt of 900°C.	96
Figure 6.19 Porosity distribution of Al-Si and Al-Si-Fe alloys.....	97
Figure 6.20 Tensile stress vs strain curve on tensile loading of Al-Si and Al-Si-Fe alloys	98
Figure 6.21 DSC curve for Al-7Si-2Fe alloys cast at 700°C and 900°C.....	99
Figure 6.22 Optical microstructure of Al-7Si alloys cast at (a) 700°C (b) 900°C	101
Figure 6.23 Optical microstructure of Al-7Si-2Fe alloys cast at (a) 700°C and (b) 900°C	101
Figure 6.24 3D reconstructed CT images of vacuum cast Al-7Si alloy at (a) 700°C (b) 900°C and Al-7Si-2Fe alloy at (c) 700°C (d) 900°C.....	102
Figure 6.25 3D reconstructed CT images of porosities in Al-7Si alloy at cast in vacuum atmosphere at (a) 700°C (b) 900°C and Al-7Si-2Fe alloy at (c) 700°C (d) 900°C (approximate size of the cuboid is 9.5 mm x 6.0 mm x 7.0 mm).....	103
Figure 6.26 Pore size distribution of vacuum cast Al-Si and Al-Si-Fe alloys.....	104
Figure 6.27 Tensile stress vs strain curve on tensile loading of vacuum cast Al-7Si and Al-7Si-2Fe alloys	106
Figure 7.1 SEM images of (a) Al-7Si-1Fe (b) Al-7Si-1Fe-0.5Mn (c) Al-7Si-1Fe-0.5Mn-400ppmSr	109

Figure 7.2 SEM images of (a) Al-7Si-2Fe (b) Al-7Si-2Fe-1Mn (c) Al-7Si-2Fe-1Mn-400ppmSr	109
Figure 7.3 Intermetallic compounds identified through EDS analysis	110
Figure 7.4 Plot showing frequency(%) vs average particle size of (a) Al-7Si-1Fe (b) Al-7Si-2Fe	112
Figure 7.5 Plot showing number of pores vs average pore size of (a) Al-7Si-1Fe (b) Al-7Si-2Fe	114
Figure 7.6 SEM-EDS elemental mapping of Al-1Fe-0.5Mn (orange colour represents distribution of Al, green colour represents distribution Fe, and blue colour represents distribution of Mn).....	115
Figure 7.7 SEM-EDS elemental mapping of Al-2Fe-1Mn (orange colour represents distribution of Al, green colour represents distribution Fe, and blue colour represents distribution of Mn).....	115
Figure 7.8 SEM-EDS elemental mapping of Al-2Fe-1Mn-400ppm Sr (orange colour represents distribution of Al, green colour represents distribution Fe, yellow colour represents Sr and blue colour represents distribution of Mn).....	116
Figure 7.9 SEM-EDS elemental mapping of Al-7Si-1Fe-0.5Mn-400ppm Sr (orange colour represents distribution of Al, green colour represents distribution Fe, violet colour represents Si, yellow colour represents Sr and blue colour represents distribution of Mn).....	116
Figure 7.10 SEM-EDS elemental mapping of Al-7Si-2Fe-1Mn-400ppm Sr (orange colour represents Al, green colour represents Fe, violet colour represents Si, yellow colour represents Sr and the blue colour represents Mn).	117
Figure 7.11 3D reconstructed image of (a) Al-7Si-2Fe-1Mn-400ppmSr alloy (b) α phase iron intermetallic distribution in Al-7Si-2Fe-1Mn-400 ppm Sr alloy (c) α phase iron intermetallic particles.	118
Figure 7.12 SEM-EDS images of (a) Al-0.6Fe, (b) Al-2Fe, (c) Al-2Fe-1La	119

Figure 7.13 SEM-EDS elemental mapping of Al-2Fe (Red colour represents Al and green colour represents the Fe).	120
Figure 7.14 SEM-EDS elemental mapping of Al-2Fe-1La (Red colour represents Al, blue colour represents La and green colour represents Fe).....	120
Figure 7.15 SEM-EDS elemental mapping of Al-2Fe-1La (a) aluminium, (b) iron, (c) lanthanum.....	120
Figure 7.16 TEM bright field images of (a) Al-2Fe alloy (b) Al-2Fe-1La alloy, (c) TEM-EDS image from Al-2Fe-1La alloy (rectangular area in Figure b), TEM SAD of (d) $Al_{13}Fe_4$ in Al-2Fe alloy (Marked location in Figure a), (e) Al_5Fe_2 in Al-2Fe-1La alloy (Marked location in Figure b) and (f) $Al_{11}La_3$ in Al-2Fe-1La alloy (Marked location in Figure b).	122
Figure 7.17 3D reconstructed image of (a) Al-2Fe, (b) Al-2Fe-1La (c) iron intermetallic distribution in Al-2Fe, (d) iron intermetallic distribution in Al-2Fe-1La (e) $Al_{11}La_3$ particles distribution in Al-2Fe-1La	123
Figure 7.18 ThermoCalc computed binary phase diagrams of a) the aluminium-rich side in the Al-Fe system, (b) the aluminium-rich side in the Al-La system.....	126
Figure 7.19 Tensile properties of Al-0.6Fe, Al-2Fe and Al-2Fe-1La alloys, Tensile stress vs strain.	127
Figure 7.20 Fracture surface of Al-2Fe and Al-2Fe-1La alloys.....	128
Figure 7.21 SEM-EDS elemental mapping of Al-7Si-0.6Fe-1La (red colour represents Al, green colour represents Fe, violet colour represents Si, and blue colour represents La.	129
Figure 7.22 SEM-EDS elemental mapping of Al-7Si-2Fe-1La (red colour represents Al, green colour represents Fe, violet colour represents Si, and blue colour represents La.	129
Figure 7.23 Tensile stress vs Strain curve of Al-7Si-La alloys	131

Chapter 1. Introduction

1.1 Background and Challenges

The demand for lightweight metals and alloys is increasing in automotive and aerospace applications to improve the fuel efficiency and to control the greenhouse gas emissions[1]. The major light weight alloys used as an alternative for cast iron in automobile components is cast aluminium and cast aluminium silicon alloys[2]. The main benefit of Al-Si alloys is along with its high strength to weight ratio, it has a good thermal conductivity[2]. This enables quicker extraction of combustion heat of the engine, compared to the cast iron. Aluminium and aluminium alloys are manufactured from both primary and recycled sources[3]. Recycling of aluminium and aluminium alloys are of importance considering the economic and environmental benefits involved. Primary production of aluminium and aluminium alloys requires an energy usage of about 186 MJ/kg of metallic aluminium; whereas this is 10–20 MJ/kg for recycling the aluminium scraps obtained after its primary usage[4]. This also helps in reducing the greenhouse emissions and solid waste accumulation compared to the primary production[4]. But, majority of the scraps for recycling is coming from the manufacturing, automobile and beverage industries[3]. Al scrap from these industries contain several impurity elements including iron[3]. Iron is generally considered as an impurity in aluminium and aluminium alloys because it causes casting defects and affects the mechanical properties[5]. These iron based components mixed with scrap are generally removed by physical separation techniques[6]. Since the molten aluminium is capable of dissolving iron, despite using these physical separation methods, the residual iron impurity results in the formation of intermetallic phases[4]. The intermetallic phases forms in pure aluminium and aluminium silicon alloys includes θ -phase, η -phase, δ -phase, γ -phase, β -phase and α -phase compounds[7,8]. Among those, θ -phase and β -phase compounds are brittle and appear as needles or platelet morphologies in the microstructure causes severe decrease in the ductility and other mechanical

properties of the casting[7]. Therefore instead of removing all the iron intermetallic particles, it could be made useful by finely dispersing uniformly or by converting to other phase compounds. Attempts have to be taken to eliminate the detrimental effects of the needle shaped iron intermetallic particles in recycled aluminium and aluminium silicon alloys.

1.2 Motivation

It is important to study the effect of iron based intermetallic particles in the aluminium alloys and different methods to control the size and shape of the intermetallic particles in the same. The type of intermetallic phase formed depends mainly on the cooling rate, melt superheat, amount of iron and the composition of the aluminium alloy. Melt treatment, chemical modification and post processing of the casting are the important methods that can control the size and shape of the iron intermetallic particles[6]. Some of the researchers have reported the nucleation of iron intermetallic particles on the surface of oxides. But there is not much research reported with superheating the melt in a vacuum atmosphere and casting with high cooling rates, which could reduce the detrimental effects considerably. Chemical modification of the iron intermetallic particles in aluminium and aluminium alloys is one of the modification technique which has industrial importance, since it is an economically viable process for the bulk recycling[3-6]. Studies have been reported with the addition of elements in particular strontium, calcium, scandium, manganese, titanium, boron etc. acts as a modifier for iron intermetallic particles in aluminium and aluminium alloys. The chemical modification technique involves the reaction of additive elements/compounds with the aluminium, silicon and iron phases. The morphological modification of iron intermetallic particles upon addition of these elements have to be studied broadly. Among these, there is not much of research carried out about the chemical modification of the iron intermetallic particles in pure aluminium and aluminium silicon alloys with the addition of rare-earth elements. Lanthanum is found to form $\text{La}(\text{AlSi})_2$ and $\text{Al}_{11}\text{La}_3$ phases prior to the formation of iron intermetallic phases during

solidification [9,10] of AlFeSiLa alloys. This could modify the iron intermetallic particles or reduce its detrimental effects.

1.2 Research Objectives

It is important to control the deleterious effects of iron intermetallic particles to increase the recycling of aluminium from the scraps containing higher iron contents. The objective of this project is to determine an economically and industrially viable modification method for reducing the detrimental effect of iron intermetallic particles. The chemical modification is a suitable technique which can be studied with different chemical additions to improve the morphology of iron intermetallic particles and mechanical properties of the alloy. Even though there are many theories explained on the effect of iron intermetallic particles in the failure of the aluminium alloys, the 3D fracture analysis is not studied to understand the failure mechanism. In order to control the harmful effects of intermetallic particles, it is necessary to understand the failure mechanism and the favourable melt conditions for the formation of intermetallic particles.

The main objectives of the present study are:

- To study the effect of lanthanum addition on the modification of iron intermetallic particles in aluminium and aluminium alloys.
- To study the effect of iron concentration and silicon concentration in aluminium by studying 3 different concentration of silicon (0%, 7% -hypo eutectic, 12%-near eutectic) in aluminium with 0.6% and 2% in iron.
- To study the effect of different melt treatment processes such as variable cooling rate and superheating on the formation and growth of iron intermetallic particles.
- To study the effect of iron intermetallic particle morphology in determining the mechanical properties of the aluminium alloys
- To study the effect of other chemical additions such as Mn and Sr in the modification of iron intermetallic particles and its limits.

Chapter 2. Literature review

Aluminium is one of the most widely used and bulky produced material in the automotive aerospace and structural applications. The growing demand for lightweight components leads to the substitution of the currently used materials with aluminium and aluminium alloys. It is important to study the recycling of aluminium in order to meet this growing demand as well as to reuse the scraps of old aluminium parts and reduce the solid waste build up.

This chapter covers the previous researches done on recycling of aluminium as well as strategies taken to improve the mechanical properties of aluminium and aluminium alloys containing impurities. One of the major impurity in the aluminium is iron and so is studied in detail about the iron impurities, its removal or modification methods.

2.1 Importance of Aluminium recycling

Total aluminium smelter production of the world reported by U.S geological survey is approximately 49,300 thousand metric tons in 2014. According to the survey, out of the 3.63 million tons of aluminium recovered from the purchased scrap by the United States in 2014, 53% came from new scrap and 47% from old scraps. That means the amount of recycled aluminium was about 47% of the total consumption. The aluminium recycled from old scraps is more than 50% of the total aluminium produced in the European Union (EU-25) [11]. Considering the amount of recycled aluminium in previous years, it is following an increasing trend.

Recycling of aluminium and aluminium alloys have several important environmental and economic benefits. In terms of energy usage on primary production and recycling, recycling of aluminium is beneficial. Total energy required for the primary production of aluminium from the bauxite ore is about 186 MJ/kg while, the total

energy required for the recycling of aluminium is about 10-20 MJ/kg. Despite of this economic benefit there is an underlying environmental importance for recycling of any material.

2.2 Major problems in recycling

Literature studies show that the major concern of the aluminium recycling industry is the presence of problematic impurities in the old scrap which comes from the manufacturing, automobile and beverage industries where aluminium is used with many other materials. Some of the major metallic impurities are silicon, magnesium, nickel, zinc, lead, chromium, iron, copper, vanadium and manganese[6]. There are a large number of ways to control these problematic impurities on recycling. Choosing a best method always depends on the optimum cost efficiency and improvement of the properties. Most common physical separation methods used for the separation of these particles are magnetic separation, air separation, eddy current separation, sink float/heavy media separation, hot crush, colour sorting and other spectrographic techniques[6]. But, the iron is soluble in the molten aluminium resulting in the formation of iron containing intermetallic particles and hence cannot be removed completely by any of the above physical separation techniques. These hard and brittle intermetallic phases act as stress raisers diminishing the mechanical properties and castability of recycled aluminium. Higher iron content can reduce the fluidity during casting resulting in an increase in shrinkage porosity[4].

2.3 Iron based intermetallic particles

Iron is soluble in the aluminium and it forms different types of intermetallic particles with or without combining other elements. These intermetallic phases are commonly classified/identified based on their characteristic shapes. Table 2.1 shows most of the identified iron intermetallic particles in aluminium and aluminium silicon alloys.

Table 2.1 Crystallographic data of the identified iron intermetallic particles in aluminium and aluminium silicon alloys

<i>Iron intermetallic particles</i>	Crystal structure	References
$\text{Al}_{4,4}\text{Fe}$	Bct	[12,13]
Al_6Fe	Orthorhombic	[13,14]
$\theta\text{-Al}_3\text{Fe}$ or $\theta\text{-Al}_{13}\text{Fe}_4$	Monoclinic	[13–15]
$\alpha\text{-Al}_8\text{Fe}_2\text{Si}$ or $\alpha\text{-Al}_{12}\text{Fe}_3\text{Si}_2$	Hexagonal	[13–16]
$\alpha\text{-Al}_{12}\text{Fe}_3\text{Si}$ or $\alpha\text{-Al}_{15}\text{Fe}_3\text{Si}$	Bcc	[14,16,17]
$\text{Al}_9\text{Fe}_2\text{Si}_2$	Monoclinic	[18]
$\beta\text{-Al}_5\text{FeSi}$	Monoclinic	[13,14]
Al_9FeSi	Monoclinic	[19]
$\delta\text{-Al}_4\text{FeSi}_2$	Tetragonal	[14,20]
$\delta\text{-Al}_3\text{FeSi}_2$	Bcc	[21]
AlFeSi	Monoclinic	[12]
$\gamma\text{-Al}_3\text{FeSi}$	Monoclinic	[12]
$\gamma\text{-Al}_8\text{FeSi}$	Monoclinic	[14]

2.3.1 Pure aluminium

In pure aluminium, major iron intermetallic phases were found to be Al_3Fe and Al_6Fe . Among these, Al_3Fe is θ phase which is acicular in shape with detrimental properties and Al_6Fe is granular in shape[22]. The maximum solid solubility of iron in aluminium is 0.04 % under equilibrium conditions. Al_3Fe phase has also been observed as $\text{Al}_{23}\text{Fe}_7$, $\text{Al}_{19}\text{Fe}_6$, $\text{Al}_{13}\text{Fe}_4$ phases. Figure 2.1 shows the optical micrographs of the Al_3Fe and Al_6Fe iron intermetallic particles in Al-1 wt% Fe alloy[23].

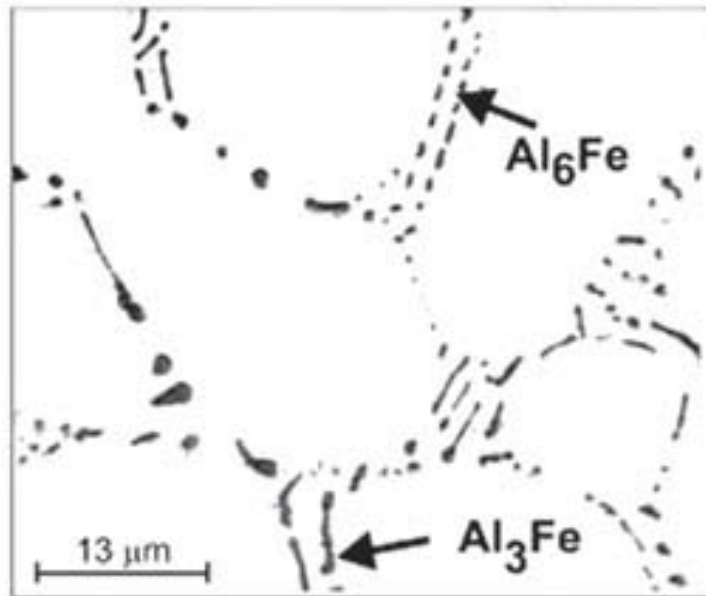


Figure 2.1 Optical micrograph showing iron intermetallics in Al-1Fe alloy [23].

2.3.2 Aluminium-silicon alloys

In aluminium silicon alloys, the major intermetallic phases formed with iron are α - $\text{Al}_8\text{Fe}_2\text{Si}$ and β - Al_5FeSi . α - $\text{Al}_8\text{Fe}_2\text{Si}$ phase is hexagonal shaped and β - Al_5FeSi phase is monoclinic shaped[24].

Some authors identified some other phases in aluminium silicon alloys. The other identified alpha phases are $\text{Al}_{12}\text{Fe}_3\text{Si}$ and α - AlFeSi . The β phases identified are Al_3FeSi_2 , Al_4FeSi , $\text{Al}_9\text{Fe}_2\text{Si}_2$, β - Al_5FeSi , Al_5FeSi , β - $\text{Al}_{4.5}\text{FeSi}$, and Fe_2SiAl_5 . These iron intermetallic forms differ in their shape and chemical properties, hence can be distinguished easily on microscopic studies with proper etching/EDS. α -phase is Chinese script-like morphology and β -phase is observed generally as needle like morphology. Figure 2.2 shows the 2 Dimensional morphology of the needle shaped β - Al_5FeSi and Chinese script shaped α - $\text{Al}_8\text{Fe}_2\text{Si}$ iron intermetallic particles in aluminium-silicon alloys[24]. However, on 3 Dimensional analysis later some of the researchers found that, actually the β -phase is platelet shaped which was misinterpreted as needle shape in 2 Dimensions. The detrimental properties

imparted by the β -phase intermetallic particles was considered to be because of its morphology.

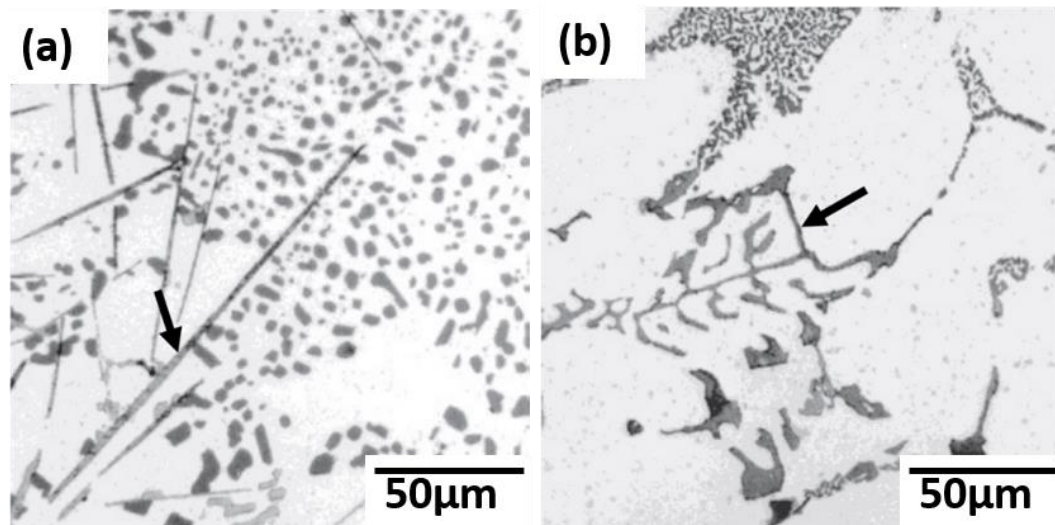


Figure 2.2 Microstructure of common iron intermetallic particles in Aluminium-silicon alloys, arrows showing their typical morphologies (a) β -Al₅FeSi needles, (b) script-like α -Al₈Fe₂Si[24].

The 3-Dimensional study of the β -phase iron intermetallic particles started very recently and only a very few literature is available. Dinnis et al.[25] used serial sectioning technique to create 3-dimensional view of β -Al₅FeSi. The 3D reconstructed image shows that the platelets were grown as an interconnected network around the pre-existing aluminium dendrite arms. A 3-dimensional study on Al-Si-Cu-Fe alloy using a synchrotron X-ray tomography identifies not all the platelets are networked and independent platelets were observed. Figure 2.3 shows the three dimensional image of a group of β -Al₅FeSi intermetallic platelets[25]. The solidification of the same alloy is studied 2-dimensionally in-situ and observed that the growth of intermetallic particles is more rapid in the initial stages of solidification[26]. Later the 3-dimensional in-situ study on the solidification of the Al-Si-Cu-Fe alloy[27] shows that the β -phase iron intermetallic particles nucleates near the surface oxide and grows due to the interaction with the primary aluminium dendrites. The growth of the β -phase is by branching of the platelets.

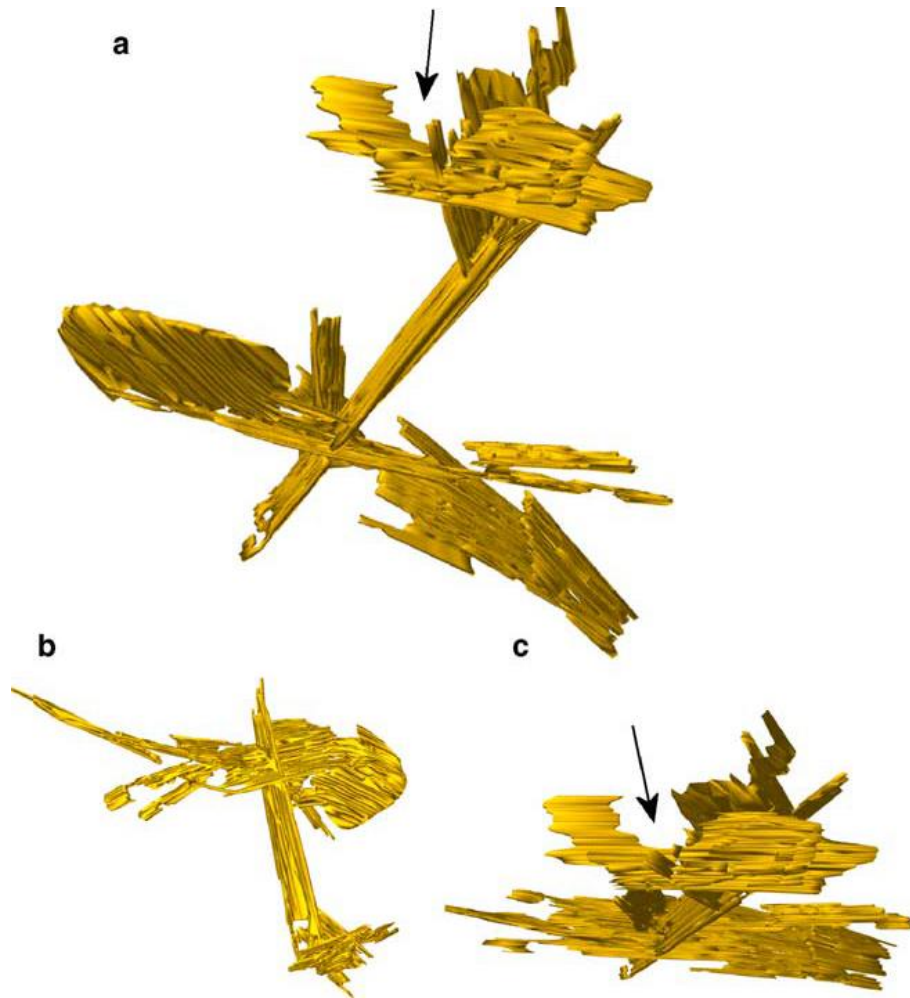


Figure 2.3 Three Dimensional reconstructed image of a group of β -Al₅FeSi intermetallic platelets[25].

2.4 Mechanism of formation of β -phase iron intermetallic particles

During solidification of the aluminium alloys with iron, the metastable γ -aluminium oxide particles act as nucleation sites for the primary β -phase iron intermetallic compounds. The formation of γ -aluminium oxide on the melt is generally accelerated at low superheat temperatures. The γ -aluminium oxide particle size range varies from submicron to few microns. If the melt is superheated to very high temperatures, the γ -aluminium oxide may transform to α -aluminium oxide decreasing the nucleation of β -phase iron intermetallic compounds. However if the cooling rate is low even with high superheat, γ -aluminium oxide can form which may increase the nucleation of β -phase iron intermetallic compounds[28]. Figure 2.4a, shows the nucleation of β -Al₅FeSi needles on a γ -aluminium oxide particle[28]. Samuel et.al [29] explained the mechanism of formation of secondary β -phase iron intermetallic compounds by sympathetic nucleation. That is, by branching out from the parent needle spanning across the matrix surface. The authors also concluded from the microstructure that the two needles are not occurring one above other but are branches, and appears so in the cross sectional view. Figure 2.4b, shows the sympathetic nucleation of β -Al₅FeSi platelets[29].

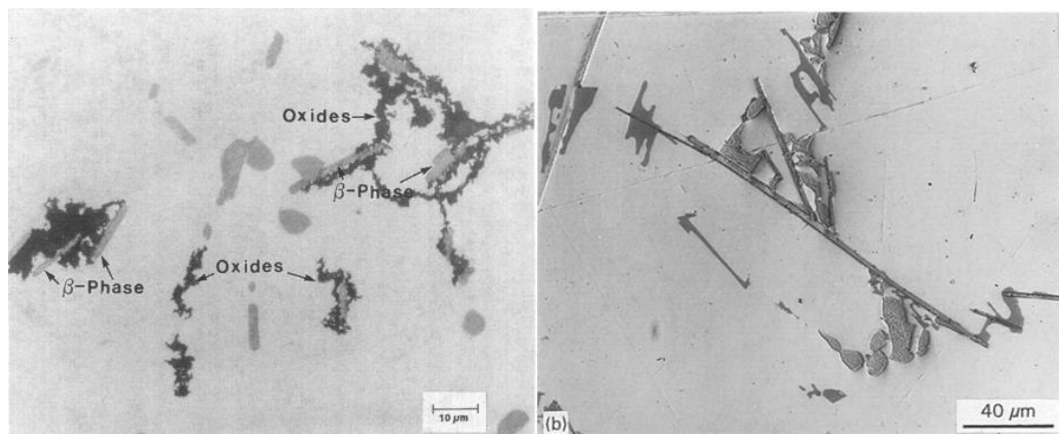
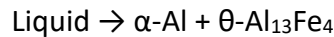


Figure 2.4 (a) Photomicrograph showing nucleation of the β -AlFeSi platelets on the oxide particles. (b) Sympathetic nucleation (branching) of β -Al₅FeSi platelets on the surface of already formed β -Al₅FeSi platelets[28].

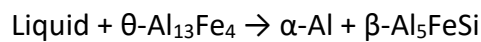
2.4.1 Reactions leading to the formation of intermetallics

There have been many attempts made to understand the reactions behind the formation of iron intermetallic phases through researches and hypothesis. Even though many of the solidification phases are identified along with the Al-Si-Fe phase diagram, there are some disagreements related to the temperature and nature of the reactions leading to the formation of various intermetallic phases. The major reactions reported in Al-Fe and Al-Si-Fe alloy systems are described below.

Allen et al.[30] reported the reaction upon studying the 1xxx aluminium alloy for the formation of θ -Al₁₃Fe₄ intermetallic particles.



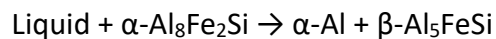
Sha et al.[31] reported the quasi-peritectic reaction resulting in the formation of β -Al₅FeSi intermetallic phase formation from θ -Al₁₃Fe₄ in 6xxx aluminium alloys (Al-0.6Si-0.8Mg-0.3Fe).



Backerud et al.[32] reported the reaction on the formation of Chinese script α -Al₈Fe₂Si intermetallic particles in the 6xxx aluminium alloys.



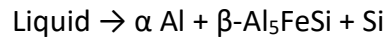
Mulazimoglu et al.[33] hypothesised that the β -Al₅FeSi intermetallic particle phases formed via a quasi-peritectic breakdown of α -Al₈Fe₂Si intermetallic particle phases in Al-6201 alloys.



Lu and Dahle[20] reported the formation of β -Al₅FeSi intermetallic particle phases through a binary reaction at higher Fe content (0.7 wt% Fe) in Al-7Si cast alloys.



Lu and Dahle [20] reported the formation of β -Al₅FeSi intermetallic particles through a ternary eutectic reaction at low Fe content (0.3 wt% Fe) in Al-7Si cast alloys.



2.5 Effect of cooling rate and concentration of Fe and Si in the formation of iron based intermetallic particles

The formation of the iron containing intermetallic compounds mainly depends upon the time and temperature for the solidification. To be more specific, the formation and growth of iron intermetallic particles depends on the cooling rate and concentration of different elements present at those temperatures. Generally, the larger intermetallic particles that form before the eutectic solidification are more detrimental compared to the smaller intermetallic particles which form after eutectic solidification. The formation of iron intermetallic phases occurs earlier upon increasing the iron concentration in the alloy. Hence, the time available for the growth of intermetallic particles is more which results in the formation of bigger sized iron intermetallic particles. Similarly, when the cooling rate is low, the time available for the growth of intermetallic particles during solidification will be more and results in much bigger sized iron intermetallic particles.

In pure aluminium, rapid solidification can suppress the formation of needle shaped Al+ Al₃Fe and resulting in the formation of granular shaped Al+Al₆Fe[22]. If the cooling rate is more than 1.0 K/s, the formation of Al₆Fe particles were reported along with Al₃Fe particles and if the cooling rate is less than 0.015 K/s formation of stable Al₃Fe is predominated [23]. Liu et al.[34] studied the influence of cooling rate in the growth of iron based intermetallic compound Al₉FeNi formed in AA2618 alloy. The study reported that on decreasing the cooling rate the intermetallic compound Al₉FeNi precipitates at the earlier stages of solidification and grew into flower like structure, whereas upon increasing the cooling rate the formation of flower like structures were suppressed and on rapid cooling the intermetallic compound Al₉FeNi was found to be refined.

On increasing the cooling rate and melt superheat temperature, the temperature at which β phase formation starts decreases until it joins with the silicon eutectic temperature. At this instant, the chemical composition of the residual liquid helps in the crystallization of α -phase. Thus, when the melt is superheated to a high temperature and if solidified with a cooling rate greater than $20\text{ }^{\circ}\text{C/s}$, the iron compound forms a metastable α phase instead of stable β phase[16]. Osawa et al.[35] studied the effect of cooling rate in the morphological changes of the β phase AlFeSi intermetallic particles and found that the average thickness of the needle-like intermetallic compounds decreases with increase in the cooling rate. The study also reported that both α and β phase AlFeSi is observed in Al-6%Si alloy, whereas only β phase AlFeSi is observed in Al-12%Si alloy. The intermetallic α -phase AlFeSi formed here is round shaped and β phase AlFeSi formed is needle shaped. This shows the effect of silicon content in the formation of iron based intermetallic particles.

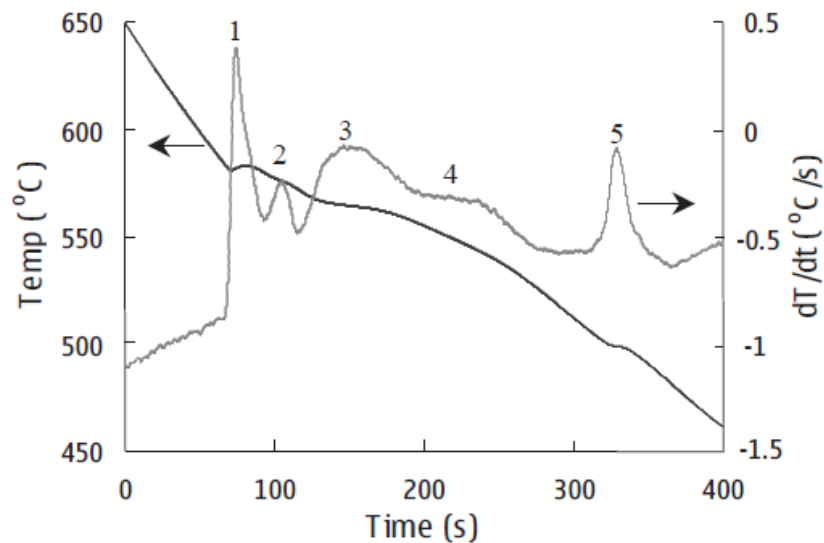


Figure 2.5 Cooling curve (Temperature vs time) and cooling rate curve (dT/dt vs. time) for an Al-9Si-3Cu-0.5Mg-1.0Fe alloy. The labels in the peaks are the following reactions: (1) Primary aluminium dendrites, (2) β -Al₅FeSi, (3) Al-Si eutectic, (4) complex Mg₂Si eutectic and (5) Al₂Cu eutectic[36].

Kim et al. studied the effect of iron intermetallic particles formed in Al-12%Si alloy with different iron concentrations and found that the intermetallic compound formed is much larger with high iron content than the low iron content. Depending on the cooling rate and concentration of iron, the size of intermetallic particles found to vary from few microns to millimetres. Figure 2.5 shows the cooling rate at which the formation of different phases in an Al-9Si-3Cu-0.5Mg-1.0Fe alloy initiates[36].

2.6 Effect of melt treatments in the formation of iron based intermetallic particles

The iron intermetallic plate length is directly proportional to the secondary dendrite arm spacing. When dendritic arm spacing increases the plate length increases, consequently the mechanical properties like strength and toughness decreases[23]. Zajac et al. reported that the homogenisation process results in the conversion of elongated β -AlFeSi particles located on the grain boundaries to spherical α -AlFeSi particles[37].

Recently it has been reported that the application of ultrasonic vibration can modify the morphology of intermetallic compounds in aluminium and aluminium silicon alloys. The coarse iron intermetallic platelets can be refined by ultrasonic vibration on crossing the liquidus temperature during solidification[35]. The acicular shaped Al_3Fe transforms to blocky shape on ultrasonic vibration treatment whereas, the acicular shaped $\text{Al}_9\text{Fe}_2\text{Si}_2$ particles was substituted by star shaped α - $\text{Al}_{12}\text{Fe}_3\text{Si}_2$ particles[22]. Figure 2.6 shows the effect of ultrasonic melt treatment of Al-2%Fe alloy for 60 seconds[22]. The large intermetallic platelets are found to be refined/broken after 60 seconds of ultrasonic treatment of the melt.

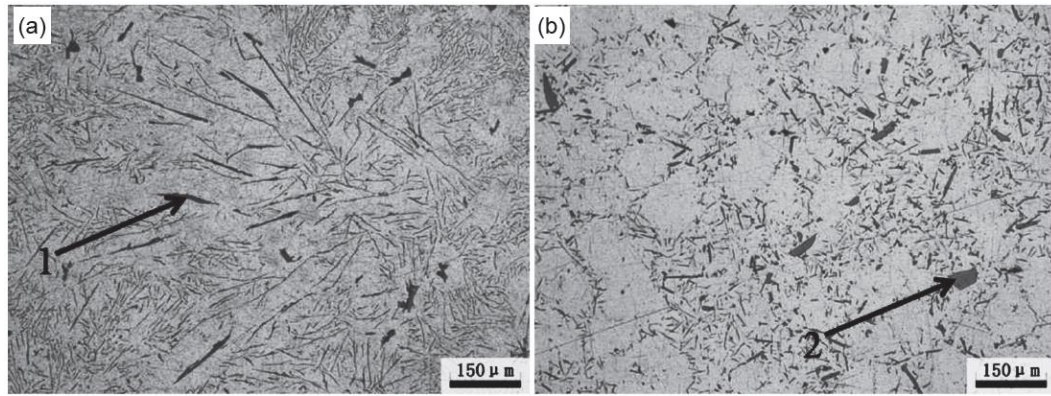


Figure 2.6 Microstructures of Al-2Fe alloy (a) without melt treatment (b) with melt treatment[22].

Iron intermetallic compounds can also be refined by semisolid processing of the aluminium and aluminium alloys. Irizalp et al.[38] reported that on thixoforming, the needle shaped β - Al_5FeSi intermetallic particles found to be modified in the form of small platelets along the grain boundaries of α -Aluminium. Shabestari et al.[39] also studied the effect of thixoforging in modification of iron intermetallic particles formed in A-380 alloy. They found that thixoforging leads to fracture of β -phase intermetallic particles and its redistribution along the grain boundaries.

2.7 Effect of heat treatment on the microstructural changes of aluminium alloys containing iron based intermetallic particles

The iron intermetallic phases in cast aluminium and aluminium silicon alloys generally undergo some degree of breaking up, spheroidisation and Ostwald ripening during heat treatments, but do not undergo any significant phase transformations. Apelian et al.[40] reported that in A356 and A357 alloys the eutectic silicon phase will break-up and spheroidize on heat treatment improving the mechanical properties. Basak et al.[4] studied the effect of heat treatment on iron intermetallic particles with different silicon concentrations and found that, at aging below the eutectic temperature the silicon phase spheroidize resulting in the fragmentation of β -phase across the length. On aging above the eutectic temperature, the β -phase grows faster

in thickness and the silicon phase forms a zagged-flaky morphology in presence of eutectic liquid.

2.8 Effect of iron based intermetallic particles in the castability of aluminium alloys

Castability mainly depends on the fluidity and formation of porosity in the cast alloy. Fluidity of an alloy is the ability of the molten metal to fill mould cavities before it solidifies. Fluidity is mainly reliant on the molten metal characteristics such as viscosity, surface tension and inclusion content[41]. Aluminium alloys can be superheated to increase the fluidity, but it will increase the chances of formation of casting defects such as gas porosity, solidification shrinkage and dross formation[42]. Also the oxide layer formation on superheating increases the surface tension and reduces the fluidity [43].

In recycled aluminium alloys, the iron intermetallic particles play a major role in controlling the fluidity. Increase in iron content decreases the fluidity, due to the formation of primary β -phase iron intermetallic particles in pure aluminium and aluminium alloys[44]. The platelet morphology of the primary β -phase iron intermetallic particles delivers a high interfacial area with the melt, obstructing the fluid flow during casting. Thus, the β -phase iron intermetallic behaves like an inclusion, which reduces the fluidity and increases the viscosity[44].

There is also an extensive research reported about the poor castability due to excessive porosity observed in iron containing alloys[45]. Figure 2.7 shows the increase in porosity in Al-Si-Cu-Mg alloy on increasing iron content[24].

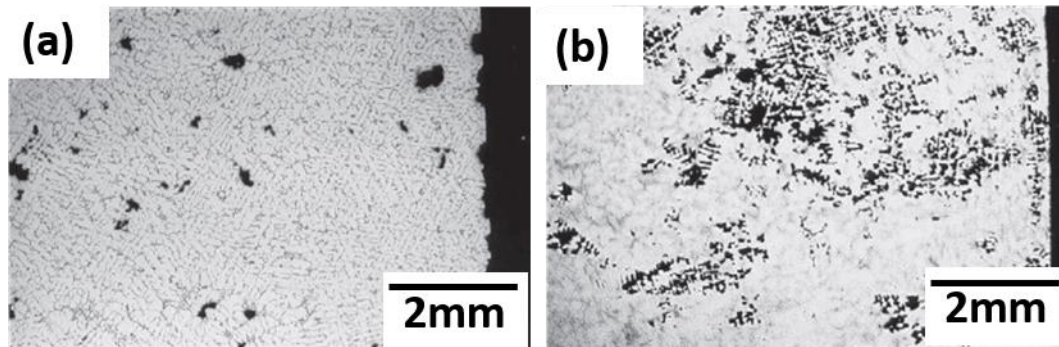


Figure 2.7 Shrinkage porosity in a cylindrical casting of Al-Si-Cu-Mg alloy with iron levels (a) 0.1% iron, (b) 1.0% iron[24].

Roy et al.[46] reported the poorer feeding characteristics and increased shrinkage due to the formation of β -phase iron intermetallic particles in aluminium alloys. They found that the β -phase iron intermetallic particles acts as nucleation sites for pores. Nevertheless, the β -phase iron intermetallic particles also limits the growth and broadening of the pores. The possible mechanism involved in the formation of porosity is explained as the long needle shaped morphology of the β -phase iron intermetallic particles which blocks the inter dendritic path and obstructs the liquid flow leading to micro shrinkage porosity[47].

2.9 Effect of superheating in the iron based intermetallic particles in aluminium alloys

Superheating temperature of Al– Si alloys has a remarkable effect on their solidification characteristics, helping in the structural refinement and thereby the properties of the alloy[48]. The melt superheating of the AlFeSi compounds results in crystallization of the α -phase intermetallic particles with Chinese script morphology rather than β -phase iron intermetallic particles with needle shaped morphology subjected to higher cooling rates[49].

Ahmad et al.[50] studied the Al-Si alloy with 1.12% Fe and 1.94% Fe at 710°C and 1000°C and found that the superheating refines the intermetallic plates to globular forms resulting in an improvement of strength. Figure 2.8 shows the microstructure

of the Al-Si alloy with an iron content of 1.94% with different superheats[50]. The light coloured particles are iron intermetallic particles.

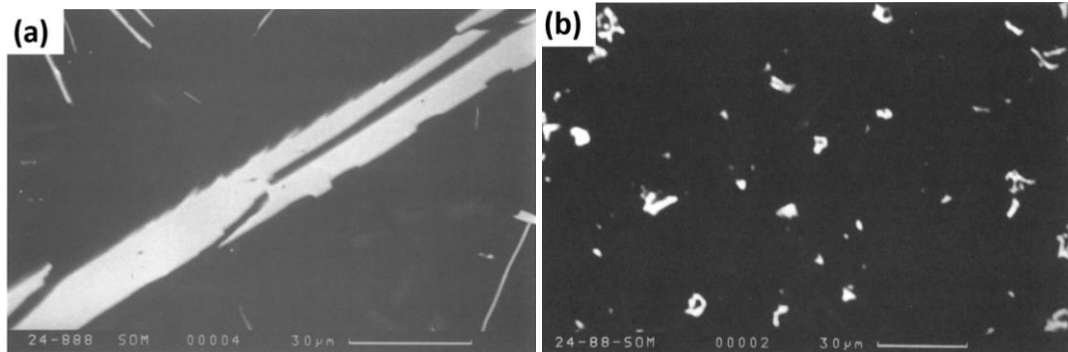


Figure 2.8 Microstructure showing the intermetallic particles in Al-Si alloy with an iron content of 1.94% (a) 710°C, (b) 1000°C[50].

The mechanism behind the formation of α -phase intermetallic particles is the variation of β -phase iron intermetallic formation temperature on increased cooling rate and superheat temperature. The primary β -phase growth time diminishes as β -phase iron intermetallic formation temperature becomes close to silicon eutectic temperature[49].

2.10 Effect of iron based intermetallic particles in the mechanical properties of aluminium alloys

In some aluminium alloys, iron is added intentionally to increase the high temperature strength, to reduce the corrosion in presence of steam at elevated temperatures etc.[51]. In pure aluminium, the elastic modulus, rigidity modulus, creep strength and machinability increases with increase in iron content. But for every 1% increase in the iron content, the Poisson's ratio reduces by approximately 0.0023%[14]. Generally iron intermetallic particles is considered as a defect in the aluminium alloys because of its negative effect in the mechanical properties. It has been extensively reported that when iron level in the aluminium alloys increases, the

ductility and tensile strength of the alloy decreases[24]. However, up to a certain critical level of iron content the deteriorating effect is small and quickly increases when the iron content is above the critical level. Mondolfo et al.[14] reported that when the iron content is more than 0.7 wt% in an aluminium silicon alloy, the formation of the brittle β -Al₅FeSi which is detrimental to the mechanical properties will be entertained. The critical iron content is directly related to the concentration of silicon in aluminium-silicon alloys. Figure 2.9 [24] shows the critical iron content is ~ 0.5 - 0.6% at 7% silicon and $\sim 0.8\%$ at 12 % silicon. Also, from Figure 2.9 it is understood that the time and temperature required for the formation of β -phase iron intermetallic particles decreases with increase in silicon content for the hypereutectic aluminium silicon alloys[24].

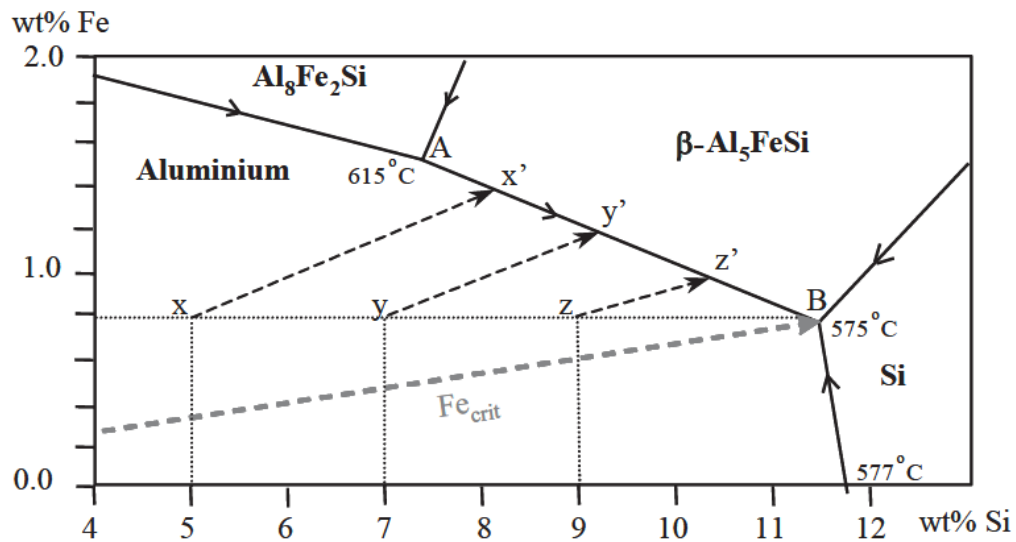


Figure 2.9 Simplified liquidus projection of the ternary Al-Si-Fe system for Al-Si alloys with critical iron levels[24].

Even though it is confirmed that iron intermetallic particles are detrimental to the mechanical properties of aluminium alloys, exact mechanisms involved are not completely explained. Some of the possible reasons explained by Taylor et al.[24] are

- When the concentration of iron in the aluminium alloys increases, the possibility of formation of β -phase increases. Once the amount of the brittle

β -phase increases more than a certain limit, it will directly take part in the fracture mechanism resulting in the failure of β -phase particles, hence decreasing the ductility of the entire alloy.

- It is also found that when the concentration of iron in the alloy increases, the porosity increases. Since the porosity is detrimental to the mechanical properties, the iron indirectly damages the mechanical property of the alloy.

The major reasons for the failure of aluminium alloys on mechanical testing's are defects (porosity and oxides), cooling rate (secondary dendrite arm spacing), and iron intermetallic particles due to iron content. On studying the effect of these parameters, the effect of iron intermetallic particles is found to be predominant[24]. Ravi et al.[52] studied the effect of iron content on mechanical properties of cast aluminium alloys and found that, the increase in iron content decreases the yield strength (YS), ultimate tensile strength (UTS), and % elongation whereas it increases the hardness of the alloy. When the iron content increases, the number of needle shaped β -phase increases. The β -phase dissolves at the grain boundaries and inter dendritic regions. These β -phase-alloy interfaces are weak regions and the sharp corners of the β -phase acts as stress raisers aiding to the crack initiation and provides pathway for its rapid propagation. Therefore, the ductility of the alloy drastically decreases with the increase in iron content associated with aluminium alloys. When the number of β -phase intermetallic particles increases, the ductility can drop to extremely small values (<1%) and sometimes the alloy fails even before yielding (<0.2% elongation).

2.11 Chemical modification of iron based intermetallic particles

There has been quite a lot of literature available in the area of chemical modification of iron intermetallic particles in aluminium. Mbuya et al.[41] reviewed the studies on influence of chemical modifiers like Mn, Cr, Be, Co, Mo, Ni, Sr, La, Ce, Nd, etc. in modification iron intermetallic particles in aluminium alloys. The study shows that most of these elements can control the detrimental effects of iron intermetallic

particles up to a certain limit. The harmful β -phase intermetallic can be modified by transforming the platelet morphology and encouraging the formation of compact morphology like Chinese script, polyhedral or star shape.

Manganese is one of the most widely studied element for the modification of the iron intermetallic particles in aluminium. Even though manganese is detrimental to the mechanical properties of aluminium alloys, it is extensively used for the modification of iron intermetallic particles in aluminium silicon alloys. The addition of sufficient amount of manganese favours the transformation of brittle platelet shaped β -phase iron intermetallic particles to Chinese script or polyhedral shaped α -phase iron intermetallic particles depending on the amount of Chromium present[41]. If the weight percentage of iron exceeds 0.8%, instead of β -Al₅FeSi particles, large primary α -Al₁₅ (Fe, Mn)₃Si₂ particles are formed on addition of manganese[14]. In presence of chromium, an additional α -Al₁₅ (Fe, Mn, Cr)₃Si₂ particle was also formed[41]. The morphology of these particles undergo changes with variations in cooling rate and concentration of silicon and iron. Manganese modified iron intermetallic compounds have a greater affinity to segregate resulting in decline of mechanical properties of aluminium alloys[51]. When the composition exceeds 0.6%Fe, 0.5%Mn, and 8%Si, at a temperature range of 610-600°C, AlFeMnSi type phases are formed which can result in sedimentation of very hard inclusions with unfavourable mechanical properties[53]. Shabestari et al.[54] reported that, the sedimentation/sludge formation is independent of the composition of iron in aluminium silicon alloy for Mn concentration above 0.6%. In general, Mn content is limited to less than half of the Fe content[24].

Cobalt with a similar atomic radius as iron is one of the best iron intermetallic modifier in aluminium since it will not generate any harmful compound by combining with silicon[14]. Couture et al.[55] suggested that a Co/Fe with a proportion of 0.5-1.0 is the suitable composition needed for the modification of iron intermetallic platelets to globular shape. The iron-cobalt phases generally form within the aluminium dendrites as an alternative of the inter dendritic regions and thereby reducing the segregation tendency [56]. It was observed that cobalt is less harmful in comparison with manganese addition to Al-Si alloys. But the formation of monoclinic Al₉Co₂ phase (32.7% Co) culminates the improvement in mechanical properties[14].

Beryllium is also reported as an iron intermetallic modifier in aluminium alloys. Beryllium combines with β -Al₅FeSi, changes its morphology by decreasing its angularity and thereby reducing the ductility of the alloy[57]. Murali et al.[56] suggested beryllium as the most effective modifier for aluminium alloys and found that the optimum quantity of beryllium for the modification is 0.26% beryllium per 1% of iron. The combined addition of beryllium with manganese or chromium is reported to improve the mechanical properties furthermore. AlFeBe phases form within the α -Aluminium dendrites and hence will be advantageous to the high temperature mechanical properties of the alloy[58]. Beryllium addition to aluminium alloys with an iron content above 0.07% has shown an increase in mechanical properties such as ultimate tensile strength, yield strength, percentage elongation, fracture toughness and hardness [59,60]. Nevertheless, if the iron content is less than 0.01%, beryllium addition is observed to diminish the mechanical properties. This could be due to the control of formation of iron intermetallic particles which at low iron concentration generally improves the mechanical properties of aluminium alloys [41]. In aluminium silicon alloys, the effect of beryllium addition is found to be more predominant since it refines the eutectic silicon and enhances the precipitation kinetics of strengthening precipitates[59,60]. Even though beryllium is found to be very effective in iron intermetallic particle modification in aluminium alloys, beryllium cannot be used as a modifier in an industrial level. Beryllium oxide, which forms on addition to aluminium alloys is highly carcinogenic[56] and results in acute pneumonitis and chronic granulomatous pulmonary diseases even at very low levels [58]. The protective measures for this toxic gas are not cost effective and inconvenient for an aluminium industry.

Scandium is another element found as effective for the modification of iron intermetallic particles in aluminium. Scandium is also found to be effective in grain refinement [61] and modification of eutectic silicon in aluminium alloys[62]. The addition of scandium results in the morphological change of platelet shaped β -phase iron intermetallic particles to Chinese script and skeleton shaped scandium rich intermetallic compounds [63]. Moreover, scandium impedes the growth of iron intermetallic particles from throughout the cross section by removing the nucleation sites for iron intermetallic compounds and thereby changing the direction of

growth[64]. However, Royset et al.[65] studied the solubility of scandium in twelve different cast aluminium alloys with constant iron (Fe) and scandium (Sc) contents of 0.5 wt% and 0.2 wt%, respectively, and found that the amount of Sc tied up in Fe bearing phases is so low that it can be regarded as negligible.

Nickel was also used as a modifier for iron intermetallic particles, but the addition of nickel forms nickel based iron intermetallic particles which is even more elongated and brittle[14]. Additionally the nickel based iron intermetallic particles can agglomerate resulting in the formation of fatigue crack[41].

The addition of strontium for the modification of iron intermetallic particles in aluminium silicon alloys was widely studied by Samuel et al.[66]. The addition of strontium resulted in the disintegration and dissolution of the needle shaped β -phase iron intermetallic particles. The strontium exterminates the nucleation sites for iron intermetallic particles. The disintegration and dissolution of the iron intermetallic particles was found to be enhanced with increasing strontium content up to an optimum level of strontium (130-400 ppm)[67]. The authors found that grain refining resulted in thickening of β -phase iron intermetallic particles and thus have a negative influence in the beneficial effect of modification[29]. The authors also suggested that strontium addition leads to the segregation of iron resulting in the formation of α - $\text{Al}_8\text{Fe}_2\text{Si}$. However, in strontium modified aluminium alloys, porosity formation is commonly associated with strontium oxides and β - Al_5FeSi platelets. These oxides are formed due to the higher oxygen affinity of strontium throughout the melting, and are challenging to eliminate by degassing[68]. Ashtari et al.[69] reported that the combined addition of manganese and strontium is more effective than strontium alone. The combined addition of manganese and strontium results in the modification of needle shaped β -phase iron intermetallic particles encouraging the formation of Chinese script and sludge morphology. Ibrahim et al.[70] studied the effect of strontium and beryllium in mechanical properties of aluminium based alloys with iron intermetallic particles and found that the tensile strength increases regardless of the alloy composition.

The addition of rare earth elements for the modification of the iron intermetallic particles is not yet widely studied. Some among the rare earth elements such as

yttrium, lanthanum, neodymium, cerium and europium were listed as possible candidates for the modification of the iron intermetallic particles[71]. Ravi et.al[72] studied the combined addition of some of these rare earth elements (mischmetal) to the aluminium silicon alloys for the modification of the iron intermetallic particles. Mischmetal is a combination of rare earth elements containing 50% cerium, 20% lanthanum, 20% neodymium and remaining other rare earth elements. The addition of 1% of mischmetal to the A356 alloys containing 0.2 and 0.6% % of iron was found to refine the microstructure resulting in the improvement of mechanical properties. The authors suggested that the mischmetal might have combined with iron and silicon to form intermetallic compounds and thereby reduced the amount of iron available for the formation of β -phase iron intermetallic particles[73]. The authors also studied the effect of combined addition of mischmetal and strontium on mechanical properties of A356 containing 0.6% of iron[52]. The study reported a complete modification of eutectic silicon and improvement in mechanical properties after the addition.

The modification of iron intermetallic particles in aluminium and aluminium alloys by adding lanthanum is not widely studied. There are some studies reported with remarkable contradictions regarding their modification potential. [73–76]. Hosseinifar et al.[74] reported a modification of iron intermetallic particles in a 6xxx series Al alloy with 0.5 wt% Fe and 0.8 wt% Si on addition of 0.2 wt% of La. They suggested that the mechanism behind the modification as formation of the La (Al, Si)₂ phase during solidification decreases the Si/Fe ratio in the melt resulting in the formation of a less detrimental α -AlFeSi phase instead of β -AlFeSi phase[75]. However, with higher silicon content the results are found to be contradictory. Samuel et al.[76] studied the lanthanum modification on A356 and A413 alloy with an addition of 1% La and found that there is no modification of Si and Fe phases. Li et al.[77] studied the microstructure modification of Al-12.6Si-0.8Fe die cast alloy with addition 3.6 wt% Mg and 0.5 wt% La and reported the formation of large script-like π -phase while lanthanum modifies the eutectic Si phase.

Even though the reported results are contradictory and the proposed mechanisms reported the formation of β -AlFeSi phase from $\text{Al}_{13}\text{Fe}_4$ phase, the effect of lanthanum in Al-Fe system was not studied.

Chapter 3. Research Methodology

3.1 Research Outline

The major reason for this research is, until now there is no suitable explanation or solution for the challenges facing to the effective recycling of aluminium and aluminium alloys. This research is mainly for understanding the effect of iron intermetallic particles in aluminium alloys by the use of advanced characterisation techniques such as X-ray computed tomography and electron microscopy and improving the recyclability of aluminium alloys by controlling the deleterious effects of the intermetallic particles by the addition of La, Mn, Sr modifiers and melt processing techniques such as superheating and controlled cooling rate.

3.2 Samples under investigation

The recycling of aluminium from the scraps is mimicked by the addition of iron into the aluminium and aluminium silicon alloy melt in the form of Al-10%Fe master alloy. In order to study the effect of different silicon and iron compositions, Al-0.6Fe, Al-2Fe, Al-7Si, Al-7Si-0.6Fe, Al-7Si-2Fe, Al-12Si-0.6Fe and Al-12Si-2Fe alloys were prepared. These alloys were prepared from commercially pure Al, Al-20Si master alloy and Al-10Fe master alloy supplied from Avon Metals Ltd, UK. Composition analysis of these alloys provided by the supplier are listed in the table 3.1. In order to study the effect of chemical addition, Lanthanum ingot (99.9% pure), Strontium pieces (99.9% pure), Manganese chips (99.9%) were purchased from Strem chemicals, UK. Each of these chemicals are then cast in to Al-10%La, Al-10%Sr and Al-10%Mn master alloys for adding in respective proportions to the Al and Al-Si melt.

Table 3.1 Elemental composition analysis of master alloys (wt%).

Alloys	Al	Si	Fe	Zn	Ni	Sn	Ti	Cr	Pb	Mg	Mn	Cu
Pure Al	99.8	.04	.08	.002	.025		.005	.001		.001	.001	.001
Al-20Si	79.69	20	.22	.01	.01	.01	.01	.01	.01	.01	.01	.01
Al-10Fe	89.03	.16	10.2	.02	.01	.01	.02	.01	.01	.02	.49	.02

3.3 Experimental procedure-preparing the cast alloys

Since the objective of each of the casting is different, the method of preparation was also different. Prior to every casting, the respective amount of each of the alloys/elements were weighed to their specific ratio with a total of 5 wt% extra amount to compensate for the loss during melting. In each experiment, about 2.5 kg of melt was prepared in a clay graphite crucible in a Carbolite top load electric arc furnace. All the alloys were added into the crucible and heated up to 740°C. In the case of superheat study three different melts were prepared at 700°C (lower than normal melting), 800°C (low superheat) and 900°C (high superheat). The melting time depends on alloy composition and superheat temperature. Once the alloy is melted, to ensure proper mixing and homogenisation the melt was hold at this temperature for 30 minutes with intermittent stirring at every 10 minutes. The melt is then degassed using argon before casting. The molten metal is then poured into a clay-graphite mould preheated to 200°C, except in case of the samples for studying the effect of cooling rate and superheat. In order to study the different cooling rates, the molten metal was poured into a water cooled copper wedge mould (very high cooling rate), cast iron mould (industrially achievable high cooling rate) and clay graphite mould (low cooling rate) respectively (Figure 3.1). The cooling rate of each of them were studied using K type thermocouples dipped in to the moulds. In order to study the superheat effect, the molten metal was poured into a cast iron mould without degassing at the respective superheat temperatures.

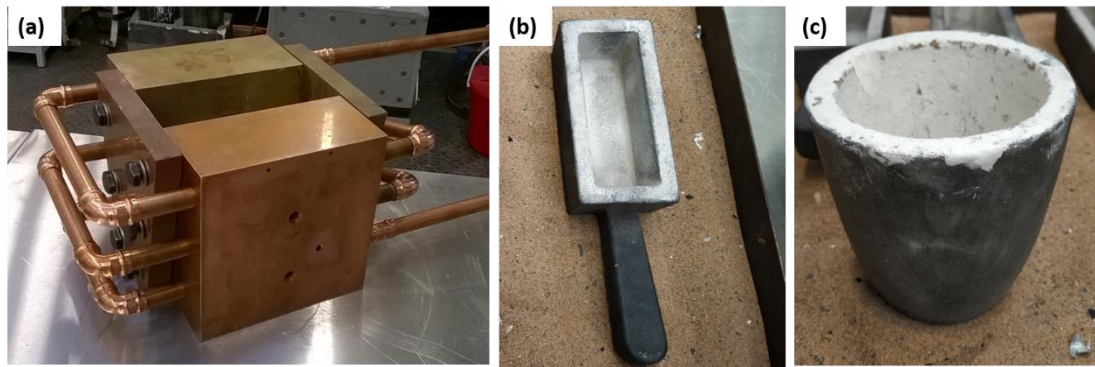


Figure 3.1 Mould for casting (a) water cooled wedge copper mould, (b) cast iron mould (c) clay graphite crucible mould.

3.3.1 Chemical modification

To study the effect of chemical modification of iron intermetallic particles in aluminium and aluminium 7 wt% silicon alloy, lanthanum (La), strontium (Sr), and manganese (Mn) were added in individual and combined form. Since the melting point of these elements are different and to keep the same melting temperature for all the additions Al-10 wt% alloys of the elements were prepared initially. Al-10 wt% La, Al-10 wt% Sr and Al-10 wt% Mn were prepared by adding them into commercially pure aluminium melt with a 90: 10 wt ratio at 950°C. These elements were wrapped in aluminium foil under glove box to prevent moisture and then added with the wrap into the melt to prevent immediate fire. The melt was stirred intermittently with 10 minutes interval for 1 hour, holding at 950°C to ensure all the substrates (elements) are dissolved and the mixture is homogenised. After preparing these master alloys, it was then added to the Al-Fe and Al-Si-Fe alloy melts at 740°C for modification and stirred intermittently for 10 minutes before pouring. The molten alloy was then poured into a graphite mould without degassing at the respective superheat temperatures.

3.3.2 Vacuum induction melting (VIM)

In order to study the castability and effect of superheat in porosity in AlSiFe alloys, the superheat experiment was repeated in a vacuum induction melting. The respective amounts of each of the alloys for preparing 2 kg of Al-7Si-2Fe alloy and Al-7Si alloy was taken in a clay graphite crucible and was placed in the induction furnace inside the vacuum chamber. The vacuum pump is used to reduce the partial pressure of air/atmospheric gas in the chamber to 10^{-2} atm. The cast iron mould was placed inside the vacuum chamber for casting. The clay graphite crucible inside the induction furnace was then heated to 700°C and was held for 10 minutes after melting. The temperature was monitored using a dip thermocouple installed in the furnace and an IR thermal camera. Molten metal was then poured into this cast iron mould by tilting the furnace using a lever equipment inside the chamber itself to ensure there is no influence of external environment throughout the casting process. The cast was then allowed to cool in the vacuum chamber to prevent interactions with the external atmosphere. Another sample is produced by repeating the same procedure by changing the melt temperature to 900 °C.

3.4 Microstructure Analysis

3.4.1 Sample Preparation for Microstructure Analysis

Specimens for microstructural analysis were cut from the alloys cast using a Buehler-AbrasiMatic 300 abrasive cutter and a Buehler Isomet 5000 linear precision cutter and hot mounted in Bakelite using Buehler's SimpliMet 3000 mounting machine. The mounted samples were then ground and polished to mirror finish using Buehler's Automet 300 grinder/polisher.

Table 3.2 shows the polishing procedure followed for this samples. After every grinding and polishing step, samples were cleaned using running water and acetone and then dried to avoid water marks on the sample surface.

Table 3.2 Polishing procedure

Step	Paper	Suspension	Direction	Force	Time	Speed (rpm)
Grinding	P400	Water	Complimentary	15 N	30-60s	300
Grinding	P1200	Water	Complimentary	15 N	30-60s	300
Polishing	Texmet	9 micron	Contra	20 N	5 min.	150
Polishing	Trident	3 micron	Complimentary	20 N	4 min.	150
Polishing	Trident	1 micron	Complimentary	20 N	3 min.	150
Polishing	Chemomet	SiC Abrasive suspension	Contra	20 N	3 min.	150

3.4.2 Optical Microscopy

Optical microscopy studies were carried out on the polished samples using a NIKON ECLIPSE LV150N metallurgical microscope. The microstructures were taken from the approximate centre of the samples to get a characteristic structure. But the optical microscope was incapable of scanning a large area for 2 dimensional quantification of porosity and particles size analysis.

To study the microstructure in a larger area and to quantify the porosity and particle size, the optical microscope in an Alicona infinite focus is used. This equipment is generally used for roughness measurement, where a large area is scanned with an automatic multi focusing.

Image J is used to analyse the particle size and porosity distribution in 2 dimension. Various tools in the software were used for the phase selection and phase segregation analysis measurements. The data from the porosity analysis and particle size analysis is then plotted in Microsoft Excel. The size of the particles are measured from the ferret data and size of the pores are measured from the equivalent diameter considering the pore as circular in 2 dimension.

$$\text{Equivalent diameter} = (4 \times \text{Area} / \pi)^{1/2} \dots\dots\dots(1)$$

3.4.3 Scanning electron microscope (SEM)

SEM is used to obtain higher magnification images for better visualisation of the intermetallic particles in the microstructure. It has a large depth of field and higher resolution compared to the optical microscope. In addition, SEM doesn't have any reflections as in case of optical microscope and works on the basis of scattered electrons, which makes them useful to study shiny surfaces of aluminium-silicon alloys. Therefore, fracture surfaces were also investigated under SEM with SE2 detectors to find the type of failure and understanding the fracture mechanism. Micrographs were captured by a field emission scanning electron microscope (FESEM) using Zeiss, Carl Zeiss SMT AG instrument coupled with energy dispersive X-ray spectrometer (EDS) and a HITACHI TM3030Plus Table top microscope. The SEM-EDS is used for the elemental mapping of the samples. This will give a good distinction between needle shaped silicon particles and iron particles. This is also helpful to find the formation and distribution of different phases after the addition of modifying elements.

3.4.4 Three Dimensional FIB-SEM

Even though the intermetallic particles have a needle shaped morphology in 2 dimensions, it appears as a plate shaped morphology in 3 dimension. To overcome

the limitations of 2D analysis, three dimensional (3D) characterization techniques such as X-ray Computed Tomography and FIB-SEM (focused ion beam milling coupled with a scanning electron microscope) tomography was used. The polished samples were observed under SEM and a 50 x 50 μ m area having the required intermetallic particle phases is selected for milling. The selected area of the sample surface is then covered with a 1 μ m thick layer of platinum deposited using the ion beam. An ion beam voltage of 30 kV and an electron beam voltage of 1 kV was used throughout the milling process. The three sides of the platinum layered area was then dug around to isolate the volume to be milled and to ensure the maximum field of view. An ion beam current of 30nA was used to make a rough milling and 3nA was used to cut the material near by the platinum covered area. An ion beam current of 1nA was used to cut the 50 x 50 μ m area into 100 nm thick slices for a depth of 30 μ m contained in a typical data stack. These images were then stacked in order to generate a 3D data simultaneously using 'slice and view' software (FEI).

These 2 dimensional images were reconstructed using Avizo 9.8 software to generate the 3 dimensional volume. The iron intermetallic particles were given red colour, aluminium matrix white colour and lanthanum compounds yellow colour accordingly.

3.4.5 Transmission electron microscopy (TEM)

TEM can be used to obtain higher magnification or better resolution images compared to SEM. TEMs can generate the diffraction patterns from the microstructure and reveals the internal microstructure of different phases present in them.

3.4.5.1 Sample preparation for TEM

The metallographic sample preparation for TEM is same as optical microscopy and SEM. The sample surface is then focussed using an SEM coupled with FIB. TEM samples with a dimension of 6-12 micron length, 2-3 micron width and 100-200 nm depth were cut and lift up with the ion miller from the focussed area. One of the major artefact observed on the sample surface is the gallium used in the ion milling. This can be seen as sediments on the grain boundaries and interphase boundaries. The extracted TEM sample is then inserted into the HRTEM for further investigations.

TEM images of the alloys were captured and mass fraction of aluminium, lanthanum and iron was measured using a FEI TALOS Transmission Emission Microscope (TEM) coupled with energy dispersive X-ray spectrometer (EDS). Selected Area Diffraction (SAD) patterns of the particles were taken from different areas of Al-2Fe and Al-2Fe-1La alloys. The diffraction patterns were then analysed in a crystal maker software to understand the crystal structure of the particles. Crystallographic data base for the similar phases were downloaded from the National Chemical Data base Service (NCDS) and used to match with the diffraction pattern obtained from the TEM. The distance between the atoms (a, b coordinates) and angle between them were measured using the software and were compared to find the crystal structure of the particles.

3.4.6 Three Dimensional X-ray computed tomography

The tensile samples were scanned before and after the test using the Zeiss Versa at CiMat, WMG for studying the fracture mechanism and particle distribution in a bigger area. The scanning conditions are given in Table 3.3. To reach the best resolution possible, a 0.49 flat panel was used as the detector. The detector is composed of 2048 x 2048 pixels resulting in 3.67- μm resolution. The raw data was reconstructed using the Zeiss reconstruction software, which uses a filtered back projection (FBP)

algorithm creating a stack of DICOM images. The stack was then be used for analysis with Avizo 9.8 (FEI, USA; <http://www.fei.com/software/avizo3d>).

Samples for porosity and particle distribution analysis were prepared with 1 mm diameter using an EDM wire cutter. The reconstructed 3D data stack is analysed using Avizo 9.8 software. The matrix, particle and porosity were selected individually based on their contrast range and assigned white, red and blue colours respectively.

Table 3.3 X-ray tomography scanning parameters

Scanning condition Zeiss Versa

Voltage (kV)	80
Current(A)	87
Number of projections	1601
Filtration	LE4
Voxel size (lm)	3.67

3.5 Differential scanning calorimetry (DSC)

A Differential scanning calorimetry (NETZSCH STA 449 F3 Jupiter) is used to record the characteristic transformations associated with exothermic or endothermic enthalpy changes. The DSC equipment consists of a furnace, one reference crucible, one sample crucible and thermocouples under the crucibles. The power difference needed to retain the equilibrium temperature of sample crucible and reference crucible is used to generate the data. The experiments were carried out using aluminium alloy samples with an average weight of 45mg (\pm 3mg) in sapphire crucibles with lid. High purity argon (N6.0) is used as the protective gas after reducing

the oxygen content in the inlet to approximately 1ppb. The furnace is evacuated and backfilled with argon two times before the start of each experiment. A cooling rate of 20 °C/s was used for cooling with the help of a chiller unit.

3.6 Mechanical property analysis

3.6.1 Nanoindentation

Nanoindentation tests were carried out using a standard Berkovich indenter (included angle, 142.3°), in a nanoindentation instrument (Micro Materials) which simultaneously measures force and displacement as the indentation progresses. The samples for testing were prepared flat and finely polished to control the surface roughness effects during indentation. Twelve indentations each were taken from both particle and primary aluminium by applying a maximum load of 5 mN. The load was applied for 20 s and unloaded in 20 s keeping a constant maximum load for 6 s (dwell). The detailed test procedure can be found elsewhere[78]. Figure 3.1 shows the typical loading – unloading curves generated from nanoindentation studies proposed by Oliver and Pharr[78,79]. In order to minimize the indentation size effects, an interval of 25 µm between each indentation was used[80,81]. The peak indentation depth (h_{max}) is the maximum displacement of the indenter from its initial position/origin at peak load (P_{max}). It contains both elastic and plastic deformations. Nevertheless, the material also elastically recovers its shape when the indenter is unloaded[82]. From these data generated from the indentation plots, elastic displacements are measured for calculating the elastic modulus, E . The hardness, H , can be calculated by removing this elastic contribution from the total displacement of the indenter.

The hardness (H) can be calculated as:

$$H = P_{max}/A \dots\dots\dots (2)$$

Where, P_{max} is the peak load and A is the projected area of contact between the indenter and the sample[1].

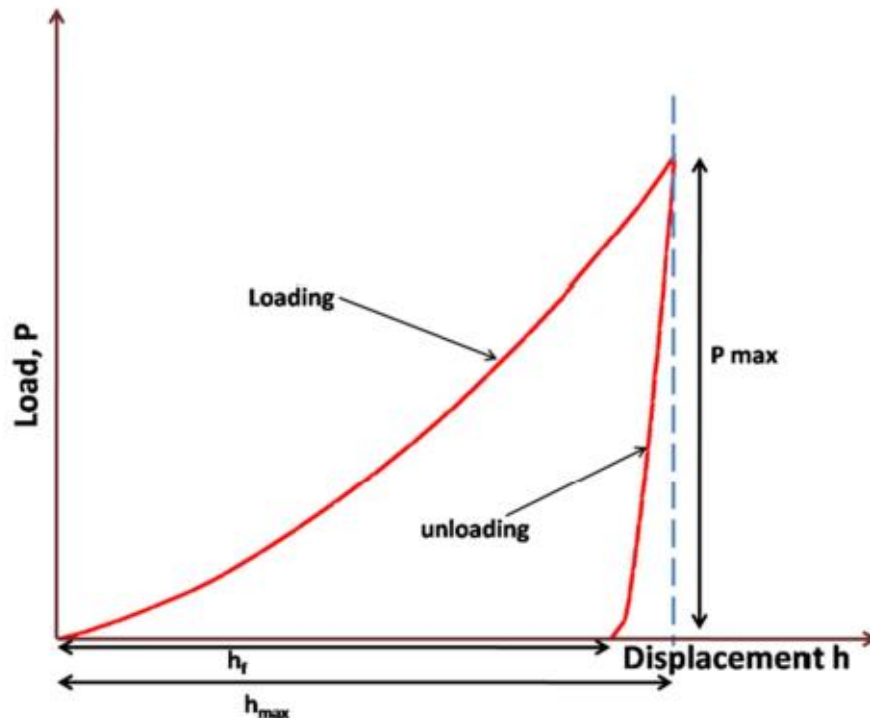


Figure 3.2 Schematic representation of a loading-unloading curve[79].

3.6.2 Mechanical Property Characterisation

Cylindrical tensile samples (Figure 3.3) were prepared using a CNC lathe according to the dimensions specified in ASTM E-8M[83]. Tensile properties were evaluated using a 100 kN universal tensile testing machine (Instron model 5800R) at a constant crosshead speed of 2 mm/min. The wedge shaped grips were used to attain maximum gripping of the cylindrical test pieces. The user interface of the Instron Bluehill software is used for the setting up the test method and evaluation of the test results. A video extensometer is used to measure the strain. The samples were painted with a graphite spray paint on one side to reduce the reflections from the shiny aluminium surface upon using video extensometer. The gauge length is then marked with white spots on the sample to make it identifiable and measurable for

video extensometer. The test data including the strain, measured using video extensometer is automatically saved in the bluehill software. Five tensile samples of each condition were prepared and tested under similar conditions to find the repeatability of the results and standard deviation associated with it. The fracture surface was then studied under SEM to find the nature of fracture. A detailed investigation of the fractured area is carried out using XCT. 2D orthogonal slices from CT and its 3D reconstructed images were studied.

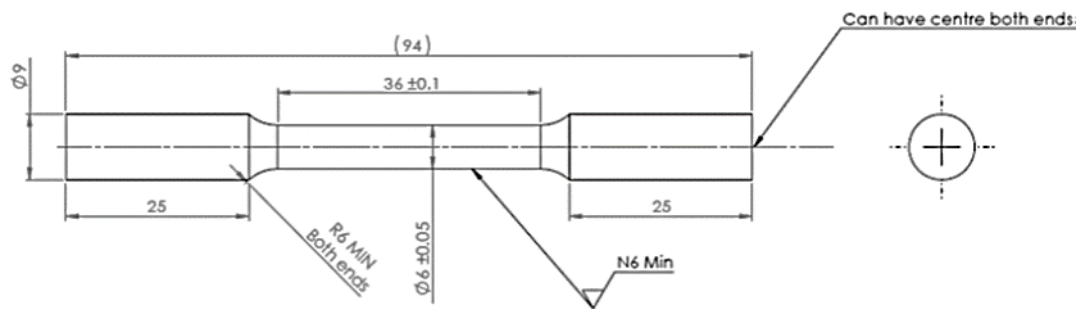


Figure 3.3 Tensile testing sample prepared as per ASTM E-8M[83]

Chemical composition of all the alloys studied in this theses is measured using a Bruker Q8 Magellan optical emission spectrometer. The samples of all the alloys were polished on the sides to a smooth finish and the measurements were taken from 5 different locations. The maximum and minimum mass fraction is assumed as the weight percentage range for the corresponding element in the alloy. The measured chemical composition with all the elements having a concentration above 1ppm is listed in table 3.4

Table 3.4 Chemical composition of alloys prepared (wt%)

Alloys	Al	Si	Fe	Mn	La	Sr	Ni
Al-0.6Fe	98.96-99.15	0.06-0.07	0.57-0.65	0.01			0.02
Al-2Fe	97.86-98.05	0.06-0.07	1.99-2.00	0.01			0.02
Al-2Fe-1La	96.87-97.15	0.06-0.07	1.99-2.00	0.01	0.98-1.02		0.02
Al-2Fe-1Mn	97.06-97.23	0.05-0.06	1.99-2.00	1.01-1.1			0.02
Al-1Fe-0.5Mn	98.34-98.70	0.04-0.05	0.98-1.08	0.50-0.55			0.02
Al-2Fe-1Mn-0.04Sr	97.06-97.23	0.05-0.06	1.99-2.00	1.00-1.1		0.04	0.02
Al-7Si	92.26-93.16	6.82-7.02	0.12	<0.01			0.01
Al-7Si-0.6Fe	92.3-92.57	6.99-7.01	0.59-0.60	<0.01			0.01
Al-7Si-1Fe-0.5Mn	91.05-91.32	7.00-7.10	0.98-1.05	0.5-0.55			0.01
Al-7Si-1Fe-0.5Mn-0.04Sr	91.05-91.22	7.00-7.08	0.98-1.04	0.5-0.55		0.04	0.01
Al-7Si-2Fe	90.84-91.10	6.98-7.00	1.99-2.00	0.01			0.01
Al-7Si-2Fe-1Mn	90.04-90.10	6.96-7.00	1.98-2.00	1.01-1.02			0.01
Al-7Si-2Fe-1Mn-0.04Sr	90.01-90.08	6.96-7.01	1.98-2.03	0.99- 1.00		0.04	0.01
Al-7Si-0.6Fe-1La	91.48-91.63	6.96-7.11	0.57-0.64	<0.01	0.99-1.00		0.01
Al-7Si-2Fe-1La	90.10-90.15	6.88-7.01	1.91-2.05	0.01	1.00-1.02		0.01
Al-12Si-0.6Fe	87.31-87.57	11.98-12.00	0.59-0.60	<0.01			0.01
Al-12Si-2Fe	85.92-86.19	11.99-12.01	1.99-2.00	0.01			0.01

Chapter 4. Effect of silicon and iron concentration in the formation and growth of iron intermetallic particles

The majority of the aluminium scraps derives from the automobile industry. Al-7Si alloy is the most widely used aluminium alloy in the automobile industry and Al-12Si alloy is a widely used eutectic alloy of aluminium. Hence the majority of aluminium alloy scraps belongs to these categories. These alloys are of prime importance and selected for the recyclability studies in this project. Iron content of 0.6% and 2% were selected since aluminium with iron content lower than 0.5 wt% do not have considerable influence in mechanical properties. The critical iron content for Al-7Si alloy is ~ 0.6 wt %. Depending on the amount of silicon and iron present in the alloys, the intermetallic phases formed will be different. The quantity of iron intermetallic particles and thickness of intermetallic particles also vary with the changes in silicon and iron concentration. This chapter studies the microstructural changes of aluminium with different iron and silicon concentration and the mechanical properties associated with it. The effect of iron and silicon in the mechanical properties of the aluminium alloys is correlated with this and explained.

4.1 Prediction of phase formation using ThermoCalc

Figure 4.1 shows the expected phases in equilibrium solidification conditions using a ThermoCalc software. The expected intermetallic particles for pure aluminium ($<1\%$ Si) in equilibrium conditions are θ -Al₁₃Fe₄ which is monoclinic and acicular shaped. When the silicon content is above 2%, stable monoclinic β -Al₅FeSi intermetallic particles are expected. This means the stable intermetallics which will form in case of the Al-7Si alloy and Al-12Si alloy are monoclinic β -Al₅FeSi particles. Both θ -Al₁₃Fe₄ and β -Al₅FeSi are found to have detrimental properties from the literature studies. When the iron content is increased to 2% (Figure 4.1b), the percentage of intermetallic compounds is also increased even though the expected intermetallic particles may vary with change in cooling rate and rate of undercooling. The

nucleation and phase transformation follows a different sequence in case of 2%Fe addition compared to the 0.6% Fe addition. According to the ThermoCalc plots (Figure 4.1), the solidification sequences of the different alloys considered in this study are shown in table 4.1.

Table 4.1 Solidification sequence/microstructure evolution of aluminium and aluminium silicon alloys upon cooling from liquid state

Alloy	Solidification sequence
Al-0.6Fe	<ol style="list-style-type: none"> 1. Liquid \rightarrow Al + Liquid 2. Al + Liquid \rightarrow θ-Al₁₃Fe₄ + Al + Liquid 3. θ-Al₁₃Fe₄ + Al + Liquid \rightarrow θ-Al₁₃Fe₄ + Al
Al-2Fe	<ol style="list-style-type: none"> 1. Liquid \rightarrow θ-Al₁₃Fe₄ + Liquid 2. θ-Al₁₃Fe₄ + Liquid \rightarrow θ-Al₁₃Fe₄ + Al
Al-7Si-0.6Fe	<ol style="list-style-type: none"> 1. Liquid \rightarrow Al + Liquid 2. Liquid + Al \rightarrow Al + β-Al₅FeSi + Liquid 3. Al + β-Al₅FeSi + Liquid \rightarrow Al + β-Al₅FeSi + Si
Al-7Si-2Fe	<ol style="list-style-type: none"> 1. Liquid \rightarrow Liquid + α-Al₈Fe₂Si 2. Liquid + α-Al₈Fe₂Si \rightarrow Al + α-Al₈Fe₂Si + Liquid 3. Liquid + α-Al₈Fe₂Si + Al \rightarrow Al + β-Al₅FeSi + Liquid 4. Al + β-Al₅FeSi + Liquid \rightarrow Al + β-Al₅FeSi + Si
Al-12Si-0.6Fe	<ol style="list-style-type: none"> 1. Liquid \rightarrow Liquid + Al 2. Liquid + Al \rightarrow Al + β-Al₅FeSi + Si
Al-12Si-2Fe	<ol style="list-style-type: none"> 1. Liquid \rightarrow β-Al₅FeSi + Liquid 2. β-Al₅FeSi + Liquid \rightarrow Al + β-Al₅FeSi + Liquid 3. Al + β-Al₅FeSi + Liquid \rightarrow Al + β-Al₅FeSi + Si

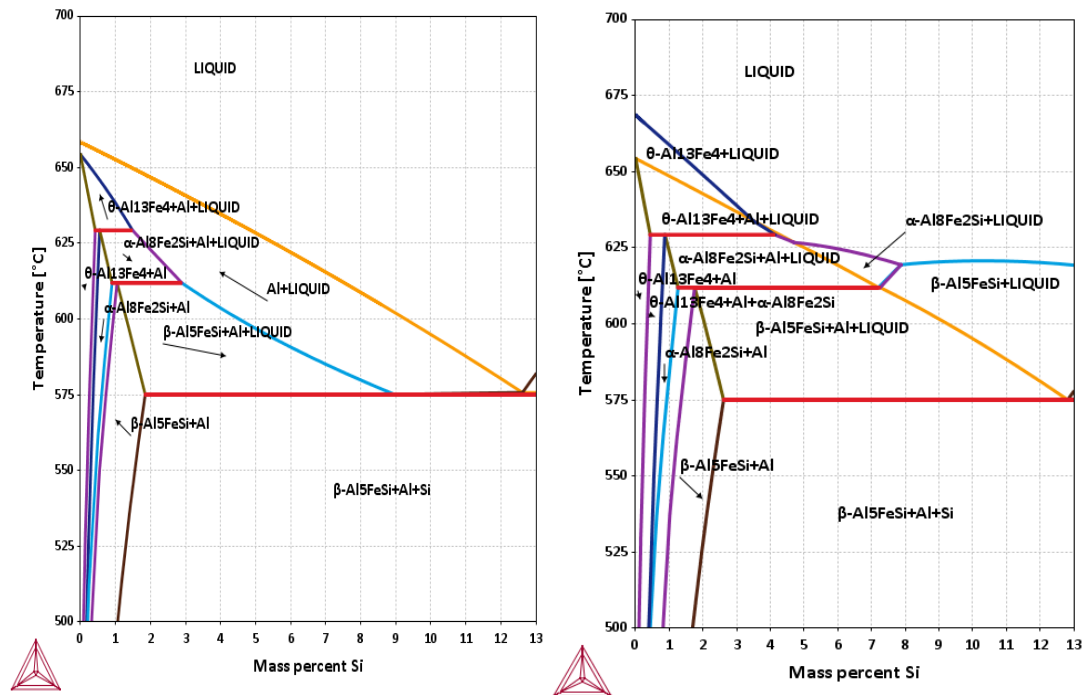


Figure 4.1 ThermoCalc computed binary phase diagrams of the aluminium-rich side in the Al-Fe-Si system showing the expected phases in equilibrium conditions, (a) Al-Si alloy with 0.6 wt% Fe and (b) Al-Si alloy with 2 wt% Fe.

4.2 Microstructural studies

Figure 4.2 shows the optical images from Al-0.6Fe alloy and Al-2Fe alloy. The Al-0.6Fe alloy (Figure 4.2a) is found to have a microstructure with refined particles around the grain boundaries. The 2wt % iron addition to the aluminium (Figure 4.2b) resulted in the formation of a large number of intermetallic particles.

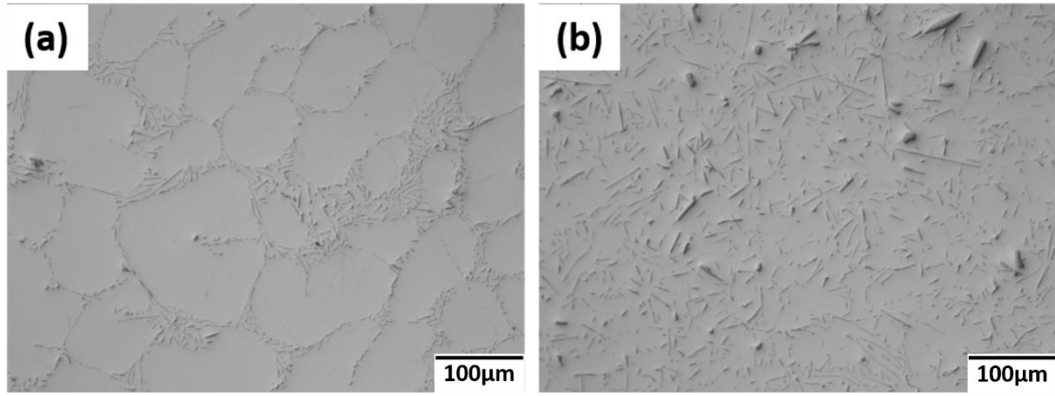


Figure 4.2 Optical microstructure of (a) Al-0.6Fe, (b) Al-2Fe.

Figure 4.3 shows the optical images from Al-7Si-0.6Fe alloy and Al-7Si-2Fe alloy. The Al-7Si-0.6Fe alloy (Figure 4.3a) is found to have a microstructure with few big intermetallic particles along with a majority of refined particles around the grain boundaries. The 2wt % iron addition to the aluminium (Figure 4.3b) resulted in the formation of a large number of big and small intermetallic particles.

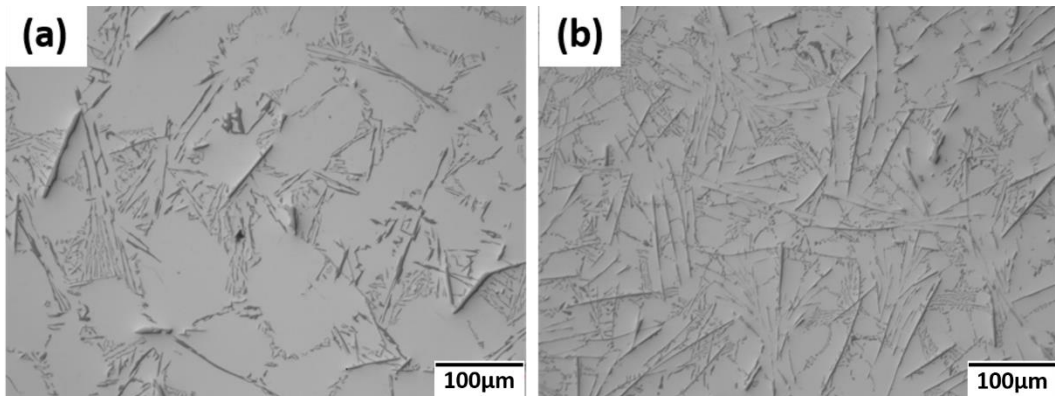


Figure 4.3 Optical microstructure of (a) Al-7Si-0.6Fe, (b) Al-7Si-2Fe.

Figure 4.4 shows the optical images from Al-12Si-0.6Fe alloy and Al-12Si-2Fe alloy. The Al-12Si-0.6Fe alloy (Figure 4.4a) is found to have a microstructure with big intermetallic particles along with a few eutectic silicon particles. The 2wt % iron addition to the aluminium (Figure 4.4b) resulted in the formation of plentiful number

of small intermetallic particles along with few large ones. The intermetallic particles in Al-12Si alloy is much bigger than Al-7Si alloys.

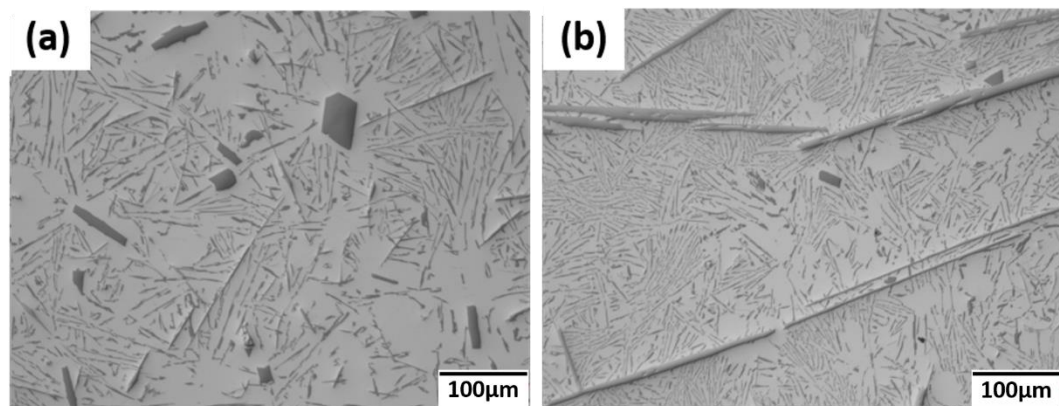


Figure 4.4 Optical microstructure of (a) Al-12Si-0.6Fe, (b) Al-12Si-2Fe

Figure 4.5 to 4.7 shows the scanning electron microscopy (SEM) images of Al-0.6Fe, Al-2Fe, Al-7Si-0.6Fe, Al-7Si-2Fe, Al-12Si-0.6Fe, Al-12Si-2Fe alloys.

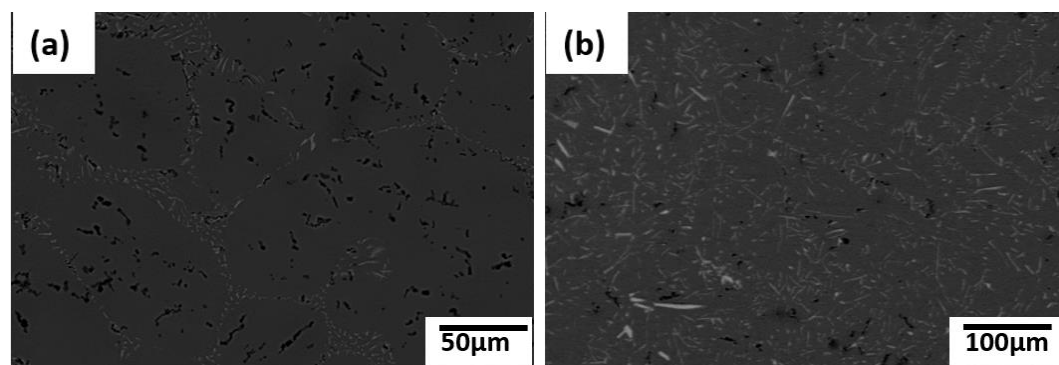


Figure 4.5 SEM images of (a) Al-0.6Fe, (b) Al-2Fe

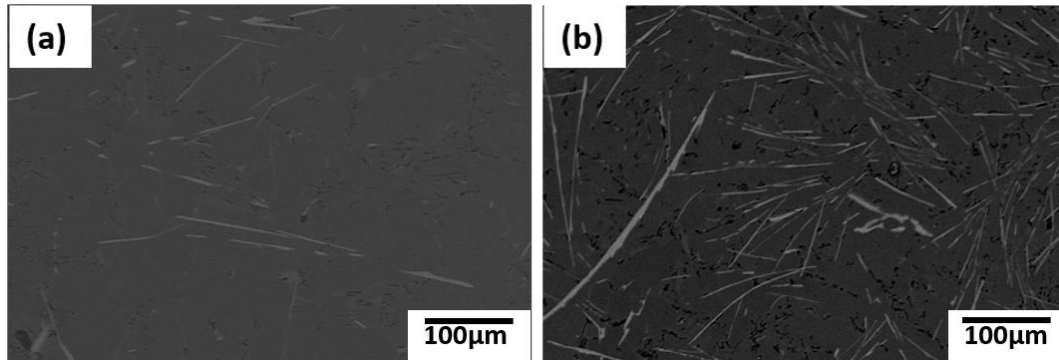


Figure 4.6 SEM images of (a) Al-7Si-0.6Fe, (b) Al-7Si-2Fe.

These SEM images more expressively shows the intermetallic particles. The 2Fe and Si additions has increased the size of intermetallic particles considerably.

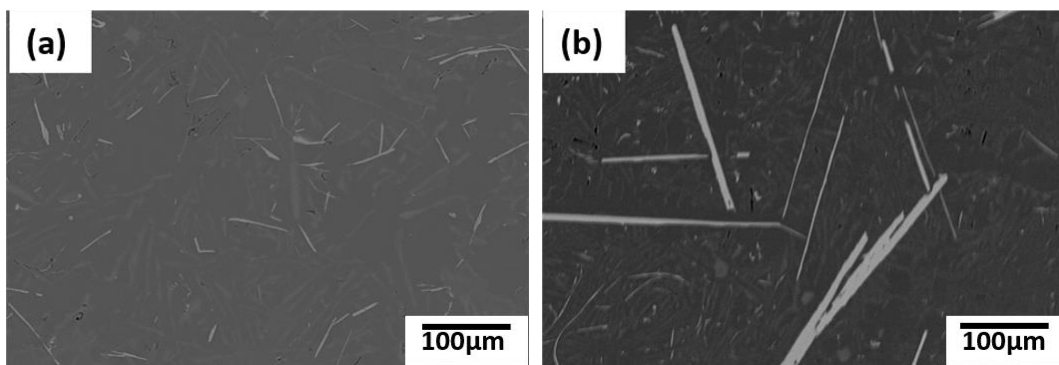


Figure 4.7 SEM images of (a) Al-12Si-0.6Fe, (b) Al-12Si-2Fe

Figure 4.8 and 4.9 shows the elemental mapping of Al and Fe in Al-0.6Fe alloy and Al-2Fe alloy. The 2% iron addition resulted in the formation of a large number of needle like iron intermetallic particles. A few thicker needle like intermetallic particles were also found in the microstructure.

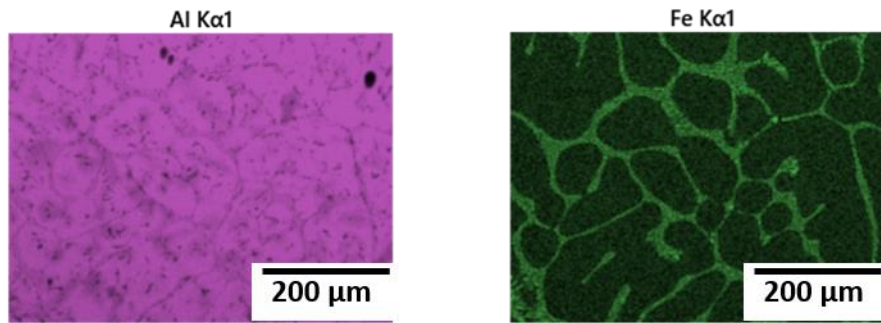


Figure 4.8 EDS elemental mapping of Al-0.6Fe (violet colour represents distribution of aluminium and the green colour represents distribution of iron).

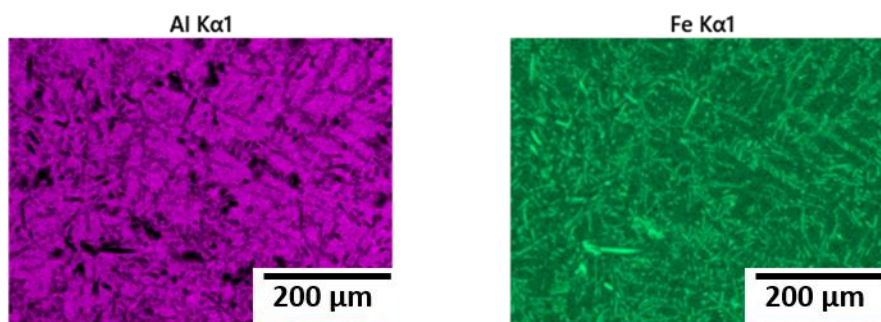


Figure 4.9 EDS elemental mapping of Al-2Fe (violet colour represents distribution of aluminium and the green colour represents distribution of iron).

Figure 4.10-4.13 shows the elemental mapping of Al and Fe in Al-7Si-0.6Fe alloy, Al-7Si-2Fe alloy, Al-12Si-0.6Fe alloy and Al-12Si-2Fe alloy respectively. Silicon was found to be refined in Al-7Si-0.6Fe alloy, with Fe equals to the critical iron content. The importance of critical iron content is explained later in chapter 5. The addition of 12% silicon not only increased the iron intermetallic platelet numbers and thickness, but also resulted in the formation of a large number of silicon flakes and eutectic silicon blocks. The thick yellow particles, shows the eutectic silicon and the thin yellow needle shaped shows the silicon flakes where both are detrimental to the mechanical properties.

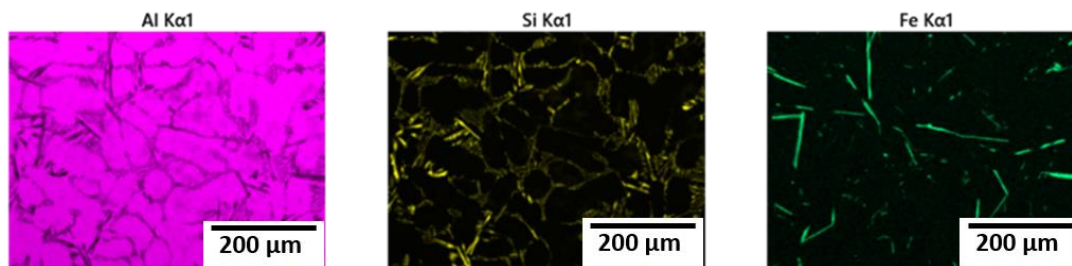


Figure 4.10 EDS elemental mapping of Al-7Si-0.6Fe (violet colour represents distribution of aluminium, the yellow colour represents distribution of silicon and the green colour represents distribution of iron).

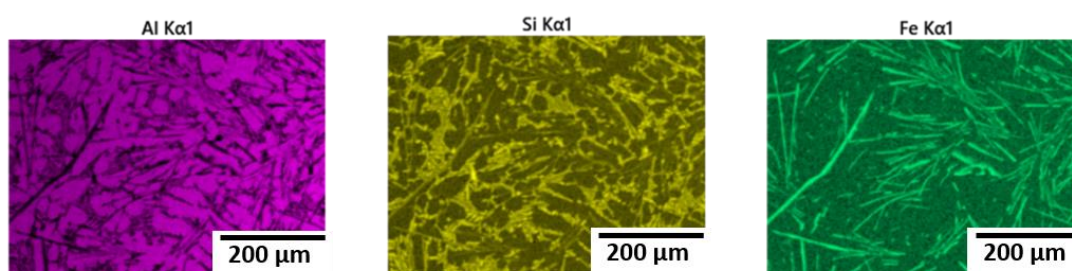


Figure 4.11 EDS elemental mapping of Al-7Si-2Fe (violet colour represents distribution of aluminium, the yellow colour represents distribution of silicon and the green colour represents distribution of iron).

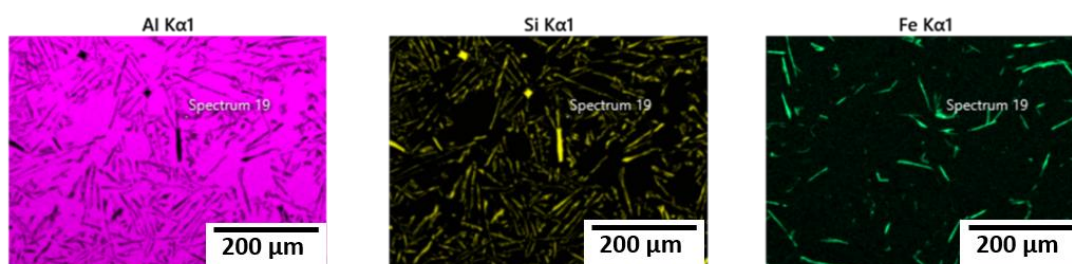


Figure 4.12 EDS elemental mapping of Al-12Si-0.6Fe (violet colour represents distribution of aluminium, the yellow colour represents distribution of silicon and the green colour represents distribution of iron).

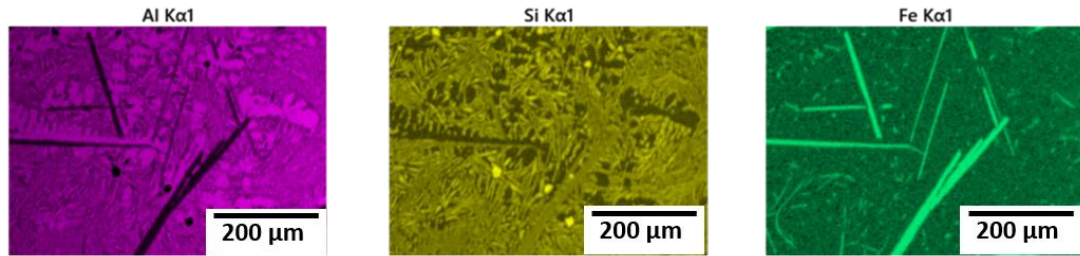


Figure 4.13 EDS elemental mapping of Al-12Si-2Fe (violet colour represents distribution of aluminium, the yellow colour represents distribution of silicon and the green colour represents distribution of iron).

4.3 Mechanical properties

The mechanical testing of the samples were carried out to understand the effect of silicon and iron content in the failure of alloys on tensile loading. Figure 4.14 shows tensile stress vs strain of aluminium alloys. The maximum tensile elongation of Al-0.6Fe alloy is 12.35 ± 1.50 mm and for Al-2Fe alloy is 7.44 ± 0.87 mm whereas the maximum tensile stress is 80.30 ± 2.01 MPa and 94.41 ± 1.81 MPa. This shows that the 2% iron addition resulted in deteriorating the properties of aluminium and aluminium alloys.

Similarly to study the effect of silicon addition, the Al-0.6Fe alloy, Al-7Si-0.6Fe alloy and Al-12Si-0.6Fe alloy can be compared. The maximum tensile elongation of Al-0.6Fe alloy is 12.35 ± 1.50 mm, for of Al-7Si-0.6Fe alloy is 1.78 ± 1.28 mm and for Al-12Si-0.6Fe alloy is 1.40 ± 0.84 mm. The maximum tensile strength of Al-0.6Fe alloy is 80.30 ± 2.01 MPa, for of Al-7Si-0.6Fe alloy is 122.24 ± 3.31 MPa and for Al-12Si-0.6Fe alloy is 89.90 ± 6.24 MPa.

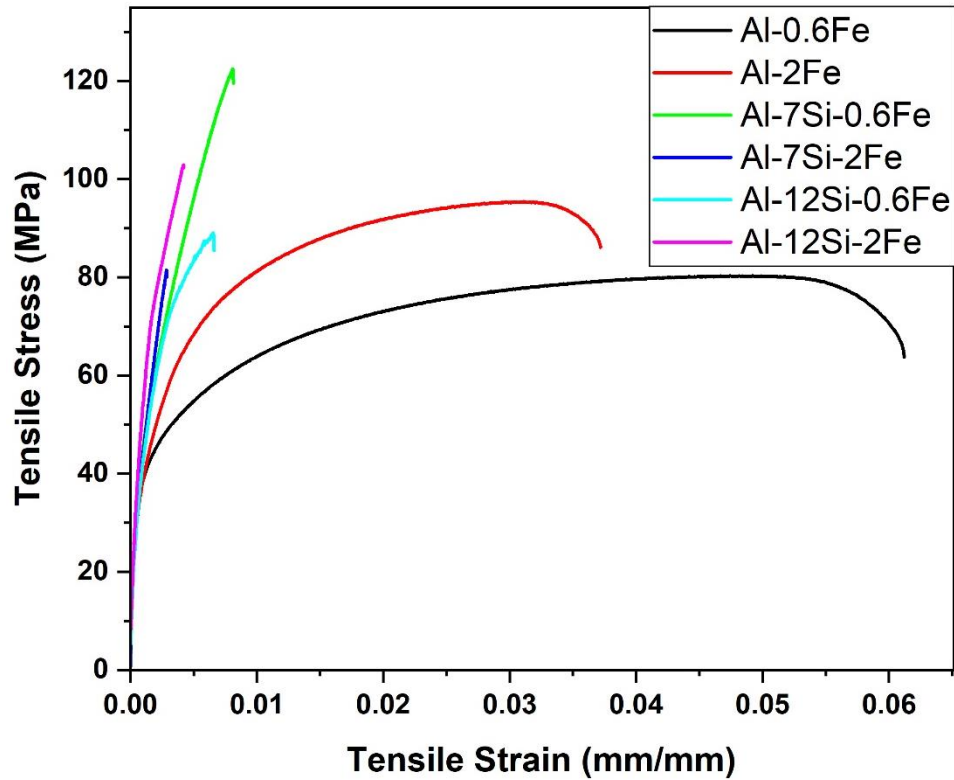


Figure 4.14 Tensile stress vs strain curve of aluminium alloys with different iron and silicon contents

This shows that even though the silicon addition up to eutectic concentration increases the strength of the alloy, it drastically deteriorates the elongation/ductility of the alloy. This could be due to the enhanced formation of iron intermetallic particles by combining with silicon particles. The eutectic alloy Al-12Si-0.6Fe showed a reduction in strength. The eutectic silicon also acts in the deterioration of the mechanical properties.

4.4 Fracture surface analysis

The fracture surface was studied in 2 dimension to understand the type of fracture as this will give a better idea for the effective modification of the intermetallic particles. Figure 4.15 shows the SEM images of the fracture surface of (a) Al-0.6Fe (b)

Al-2Fe (c) Al-7Si-0.6Fe (d) Al-7Si-2Fe (e) Al-12Si-0.6Fe and (f) Al-12Si-2Fe alloys. The brittleness of the alloys is found to be increased with increase in the iron content.

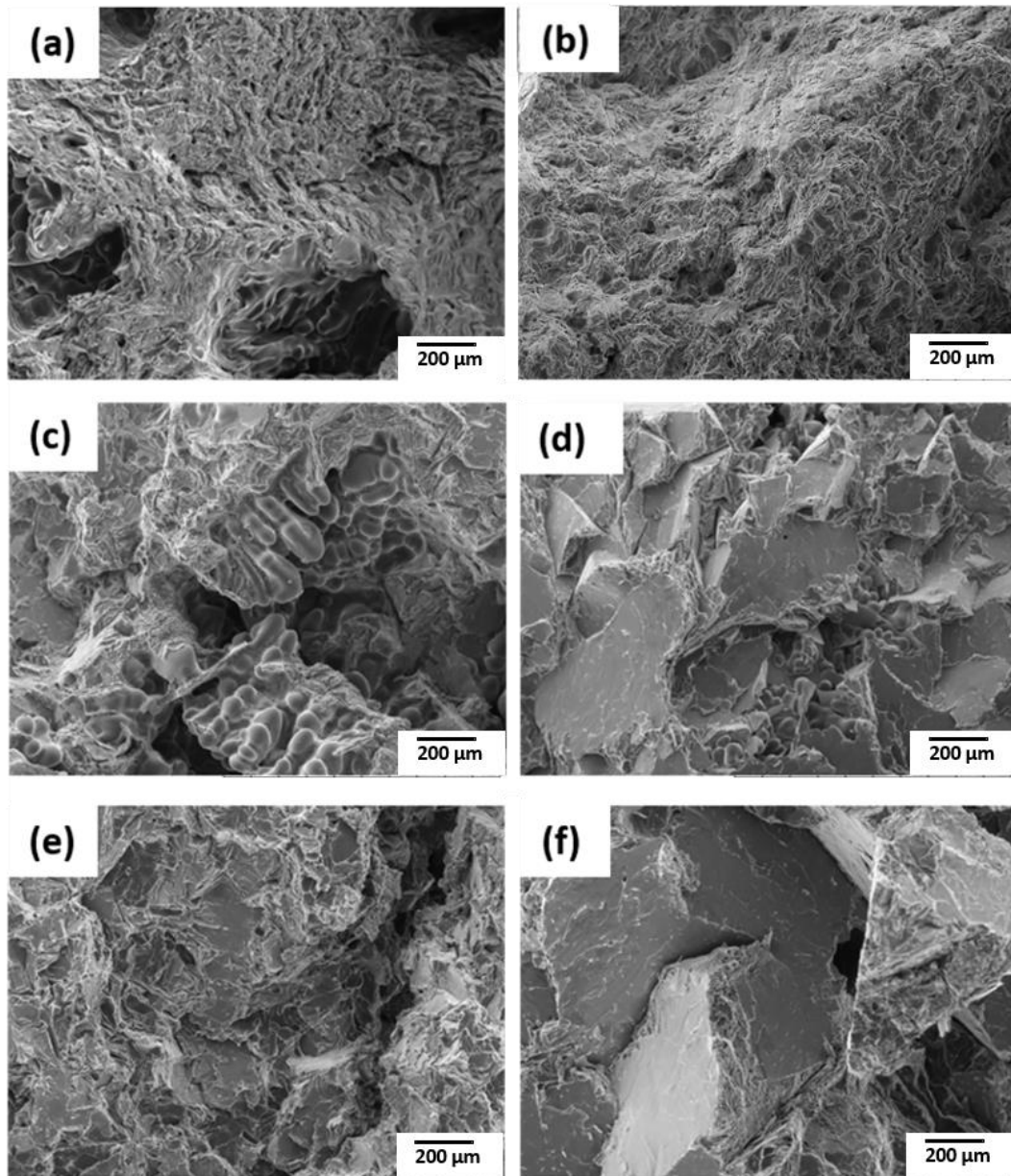


Figure 4.15 SEM image showing the fracture surface in the tensile samples of (a) Al-0.6Fe (b) Al-2Fe (c) Al-7Si-0.6Fe (d) Al-7Si-2Fe (e) Al-12Si-0.6Fe (f) Al-12Si-2Fe alloy.

The nature of fracture surface in Al-0.6Fe alloy (Figure 4.15a) is a pure ductile fracture with stretches and dimples where the aluminium dendrites are stretched out in the dimples. In the fracture surface of Al-2Fe alloy (Figure 4.15b), the grains were

stretched but the dimples were smooth with no stretches or visible primary aluminium dendrites in it. This could be possible due to the intermetallic particle pull out during the fracture on tensile loading. On comparing Al-7Si-0.6Fe (Figure 4.15c) and Al-7Si-2Fe alloys (Figure 4.15d), the one with the low iron content showed a ductile fracture with most of the primary aluminium grains elongated. The dendritic arm is also comparatively more visible. The fracture surface of Al-12Si-2Fe alloy (Figure 4.15f) shows the complete brittle fracture properties with its significant blocky and shiny surface. Whereas the Al-12Si-0.6Fe (Figure 4.15e) have comparatively smaller blocks with discontinuous edges.

This chapter explains the effect of higher silicon content and iron content on the size of iron based intermetallic particles in aluminium. It is evident from the microstructure studies higher the silicon or iron content, thicker the intermetallic particles formed. Also the mechanical properties of aluminium alloys diminishes with the increase in iron and silicon content. The increase in silicon and iron content increases the availability of the same for the formation of brittle β -Al₅FeSi intermetallic particles and thereby reducing its mechanical properties. It is evident from the phase diagram and the solidification sequence, the addition of 2% iron resulted in the nucleation of intermetallic particles prior to the aluminium. The temperature range available for these iron intermetallic particles for solidification (temperature b/w the formation of these phases and solidus) are more compared to the iron intermetallic particles formed in case of 0.6% Fe addition. This gives more time for the growth of iron intermetallic particles. This could be another reason for the bigger intermetallic particles observed in case of 2% Fe addition compared to the 0.6% Fe addition. More detailed studies on the mechanism of fracture and failure of the alloys is explained in chapter 5.

Chapter 5. Mechanism behind the failure of Al-Si alloys due to the iron intermetallic particles

In order to reduce the deleterious effect of the iron intermetallic particles, it is important to understand the mechanism behind the failure of aluminium alloys in presence of iron. This chapter explains in detail, the analysis of a sample undergone tensile failure with pre and post failure studies on the sample.

5.1 Microstructure Analysis

Figure 5.1 shows the SEM images of Al-7Si, Al-7Si-0.6Fe and Al-7Si-2Fe alloys. These images show the 2D morphology of the silicon and iron intermetallic particles. The white particles in the microstructure are iron intermetallic particles and the bright grey particles are silicon flakes. The Al-7Si-0.6Fe microstructure (Figure 5.1b) and Al-7Si-2Fe microstructure (Figure 5.1c) shows the iron intermetallic particles in aluminium matrix. Al-7Si-2Fe is found to have a large number of intermetallic particles, whereas Al-7Si-0.6Fe alloy is found to have only few intermetallic particles. The intermetallic particles were observed to be long needle shaped and were uniformly distributed in the matrix of Al-7Si-2Fe alloy. This shows that the increase in iron content from 0.6%Fe to 2 % Fe resulted in a significant increase in volume fraction of iron intermetallic particles in the alloy.

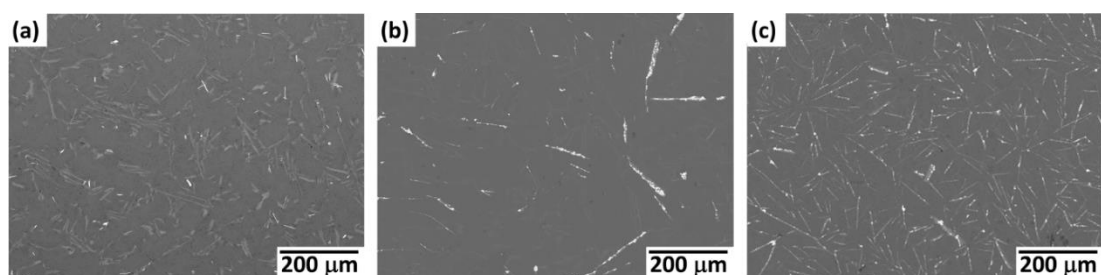


Figure 5.1 SEM images of (a) Al-7Si, (b) Al-7Si-0.6Fe and (c) Al-7Si-2Fe alloys

Figure 5.2 shows the SEM-EDS elemental analysis of Al-7Si alloy, Al-7Si-0.6Fe alloy and Al-7Si-2Fe alloy. The EDS images clearly distinguish the aluminium, silicon and intermetallic phases. As shown in Figure 5.2, the iron intermetallic particles were showing a needle shaped morphology. The iron intermetallic particles are found to be more thick and dense in number in Al-7Si-2Fe alloy (Figure 5.2c) compared to the Al-7Si-0.6Fe alloy (Figure 5.2b). Also, the eutectic silicon was found to be modified and finely distributed in Al-7Si-0.6Fe alloy compared to the Al-7Si-2Fe alloy and Al-7Si alloy (yellow coloured particles in Figure 5.2a, Figure 5.2b and Figure 5.2c).

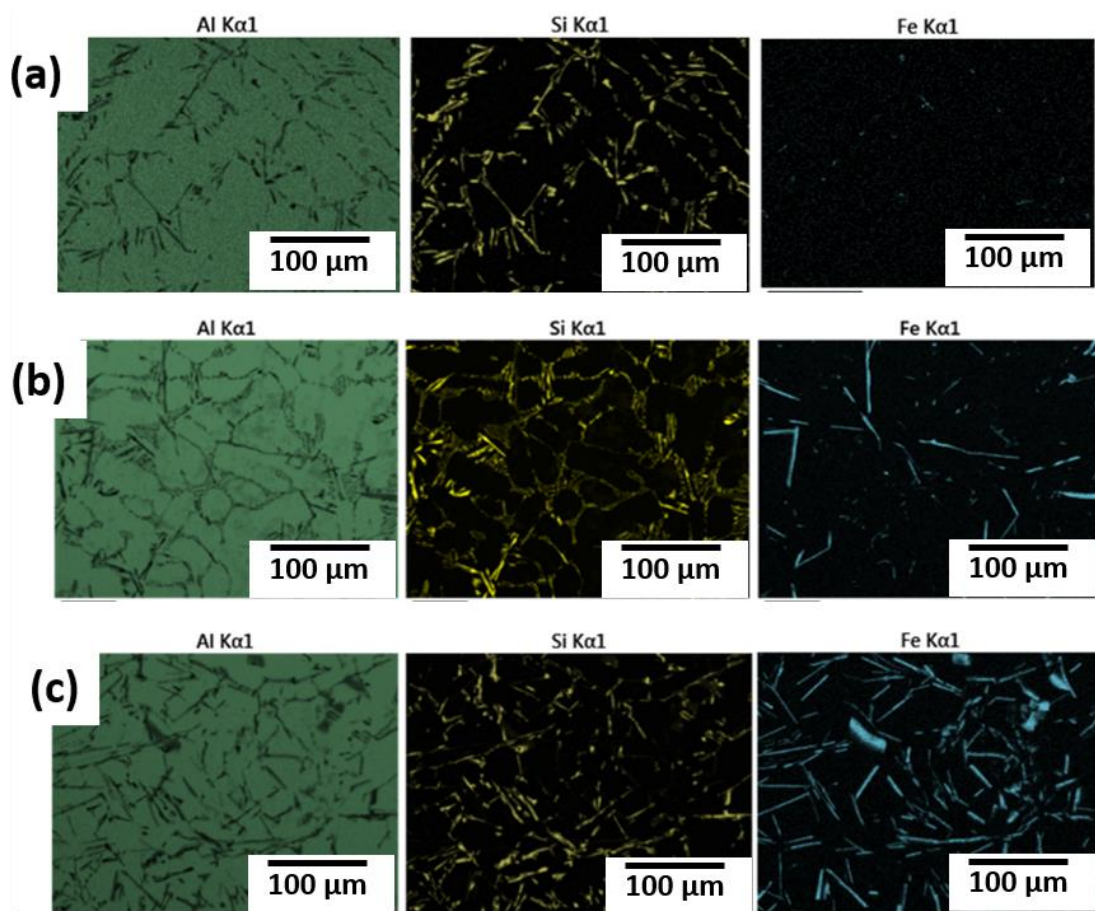


Figure 5.2 SEM-EDS elemental mapping of (a) Al-7Si alloy, (b) Al-7Si-0.6Fe alloy and (c) Al-7Si-2Fe alloy (green colour represents aluminium matrix, yellow colour represents the silicon phase and blue colour represents iron)

This is due to the heterogeneous nucleation of silicon phases on β -iron intermetallic phases[84][45] which is predominant at critical Fe content (Fe_{crit}) which is ~ 0.6 for Al-7Si alloy[24].

Taylor et al.[45] explained this mechanism on the basis of a critical Fe concentration (Fe_{crit}). At the critical iron content (Fe_{crit}), the alloy will solidify in two stages where the ternary β -AlSi eutectic platelets form first and the eutectic silicon cells nucleate only on small ternary β -AlSi platelets. Whereas, at subcritical iron contents ($<Fe_{crit}$) and supercritical iron contents ($>Fe_{crit}$), the alloy solidifies in more than 2 stages. At subcritical iron contents ($<Fe_{crit}$) the large silicon eutectic cells nucleate initially and grow before the nucleation of smaller eutectic cells of the β -AlSi ternary platelets. At supercritical iron contents ($>Fe_{crit}$), the large eutectic silicon cells nucleate on the already formed binary Al-iron intermetallics before the nucleation of small eutectic cells on the ternary β -AlSi ternary platelets. The refinement of silicon particles improves the mechanical properties of aluminium silicon alloys. Hegde et al.[85] reported a noticeable improvement in elongation and strength upon modification of silicon phase in aluminium silicon alloy.

5.2 Mechanical properties

The hardness and elastic modulus of iron intermetallic particles, silicon rich areas and aluminium in Al-7Si-2Fe alloy were determined from their respective loading-unloading curve using the method proposed by Oliver and Pharr[79][78] which is reported in chapter 3. Figure 5.3 shows the loading -unloading curve of different area/particles in Al-7Si-2Fe alloy from which the hardness and elastic modulus were measured. The indentations on the iron intermetallic particles (red colour) attain a maximum depth of ~ 150 nm whereas, indentations on the aluminium (blue colour) attain a maximum depth of ~ 550 nm. The displacement on constant load of 5 mN also shows this increasing nature (top peak of the curves). This indicates the iron intermetallic particles are less ductile/more brittle, than aluminium. The hardness and Young's modulus of the iron intermetallic particle is significantly higher than that of aluminium and silicon flake rich area. The average nano-hardness of the

primary aluminium is 1.05 ± 0.01 GPa and iron intermetallic particles are 9.53 ± 0.18 GPa, whereas average youngs modulus are 102.78 ± 1.97 GPa and 174.30 ± 11.28 GPa respectively. This is almost consistent with the literature from Chen et al.[86] who reported a hardness of 10.82 GPa and 175.32 GPa for iron intermetallic particles in AlSiFeMn alloy by nano indentation. The hardness and Youngs modulus obtained for the primary aluminium is higher than pure aluminium (0.7 GPa and 70 GPa respectively). Youn et al. [87] reported that an average elastic modulus of 77 GPa for primary aluminium in Al-Si alloy and an average nanohardness of 1.0 GPa. However, the average elastic modulus obtained for primary aluminium is higher than that of literature. This could be due to the presence of silicon particles in the alloy.

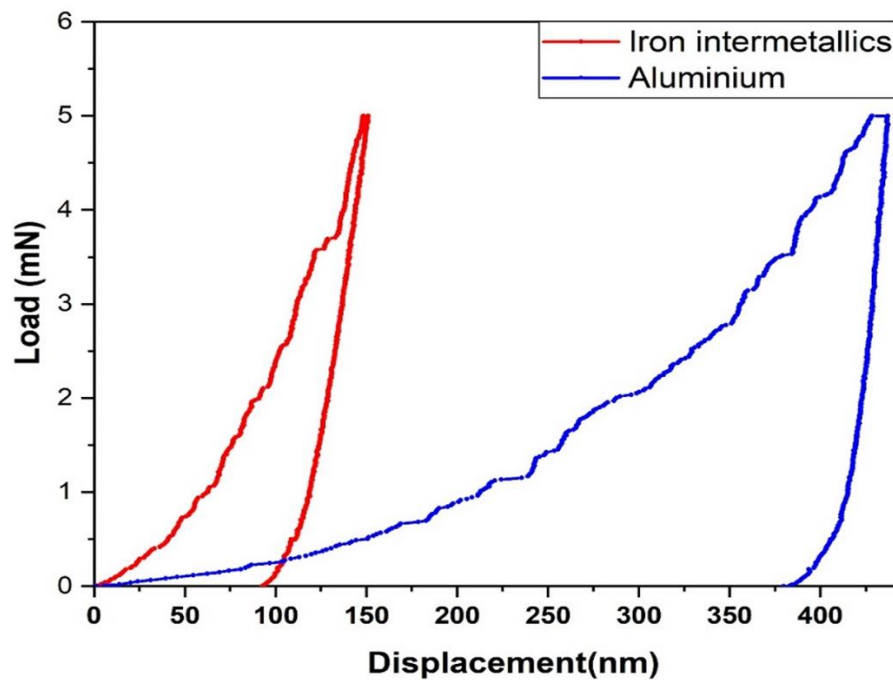


Figure 5.3 Loading –Unloading curve of Al-7Si-2Fe alloy on nano indentation testing.

The tensile properties of Al-7Si, Al-7Si-0.6Fe and Al-7Si-2Fe alloys were measured to determine the effect of intermetallic particles on the mechanical properties of Al-7Si alloys. Figure 5.4 shows the tensile stress vs strain curve of Al-7Si alloy (red colour), Al-7Si-0.6Fe (blue colour) alloy and Al-7Si-2Fe (green colour) alloy. The maximum tensile stress for Al-7Si alloy is 95.01 ± 5.65 MPa, Al-7Si-0.6 Fe alloy is 89.06 ± 1.14 MPa and Al-7Si-2Fe alloy is 70.43 ± 7.78 MPa. This shows that the increase in iron

levels to 2% resulted in a significant drop in tensile properties of the alloy. However, The maximum elongation for Al-7Si alloy was 1.25 ± 0.12 mm, whereas for Al-7Si-2Fe alloy, the the elongation was 0.51 ± 0.08 mm. This shows that the maximum elongation was dropped by 58% with 2 % iron addition to Al-7Si alloy. But the addition of 0.6 % iron results in a maximum elongation of 1.39 ± 0.19 mm. This shows an increase in the elongation by 10.67 % even though the strength is decreased by 6.26 %. This difference in elongation may be due to the critical iron content (Fe_{crit}) of Al-7Si-0.6Fe alloy which refines the silicon particles or the casting defects (porosity) or their combined effect[24,45]. Whereas the higher fraction of iron intermetallic particles formed on addition of 2 wt% Fe significantly deteriorates the mechanical properties of the alloy. Thus it indicates that, even though the iron intermetallic particles form in Al-0.6 % Fe alloy, its effect is negligible in deteriorating the mechanical properties of the alloy. These observations can be correlated with the critical iron content values of Al-7Si alloys [24,49]. Similar observations of reduction in mechanical properties on addition of Fe were reported in other Al-Si based alloys with iron intermetallic particles[70,88,89]. Anantha Narayanan et al. [24] reported that when iron content exceeds 0.7 %, the intermetallic compounds tends to form as large platelets which deteriorate the the mechanical properties of the alloy. Sacinti et al.[88] studied the effect of iron intermetallic particles on the mechanical properties of Al-7Si-0.3Mg and reported that the size of the β platelets was twice when the Fe content is doubled which eventually led to a reduction in the elongation value by 3-fold. Ravi et al.[89] also concluded that higher the Fe content in the alloy, lower the mechanical properties of the alloy.

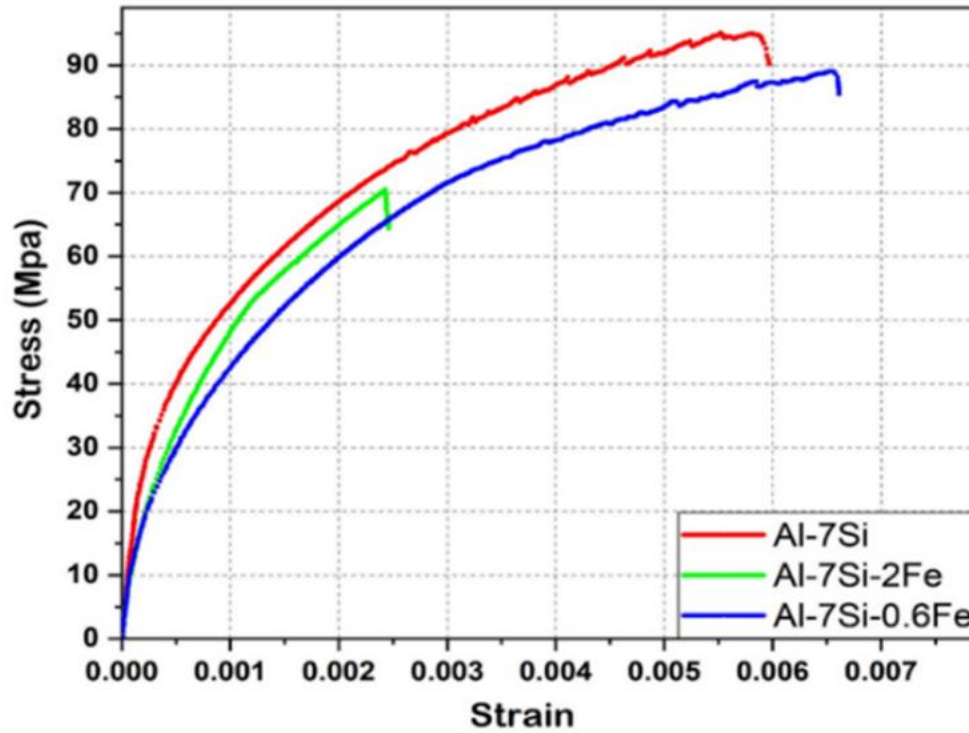


Figure 5.4 Tensile properties, Tensile stress vs strain of Al-7Si with different iron content.

5.3 Fracture surface analysis

Figure 5.5 shows the fracture surface of the tensile samples of Al-7Si and Al-7Si-2Fe alloys. The aluminium dendrites are visible in both cases with no significant damage of primary aluminium in the alloy. The intermetallic particles are clearly visible in Al-7Si-2Fe alloys (Figure 5.5b). The 3rd dimension of the needle shaped particles are visible in the Figure 5.5b. The particles which were reported earlier as needles in SEM images are actually thin platelets in 3D as shown in Figure 5.5b. The platelet shaped particles with sharp edges are projected out from the fracture surface without any rupture. This sharp edged platelet shape increases the stress concentration factor thereby resulting in the formation of cracks at the particle matrix interface in the high iron containing alloy[90,91]. This shows that, during tensile loading the intermetallic particles were pulled out along the interfacial boundary between intermetallic particles and the aluminium matrix without causing any destruction to the brittle intermetallic particles. Also this observation suggests that the early failure of the Al-7Si-2Fe alloy is particularly resulted by the intermetallic particle pullout which in turn

helps in the crack propagation along the particle edges. Wang et al.[92] reported that the large intermetallic particles enhance the crack propagation more than the fragmented intermetallic particles in the alloy. It is also necessary to analyse the fracture surface from the 3 D view and different slices across the fracture surface to support these results, which can be done with a X-ray tomography study .

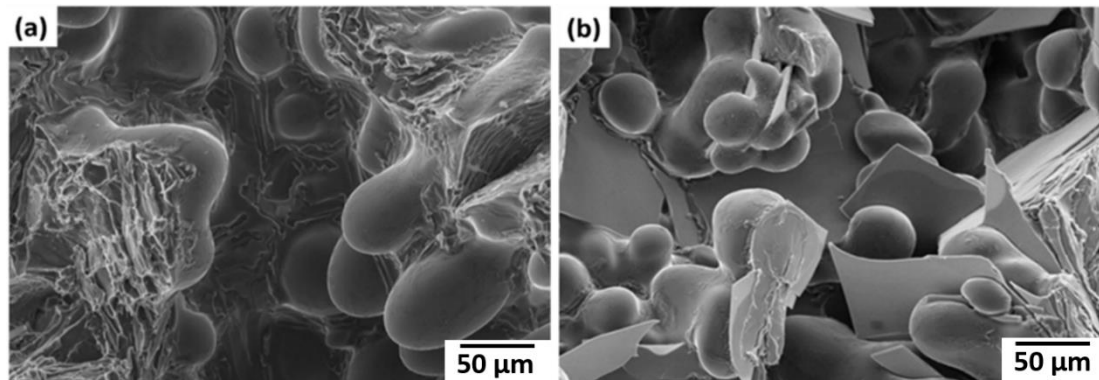


Figure 5.5 Fracture surface in the tensile samples of (a) Al-7Si, and (b) Al-7Si-2Fe alloys cast at 740°C.

5.4 X-ray tomography studies

Further, the fracture surfaces were studied using 3D X-ray tomography for better understanding of early failure of iron containing alloys during tensile testing. Figure 5.6 shows the fracture study of the tensile samples of Al-7Si-2Fe alloys using 2D orthogonal slices (3.5 mm x 3.5 mm) from XCT scan. The 2 dimensional slices from XCT scans were studied using Avizo 9.8 software. Since the cylindrical tensile sample with 6 mm diameter was not easy to analyse due to varying contrast along the cross section, a cuboid subvolume with 3.5 mm x 3.5 mm cross section was made out of 3D reconstructed cylindrical sample. The orthogonal slices from top to the center of the fracture region is as shown in the figure number from left to right respectively. The images shows that that the crack is along the particles (white coloured). Almost all of the cracks are sharp edged, demonstrating a fracture along the sharp edged intermetallic particle boundaries. The results suggest that the intermetallic particles are not fractured on extension, but the sharp corners of intermetallic particles act as

stress risers for initiation and propagation of the crack. The propagation of the crack is through the interface boundary of the particles and aluminium matrix. Since the particles are elongated and interconnected with sharp edges, cracks can easily propagate from one end to the other end.

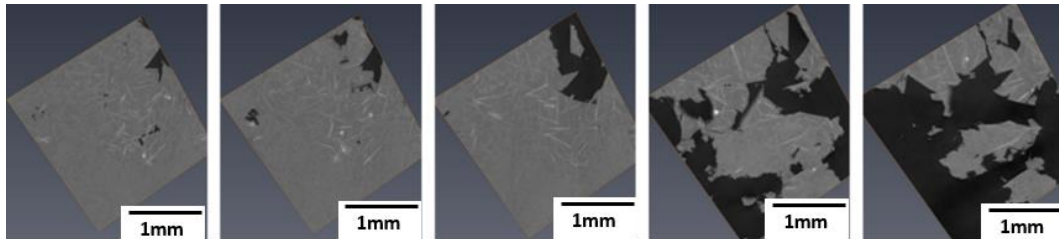


Figure 5.6 2D slices showing the crack propagation (top to centre of the fracture region)

Figure 5.7a shows the 3D reconstructed image of Al-7Si-2Fe alloy. In Figure 5.7, the colour representation are as follows: blue colour represents the porosity, while red and white colour represent iron intermetallic particles and the aluminium matrix respectively. Figure 5.7b shows the 3D reconstructed image of Al-7Si-2Fe alloy without porosities. As shown in Figure 5.7b, $\text{Al}_{13}\text{Fe}_4$ iron intermetallic particles were found to be have a platelet morphology in 3D compared to thier appearace as needles in 2D images. The needle type morphology which appears in the 2 dimension is found to have a 3rd dimension and the particles were observed to be having thin platelet shape with very sharp edges. The failure crack (thick dense blue) was observed to be formed in an area in the sample where iron intermetallic particle presence is higher (Figure 5.7a). The porosity included in the region of failure was removed in Figure 5.7b for a better observation of the fracture area. Also, it is found from the fracture area in the Figure 5.7b (zoomed in) that the crack propagated along the surface of the intermetallic particles without rupture and fracture of the particles. This shows that the early failure of iron containing alloy is not due to the brittleness of intermetallic particles, but due to the morphology of intermetallic particles. Yi et al.[90] reported the crack formation and propagation along the interfaces by de-bonding of Fe-rich intermetallic and Si-particles from the matrix in

the alloy. A similar observation was made by Gall et al.[91] that the fatigue cracks debounded almost all of the silicon particles in Al-Si alloys. Also, it was observed that the fracture occurred at the the elongated particles which has major axis perpendicular to the crack plane.

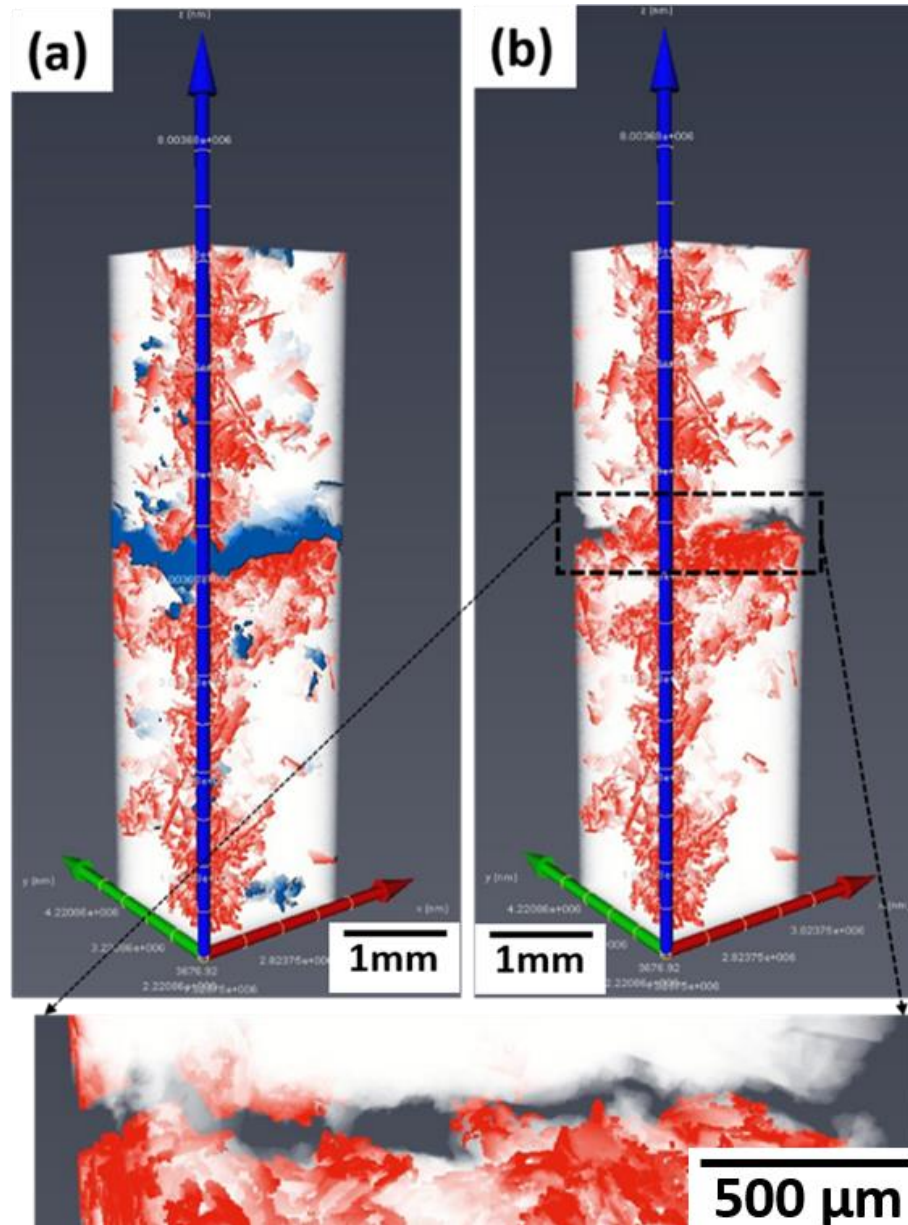


Figure 5.7 3D reconstructed XCT images (a) showing porosity (blue colour) as well as particles (red colour) in Al matrix (white), (b) showing particles (red colour) in Al matrix (white)

This chapter investigates the effect of iron intermetallic particles in the mechanical properties of the Al-7Si alloy and the mechanism of failure of this alloy. The study using the 3D XCT technique clearly shows that the addition of 2 wt% of iron to Al-7Si results in increased volume fraction of iron intermetallic particles which results in decrease in mechanical properties of the alloys. Nano indentation studies show that the iron intermetallic particles are hard and brittle compared to the primary aluminium. 3D visualisation of intermetallic particles is not only showing the morphology of intermetallic particles, but also useful in understanding the early failure of the alloy with higher levels of iron content in it. The 3D study along with fractography suggests that the failure occurs in these alloys is not only due to brittleness of intermetallic particles, but mainly due to the morphology of the intermetallic particles in the alloy. Therefore, methodologies to modify the morphology of intermetallic particles could help in improvement of mechanical properties of recycled Al-Si alloys which is discussed in the chapter 6 and chapter 7.

Chapter 6. Effect of melt treatments in the formation and growth of iron intermetallic particles

As reported earlier in the literature, studies were conducted to determine the effect of melt treatments on the formation and growth of iron intermetallic particles in Al alloys. Among them, the industrially viable processes are controlling cooling rate and superheating the melt for casting. There has not been much research reported on analysis of the microstructure and mechanical properties based on the comparative studies of Al-Fe alloy and Al-7Si-2Fe alloys. Also, it is important to study the superheating effect on iron intermetallic particles. In this chapter, the effect of cooling rate and superheating of the melt is studied for Al-Fe and Al-7Si-Fe alloy. One of the major drawback in superheating is the formation of porosity due to oxidation on superheating. In this chapter, the effect of superheating on porosity is also studied using samples prepared under vacuum conditions.

6.1 Effect of cooling rate on the microstructure and mechanical properties of Al-Fe and Al-7Si-Fe alloys.

Al-0.6Fe, Al-2Fe, Al-7Si-0.6Fe and Al-7Si-2Fe alloys were prepared in a water cooled copper mould, cast iron mould and graphite mould respectively to study the effect of cooling rate on microstructure and mechanical properties. The cooling rate was measured using K type thermocouples dipped in the mould while pouring the molten metal to the mould. The average cooling rate obtained for water cooled copper mould was 120 °C/s (very high cooling rate), cast iron mould was 20 °C/s (high cooling rate) and graphite mould was 5 °C/s (slow cooling rate). The optical microstructure of the samples were studied along with their mechanical properties. The quantified mechanical property analysis will be useful to understand the effectiveness of using different cooling rates for casting.

6.1.1 Optical microscopy

Figure 6.1 shows the microstructure of Al-0.6Fe alloy cast in water cooled copper mould, cast iron mould and graphite mould respectively. Due to the higher cooling rates in water cooled copper mould compared to cast iron and graphite mould, the Al-0.6Fe alloy (Figure 6.1a) have a refined grain structure. Even though the intermetallic particles at 0.6 Fe conditions were very less and not visually comparable, the particle distribution is better in case of water cooled copper mould. This shows the intermetallic particle refinement due to the high cooling rate in water cooled copper mould. The black dots in the Figure 6.1 b represent the porosity in the sample.

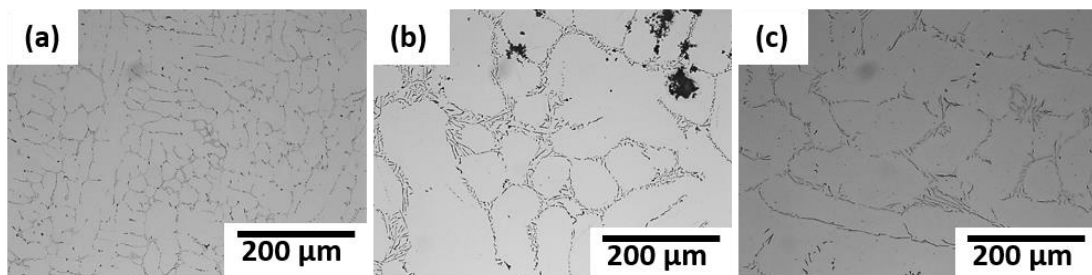


Figure 6.1 Microstructure of Al-0.6Fe alloy cast in (a) watercooled copper mould (b) cast iron mold (c) graphite mould

Figure 6.2 shows the microstructure of Al-2Fe alloy cast in a water cooled copper mould, cast iron mould and graphite mould respectively. The intermetallic particles formed with 2 wt% Fe addition was more in number and bigger in size compared to the 0.6wt % Fe addition. The size of the intermetallic particles formed at high cooling rate (Figure 6.2a) were small compared to the slow cooling cast iron (Figure 6.2b) and graphite mould samples (Figure 6.2c). But the number of particles formed was more in the former compared to the later samples. The high cooling rate in the former reduced the time for the growth of different phases in the alloy, thereby reducing the intermetallic particle size and enhanced the grain refinement of primary

aluminium phase. Even though the slow cooling rate in graphite mould cast sample increases the intermetallic particle growth and its size, the thickness of particle is more in case of cast iron mould cast sample. This could be due to the 2 dimensional view of the intermetallic particle in optical imaging. In case of cast iron sample, the thicker plane of the platelet shaped intermetallic particle is visible, whereas in case of the graphite mould sample, the thinner plane of the intermetallic particle is visible. However the length of the intermetallic particle is more for graphite mould, which indicates the intermetallic particle growth with more time available in the graphite mould due to slow cooling rate.

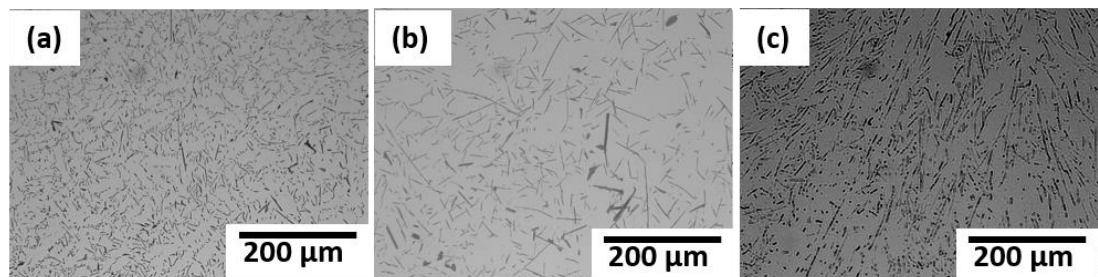


Figure 6.2 Microstructure of Al-2Fe alloy cast in (a) watercooled copper mould (b) cast iron mold (c) graphite mould

Figure 6.3 shows the microstructure of Al-7Si-0.6Fe alloy cast in water cooled copper mould, cast iron mould and graphite mould.

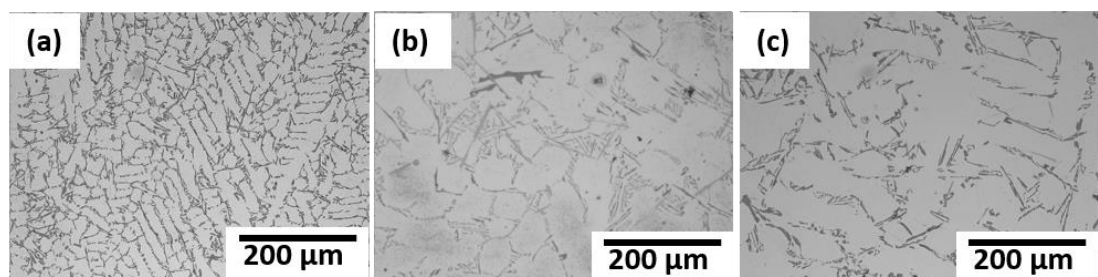


Figure 6.3 Microstructure of Al-7Si-0.6Fe alloy cast in (a) watercooled copper mould (b) cast iron mold (c) graphite mould

The intermetallic particles and primary aluminium phases are much refined in case of water cooled copper mould (Figure 6.3a) compared to cast iron mould (Figure 6.3b) and graphite mould (Figure 6.3c).

Figure 6.4 shows the microstructure of Al-7Si-2Fe alloy cast in a water cooled copper mould, cast iron mould and graphite mould respectively. As expected, the grain size and intermetallic particle size is small for the alloy cast in water cooled copper mould with high cooling rate (Figure 6.4a). But the length of the intermetallic particle is more for the alloy cast in cast iron mould and the thickness of the intermetallic particle is more for the alloy cast in graphite mould.

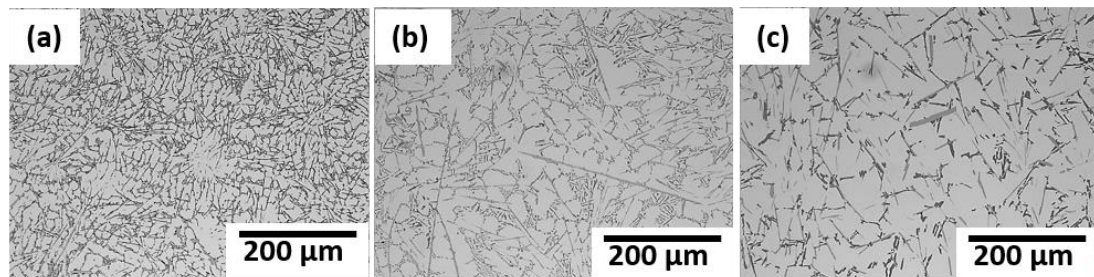


Figure 6.4 Microstructure of Al-7Si-2Fe alloy cast in (a) water cooled copper mould (b) cast iron mold (c) graphite mould

6.1.2 Mechanical properties

The mechanical testing of the samples were carried out to understand the effect of cooling rate in the failure of the alloys on tensile loading. Figure 6.5 shows the tensile stress vs strain of aluminium alloys cast in a water cooled copper mould with high cooling rate and graphite mould with low cooling rate. The trend shows that the alloys cast at a high cooling rate have a better load vs elongation profile compared to the alloys cast at a low cooling rate. This may be due to the refinement of primary aluminium phase and intermetallic particles in copper mould cast alloys.

The maximum tensile elongation of copper cast Al-0.6Fe alloy is 12.35 ± 1.50 mm and graphite cast Al-0.6Fe alloy is 10.58 ± 1.15 mm, whereas the maximum tensile stress is 80.30 ± 2.01 MPa and 76.55 ± 1.80 MPa respectively. This shows a 14.14% increase in elongation and 4.04% increase in strength for the Al-0.6Fe alloy, on increasing the cooling rate from 5 °C/s to 120 °C/s.

The maximum tensile elongation of fast cooled Al-2Fe alloy is 7.44 ± 0.87 mm and slow cooled Al-2Fe alloy is 8.22 ± 2.15 mm, whereas the maximum tensile stress is 94.41 ± 1.81 MPa and 92.41 ± 4.80 MPa respectively. This shows a 10.48% decrease in elongation and 2.16% increase in strength for the Al-2Fe alloy, on increasing the cooling rate. The standard deviation of the mechanical property values for the Al-2Fe alloy is high, probably due to the bigger intermetallic particles formed in alloy on slow cooling. Eventhough the bigger intermetallic particles can add strength to the alloy, it can also cause an early failure of the alloys resulting in an uncertainty in the mechanical property measurement. However due to the higher hardness and elastic modulus of intermetallic particles, the strength of the alloy is more for 2% Fe addition compared to the 0.6%Fe addition.

The maximum tensile elongation of fast cooled Al-7Si-0.6Fe alloy is 1.78 ± 1.28 mm and slow cooled Al-7Si-0.6Fe alloy is 1.39 ± 0.19 mm, whereas the maximum tensile stress is 122.24 ± 3.31 MPa and 89.06 ± 1.14 MPa respectively. This shows a 28.05% increase in elongation and 37.25% increase in strength for the Al-7Si-0.6Fe alloy on increasing the cooling rate.

The maximum tensile elongation of the fast cooled Al-7Si-2Fe alloy is 0.91 ± 0.86 mm and slow cooled Al-7Si-2Fe alloy is 0.51 ± 0.08 mm, whereas the maximum tensile stress is 102.95 ± 4.25 MPa and 70.43 ± 7.78 MPa respectively. This shows a 78.43% increase in elongation and 46.17% increase in strength for the Al-7Si-Fe alloy on increasing the cooling rate from 5 °C/s to 120 °C/s. But there is a reduction of 48.8% in tensile elongation and 15.78% in tensile strength on comparing the fast cooled Al-7Si-2Fe alloy with fast cooled Al-7Si-0.6Fe alloy.

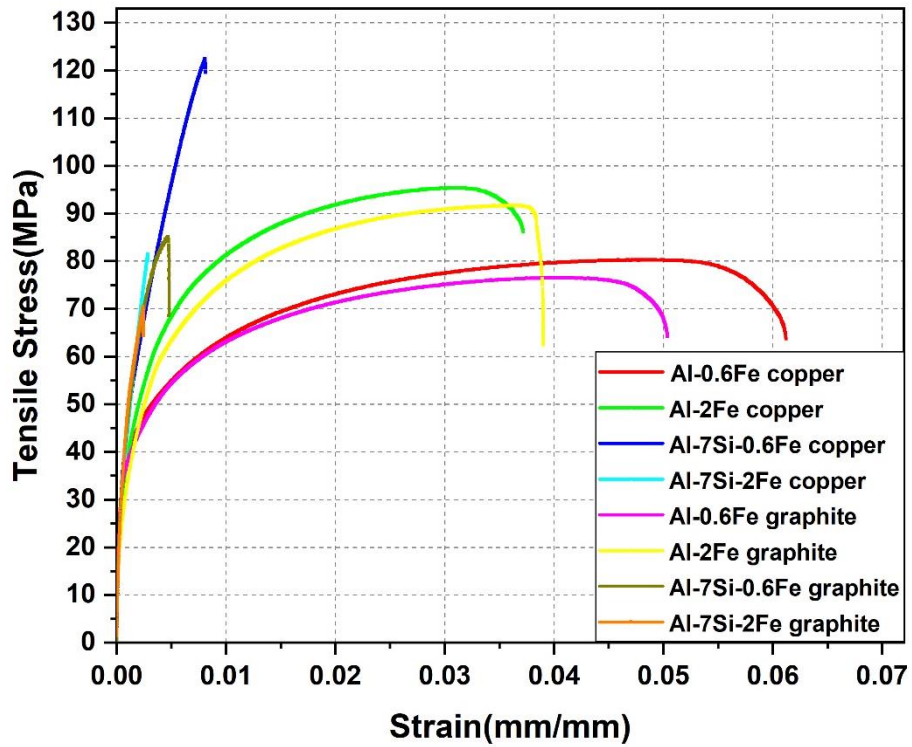


Figure 6.5 Tensile stress vs Strain curve of aluminium alloys with different cooling rate

The results from the Al-7Si-Fe alloys, show that the high cooling rate has a significant effect on the mechanical properties of these alloys compared to the graphite mould. This is mainly due to the refinement of iron intermetallic particles present in these alloys. Even though the microstructure analysis could confirm the refinement and improvement of internal microstructure in Al-7Si-2Fe alloy with high cooling rate, the mechanical property analysis is not showing noticeable improvement compared to the Al-7Si-0.6Fe alloy. Therefore, as the cooling rate increases the size of intermetallic particles decreases and the mechanical property increases. But with increase in iron content, the mechanical property still diminishes.

6.2 Effect of superheat on the microstructure and mechanical properties of Al-7Si-2Fe alloy

This section analyses the effect of superheating the Al-7Si-2Fe alloy at 700°C, 800°C and 900°C. In order to better understand the effect of iron on microstructure and mechanical properties, Al-7Si alloy is also studied under same conditions. The morphological modifications and the porosity formation along with the quantified data is analysed using X-ray computed tomography.

6.2.1 Microstructure Analysis

Figure 6.6 shows the optical images from Al-7Si alloy and Al-7Si-2Fe alloy with a melt temperature of 700°C. Addition of 2wt % iron increased the porosity in the alloy.

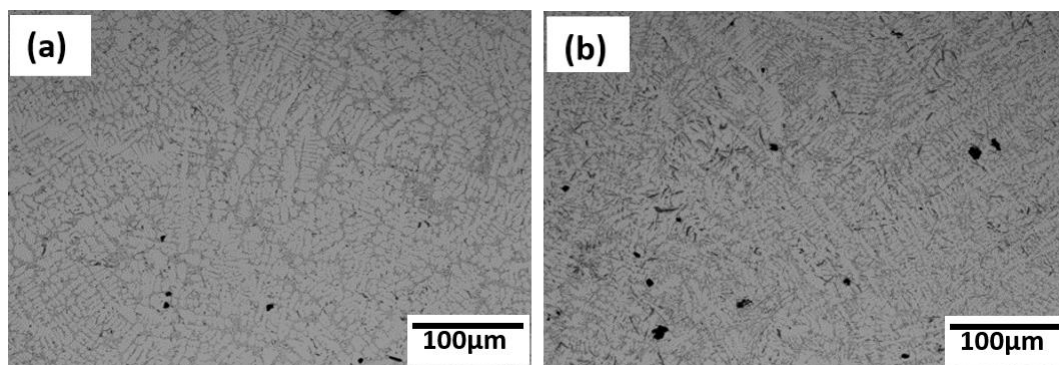


Figure 6.6 Microstructure of alloys cast with a melt temperature of 700 °C (a) Al-7Si (b) Al-7Si-2Fe

Figure 6.7 shows the optical images from Al-7Si alloy and Al-7Si-2Fe alloy with a melt temperature of 800°C. Addition of 2wt % iron to the Al-7Si alloy increased the porosity and intermetallic particle size.

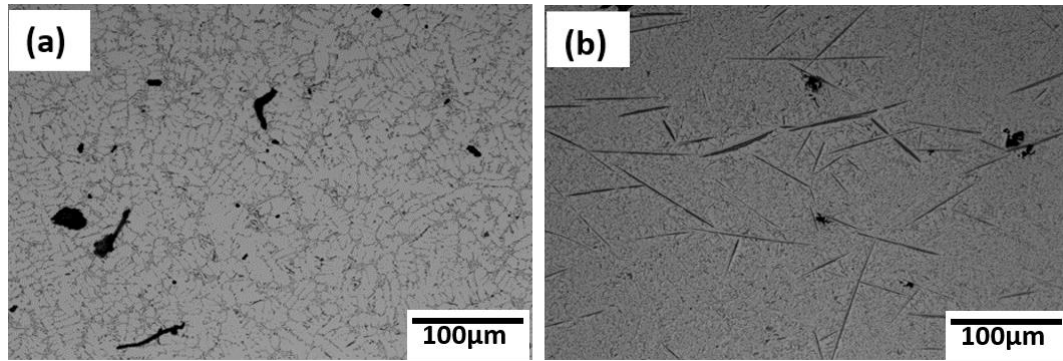


Figure 6.7 Microstructure of alloys cast with a melt temperature of 800 °C (a) Al-7Si (b) Al-7Si-2Fe

Figure 6.8 shows the optical images from Al-7Si alloy and Al-7Si-2Fe alloy with a melt temperature of 900°C. Addition of 2wt % iron to the Al-7Si alloy refines α -aluminium grains in the microstructure but increases the porosity. The optical microscopy investigation of the Al-7Si alloy and Al-7Si-2Fe alloy under different superheat conditions showed the intermetallic particles are more prominent in 800°C compared to other superheat conditions.

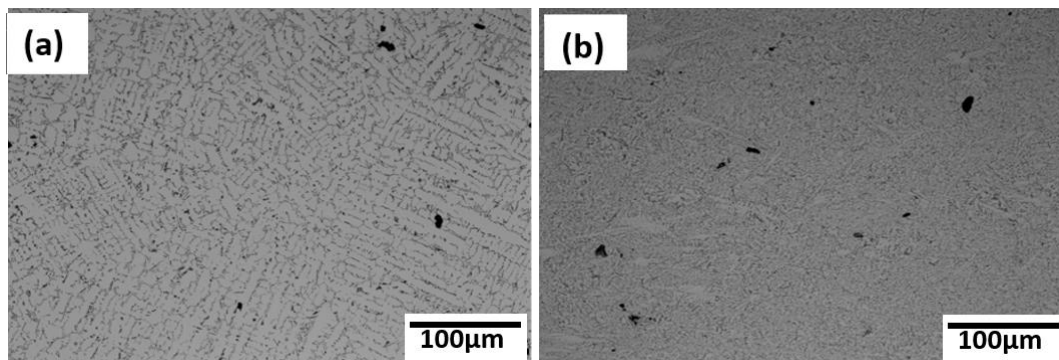


Figure 6.8 Microstructure of alloys cast with a melt temperature of 900°C (a) Al-7Si (b) Al-7Si-2Fe

A detailed investigation of the elemental composition in the microstructure is carried out using the SEM-EDS image of the specimens. The major advantage of SEM-EDS images over optical images is, it clearly distinguish the iron intermetallic particles and silicon particles. Figure 6.9-6.11 shows the elemental mapping of Al, Si and Fe phases in Al-7Si alloy under different superheat conditions.

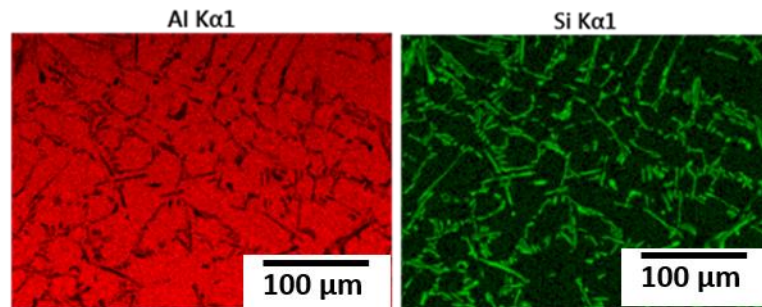


Figure 6.9 SEM elemental analysis of Al-7Si alloy cast with a melt temperature of 700°C (red colour shows the distribution of aluminium, the green colour shows the distribution of silicon).

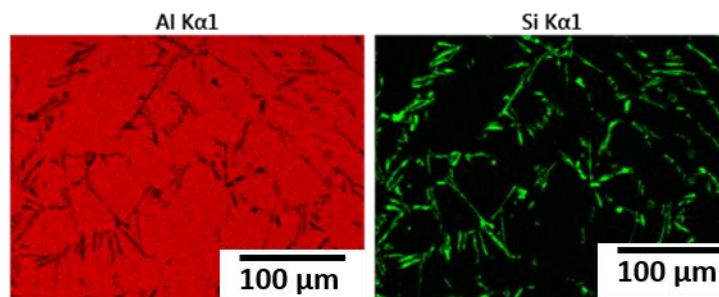


Figure 6.10 SEM elemental analysis of Al-7Si alloy cast with a melt temperature of 800°C (red colour shows the distribution of aluminium, the green colour shows the distribution of silicon).

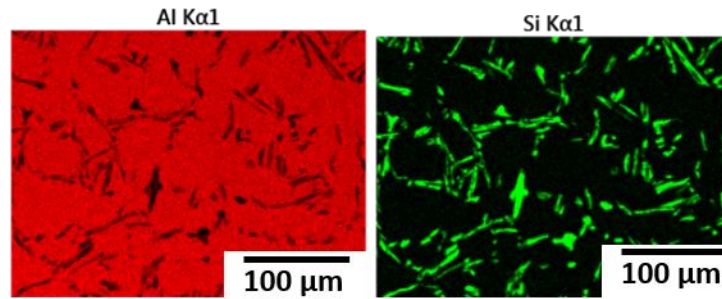


Figure 6.11 SEM elemental analysis of Al-7Si alloy cast with a melt temperature of 900°C (red colour shows the distribution of aluminium, the green colour shows the distribution of silicon).

The images show thickening of silicon particles on superheating. This could be due to the increase in solidification temperature range due to superheating. The increase in solidification temperature range increases the time for growth of silicon flakes formed during solidification.

But more investigation is required to quantify the actual particle size and porosity formation. The quantification of the particle size and porosity is carried out with XCT analysis and is reported later.

Figure 6.12-6.14 shows the elemental mapping of Al, Si and Fe in Al-7Si-2Fe alloy under different superheat conditions. In the presence of iron, the nature of growth of silicon phases and iron intermetallic particles is found to be different with different superheating. The iron intermetallic particles are much bigger and thicker when the Al-7Si-2Fe alloy is heated to 800°C compared to 700°C, whereas super heating to 900°C results in refinement of iron intermetallic particles (Figure 6.14). The silicon particles also show the same behaviour as iron intermetallic particles. The rapid nucleation of iron intermetallic particles in the alloys cast at 900°C results in the formation of large number of finer intermetallic particles which act as nucleation sites for silicon particles. This multiple nucleation events of silicon particles results in the formation of finer silicon particles.

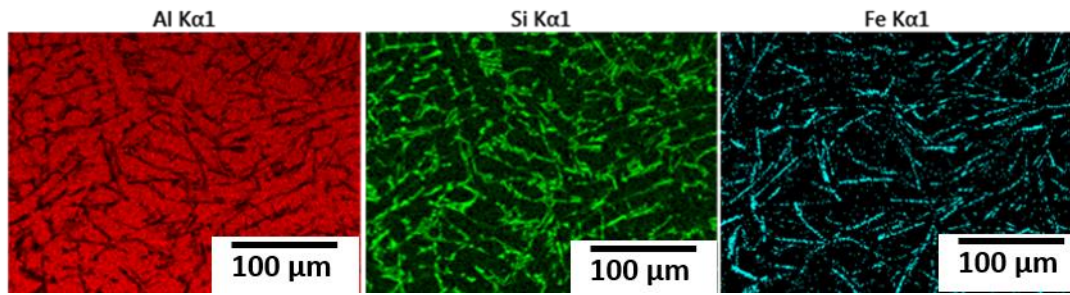


Figure 6.12 SEM elemental analysis of Al-7Si-2Fe alloy cast with a melt temperature of 700°C (red colour shows the distribution of aluminium, the green colour shows the distribution of silicon, the blue colour shows the distribution of iron).

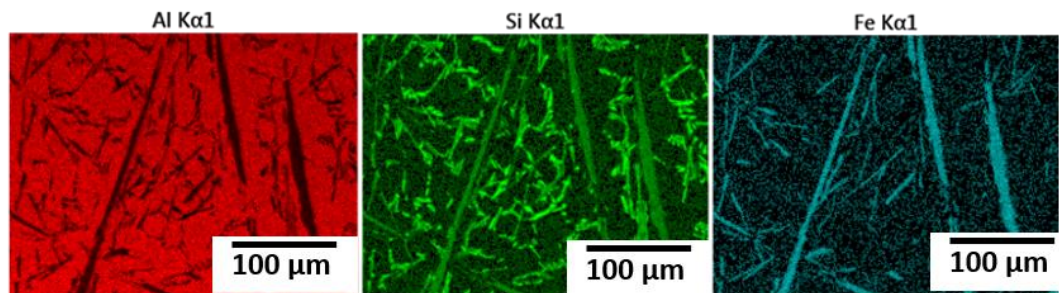


Figure 6.13 SEM elemental analysis of Al-7Si-2Fe alloy cast with a melt temperature of 800°C (red colour shows the distribution of aluminium, the green colour shows the distribution of silicon, the blue colour shows the distribution of iron).

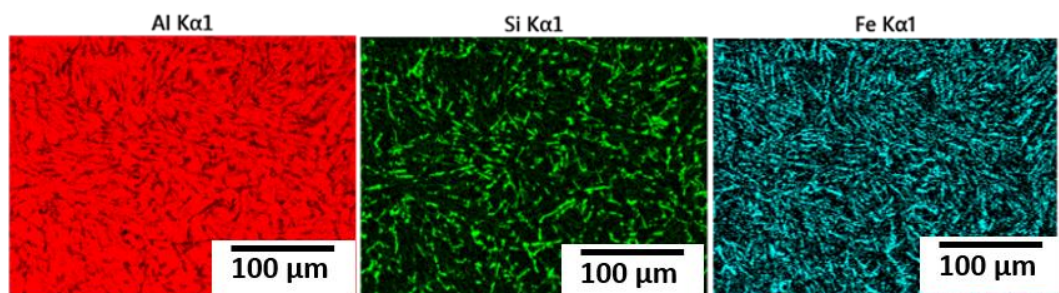


Figure 6.14 SEM elemental analysis of Al-7Si-2Fe alloy cast with a melt temperature of 900°C (red colour shows the distribution of aluminium, the green colour shows the distribution of silicon, the blue colour shows the distribution of iron).

The mechanism behind this particular behaviour in the formation of needle shaped iron intermetallic particles is explained by Samuel et al.[49]. γ -aluminium oxide particles forms at low superheats which act as nucleation sites for the intermetallic particles during solidification. But at high superheats (which is above 800°C for 2% iron), γ -aluminium oxide present in the alloy melt transforms to α -aluminium oxide, which is not a good nucleus for the iron intermetallic particles. This leads to a decrease in the nucleation potential for the iron intermetallic particles. Whereas, when the melt is superheated at 800°C, intermetallic particles nucleates and grow on the γ -aluminium oxide particles. Since the temperature change required to start the solidification in 800°C is more compared to 700°C, the particles will get more time to grow and the size increases. When the melt is superheated at 900°C, the time required for the transformation of α -aluminium oxide to γ -aluminium oxide is less[93]. The nucleation and growth of intermetallic particles starts on or near α -aluminium dendrites [26]. Since the nucleation sites on α -aluminium dendrites is more, rate of nucleation increases resulting in the formation of large number of finer intermetallic particles.

6.2.1 Three Dimensional X-ray computed tomography

The Figure 6.15 shows the 3 D reconstructed X-ray CT images of Al-7Si alloys cast at 700°C and 900°C respectively. The grey coloured structure represents the aluminium silicon alloy matrix and the blue coloured structures represents the porosity. The amount of porosity is found to increase with the increase in superheating by 200°C.

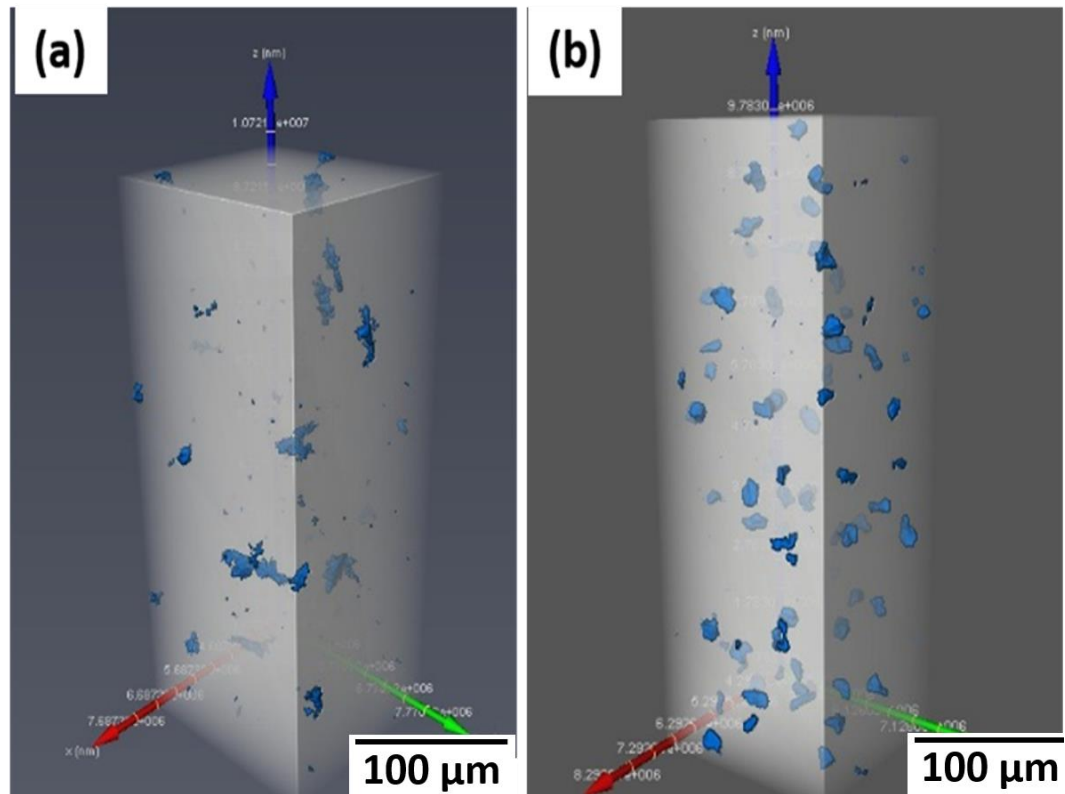


Figure 6.15 3D reconstructed x-ray CT images of Al-7Si alloys cast at (a) 700 °C and (b) 900 °C.

Figure 6.16 shows the 3 D reconstructed X-ray CT images of Al-7Si-2Fe alloys cast at 700°C and 900°C respectively. The white coloured structure represents the aluminium silicon alloy matrix, the red coloured features represent iron intermetallic particles and the blue coloured features represent the porosity. The iron intermetallic particles were found to have a big platelet shape with sharp edges at 700°C, whereas the intermetallic particles found to be refined at 900°C resulting in a large number of smaller structures. The porosity is not clearly visible in these images since the intermetallic particles blocks the view of porosity. But from the Figure 6.17a, it is clear that the porosity formed at 700°C is primarily associated with the intermetallic particles.

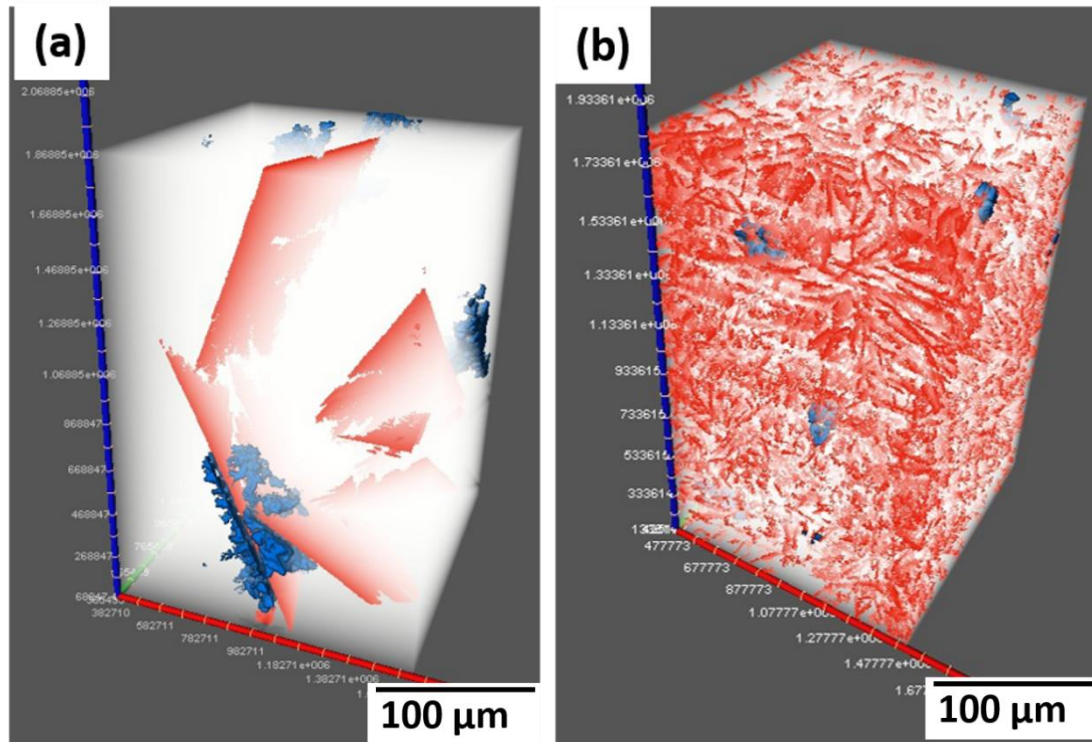


Figure 6.16 3D reconstructed x-ray CT images of Al-7Si-2Fe alloys cast at (a) 700°C and (b) 900°C.

A detailed analysis of the structure and quantification of porosity is needed to further explain about the formation of porosity.

The Figure 6.17 shows the particle size distribution of Al-7Si-2Fe alloy at 700°C and 900°C. Most of the intermetallic particles are interconnected and therefore the accurate measurement of particle size is difficult. More than 70% of the particles lie under the size of 30-40 microns after superheating at 900°C whereas more than 50% particles at 700°C is bigger than 50 microns. Approximately 20% of the particles are bigger than 200 microns on casting at 700°C, which shows the effective refinement of intermetallic particles upon superheating at 900°C.

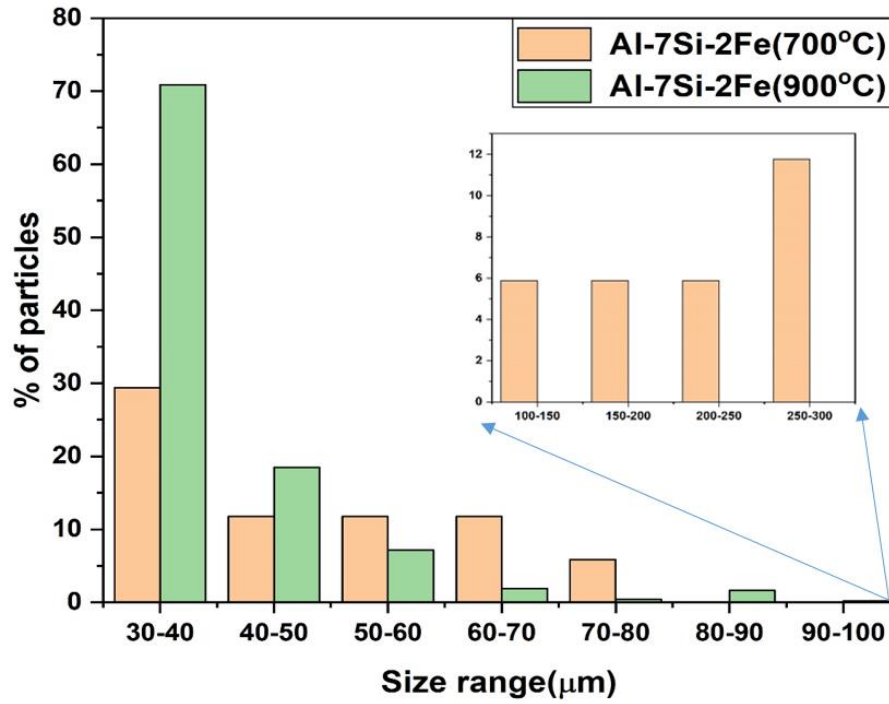


Figure 6.17 Particle distribution in Al-7Si-2Fe alloys cast at 700°C and 900°C.

The Figure 6.18 shows the 3 D reconstructed X-ray CT images of the porosities in Al-7Si alloys and Al-7Si-2Fe alloys cast at 700°C and 900°C respectively. The blue coloured features represents the porosity. The porosities formed in Al-7Si-2Fe alloys are not symmetrical and cannot be considered as gas porosities. The volume of the pores in this figure is used to calculate the pore size distribution in the alloy, shown in the Figure 6.19.

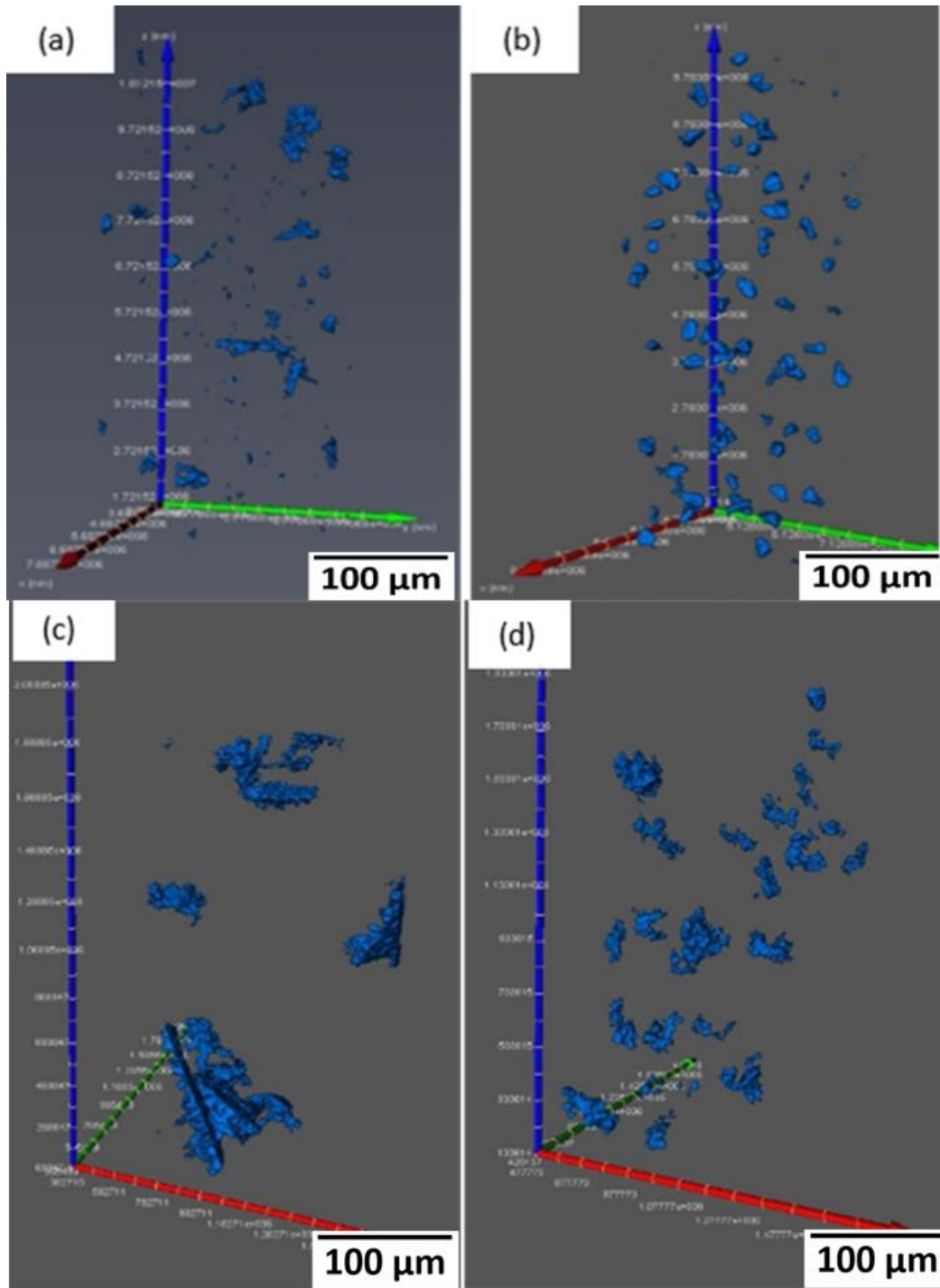


Figure 6.18 3D reconstructed x-ray CT images of (a) Al-7Si alloy cast from melt of 700°C (b) Al-7Si alloy cast from melt of 900°C (c) Al-7Si-2Fe alloy cast melt of 700°C (d) Al-7Si-2Fe alloy cast from melt of 900°C.

The Figure 6.19 shows the pore size distribution of Al-7Si alloy and Al-7Si-2Fe alloy. The porosities below the size range of 10 μm can be neglected as noises present in the imaging or processing. Al-7Si alloy has more number of pores at 900°C compared

to the 700°C. This may be due to increased solubility of hydrogen on superheating. Even though the number of pores in Al-7Si-2Fe alloy after superheating is high, the size of pores are much small compared to the 700°C. The size of pores formed on 700°C is twice that of pores formed on superheating. The largest pore observed in 900°C is in the 30-35 μm range, whereas at 700°C pores bigger than 35 μm are observed and the largest pore is 52.6 μm . This may be due to the bigger sized intermetallic particles formed at 700°C. From the Figure 6.19 (a) and Figure 6.19 (c), it is clear that the pores are formed along the surface of the intermetallic particles and in between intermetallic plates. These pores may be formed during the solidification due to the incomplete flow of liquid metal. When the intermetallic plates grow big, due to its higher surface area it restricts/blocks the flow of liquid metal resulting in the formation of bigger pores between them.

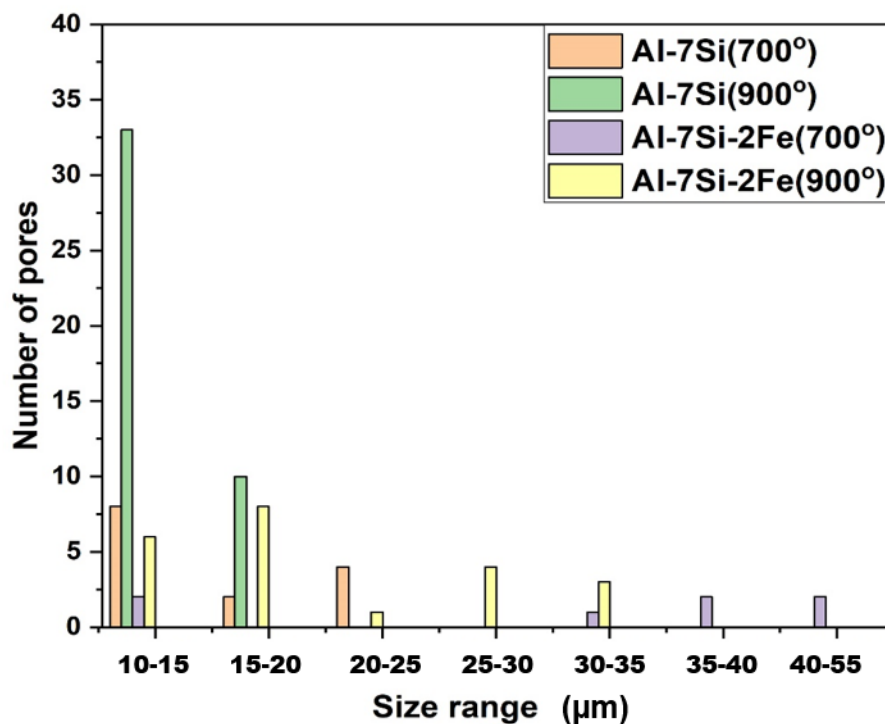


Figure 6.19 Porosity distribution of Al-Si and Al-Si-Fe alloys

6.2.2 Mechanical property analysis

The optical microstructure, SEM and 3D tomography shows the intermetallic particle refinement on superheating at 900°C. Although, the particle and pore size is decreased after superheating to 900 degree, the number of pores and particles are more than the number of pores and particles formed on 700°C casting. Also, the particles formed on superheating at 800°C was much bigger compared to 700°C. Therefore, it is important to test the tensile properties to analyse the improvement in the mechanical properties. Figure 6.20 shows the tensile stress vs strain curves of Al-7Si alloys and Al-7Si-2Fe alloys cast at 700°C, 800°C and 900°C. The tensile curves of Al-7Si alloys shows the maximum stress and strain is more for the alloy cast at 700°C, compared to 800°C and 900°C. This may be due to the increased porosity formed on superheating.

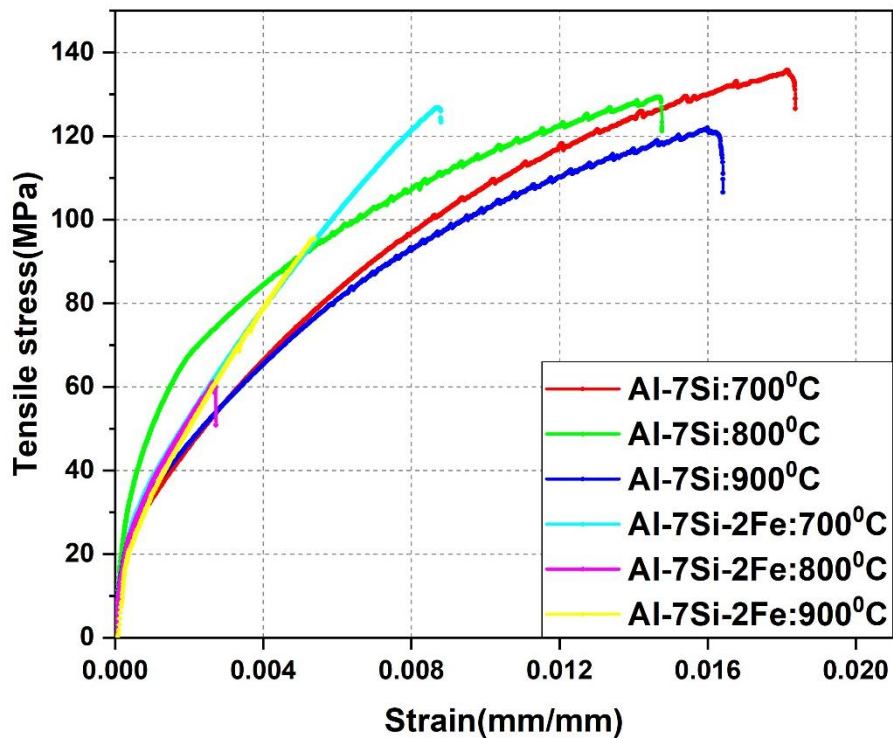


Figure 6.20 Tensile stress vs strain curve on tensile loading of Al-Si and Al-Si-Fe alloys

The superheating increases the hydrogen solubility in aluminium and thereby results in the formation of porosity. But the tensile curves of Al-7Si-2Fe alloy shows the maximum load and elongation obtained for superheating at 900°C is less compared to 700°C and more compared to 800°C. This could be due to the particle refinement on casting a 900°C although the porosity is much higher at 900°C. Even though the number of particles at 900°C are more, the orientation and size of particles may not be favourable for the crack to propagate as in case of large particles.

Figure 6.21 shows the DSC curve for Al-7Si-2Fe alloys cooled from 700°C and 900°C. The exothermic peak, sited at 590°C exists for both the case, but the enthalpy value corresponding to this peak increases for the alloy cooled from 700°C. Therefore, it can be inferred that the intermetallic phase formed at 590°C, still exists in case of the alloy cooled from 900°C. But in case of 700°C, the intermetallic particles get more time to grow and hence form bigger iron intermetallic particles.

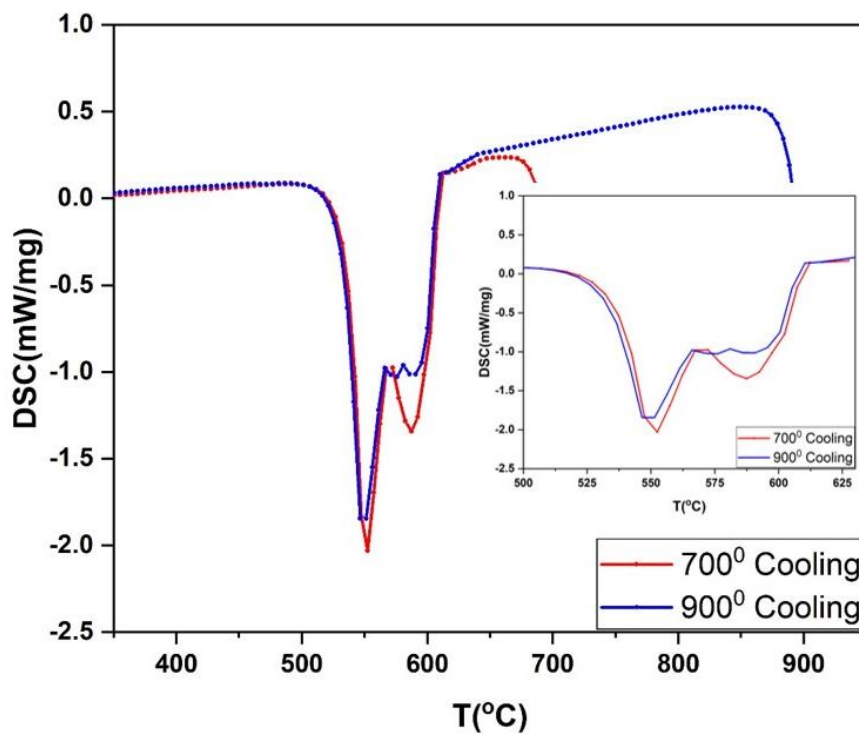


Figure 6.21 DSC curve for Al-7Si-2Fe alloys cast at 700 °C and 900 °C.

6.3 Vacuum induction casting of aluminium alloys

Even though, superheating is effective in refining the intermetallic particles, one of the major limitations with the superheating is the enhanced oxidation at high temperatures which results in increased porosity. It is important to study the porosity formation on superheating and the resulted improvement in mechanical properties. But as reported in the literature, the intermetallic particles can affect the castability of aluminium alloys. Therefore it is essential to identify the porosity formed due to high temperature oxidation and quantify them to analyse the advantage of using inert/vacuum atmosphere for superheating. Vacuum cast Al-7Si alloy and vacuum cast Al-7Si-2Fe alloy at 900°C can be compared to understand the effect of intermetallic formation and castability. Vacuum melted Al-7Si-2Fe alloy at 700°C and vacuum melted Al-7Si-2Fe alloy at 900°C can be compared to understand the effect of superheating in intermetallic particle formation and oxidation on vacuum atmosphere.

6.3.1 Optical microscopy

Figure 6.22 shows the optical microscopy images from Al-7Si alloy cast under vacuum at melt temperature of 700°C and 900°C respectively. There is no visible pores in both the conditions. This is due to the vacuum conditions for the casting which prevents the oxidation and vaporizes the gases present in the raw materials allowing them to escape.

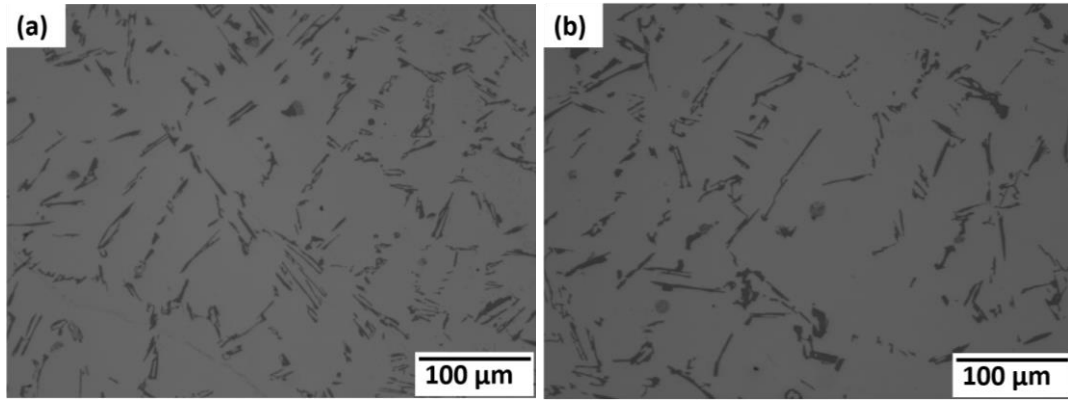


Figure 6.22 Optical microstructure of Al-7Si alloys cast at (a) 700°C (b) 900°C

Figure 6.23 shows the optical microscopy images from Al-7Si-2Fe alloy cast under vacuum at melt temperatures of 700°C and 900°C respectively. The 2wt % iron addition to the Al-7Si alloy refined α -aluminium grains in the microstructure but increased the porosity and generated the intermetallic particles. The quantification of the particle size and porosity is carried out with XCT analysis and is reported later.

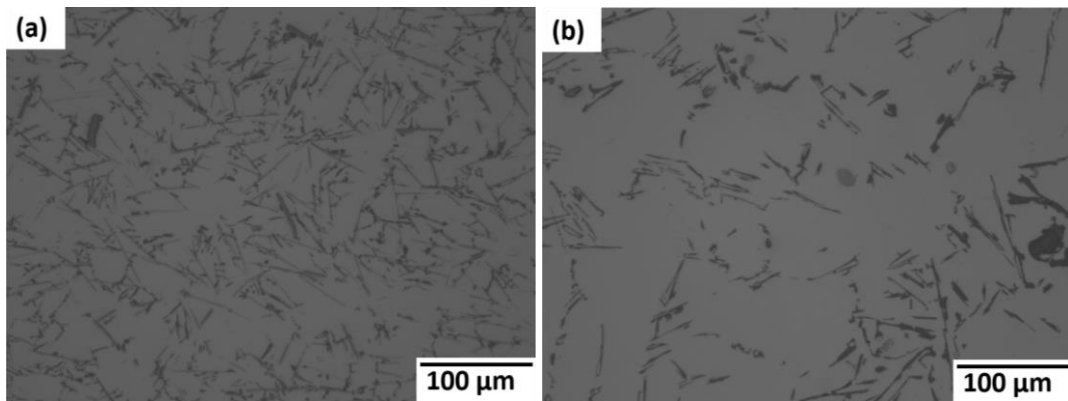


Figure 6.23 Optical microstructure of Al-7Si-2Fe alloys cast at (a) 700°C and (b) 900°C

Figure 6.24 shows the 3D reconstructed X-ray CT images from Al-7Si and Al-7Si-2Fe alloy cast under vacuum at melt temperatures of 700°C and 900°C respectively. Tensile samples scanned using X-ray CT and the 2D images were stacked together to reconstruct the 3D images. The largest possible cuboid shaped subsamples were cropped out from these 3D cylindrical images to remove the outside border of the

cylinder which has a distinctive contrast. The grey coloured structure represents the aluminium matrix and the blue coloured features represents the porosity.

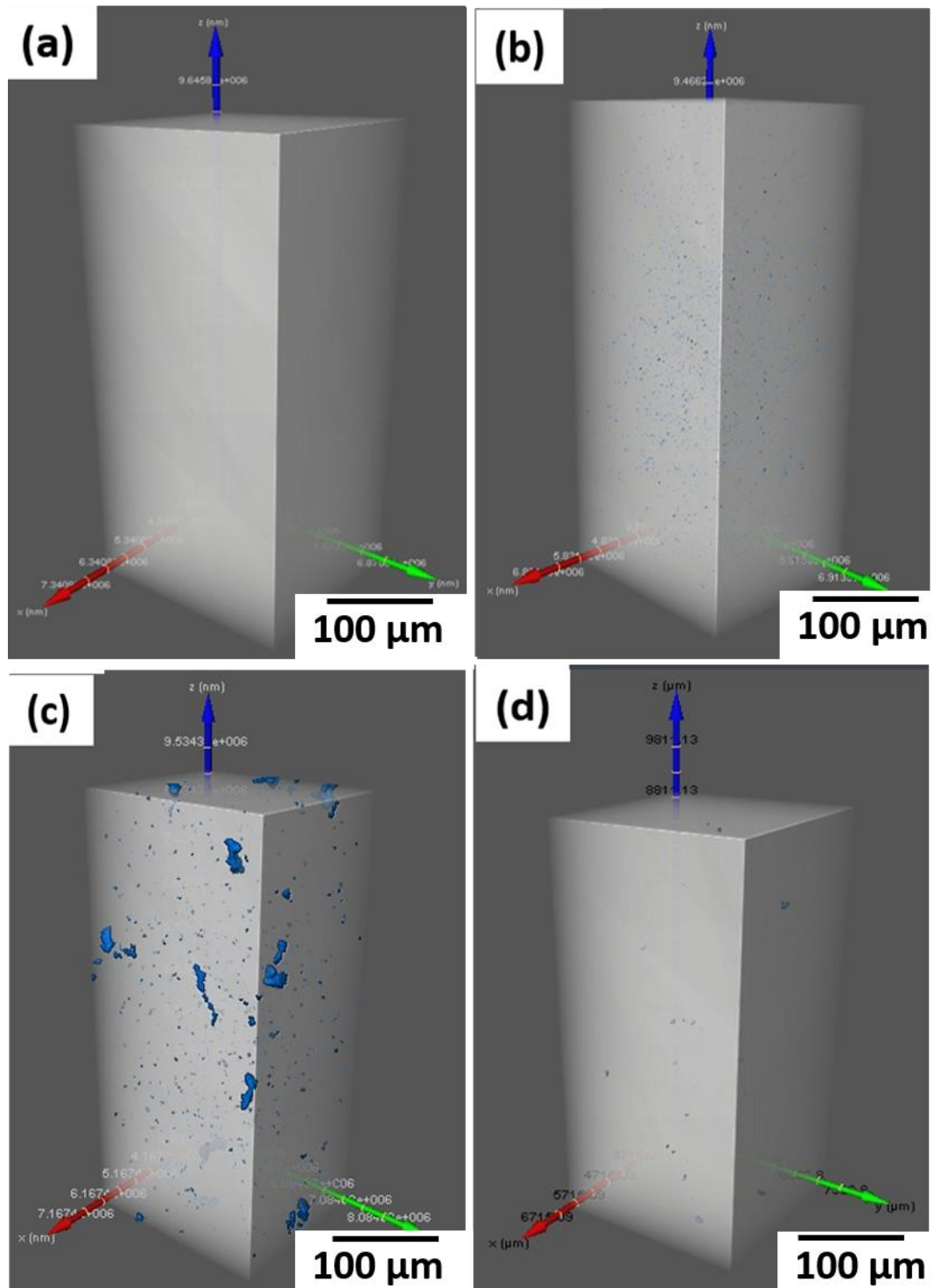


Figure 6.24 3D reconstructed CT images of vacuum cast Al-7Si alloy at (a) 700°C (b) 900°C and Al-7Si-2Fe alloy at (c) 700°C (d) 900°C

Figure 6.25 shows the 3D reconstructed X-ray CT images of the porosities of Al-7Si and Al-7Si-2Fe alloy cast in vacuum at melt temperatures of 700°C and 900°C.

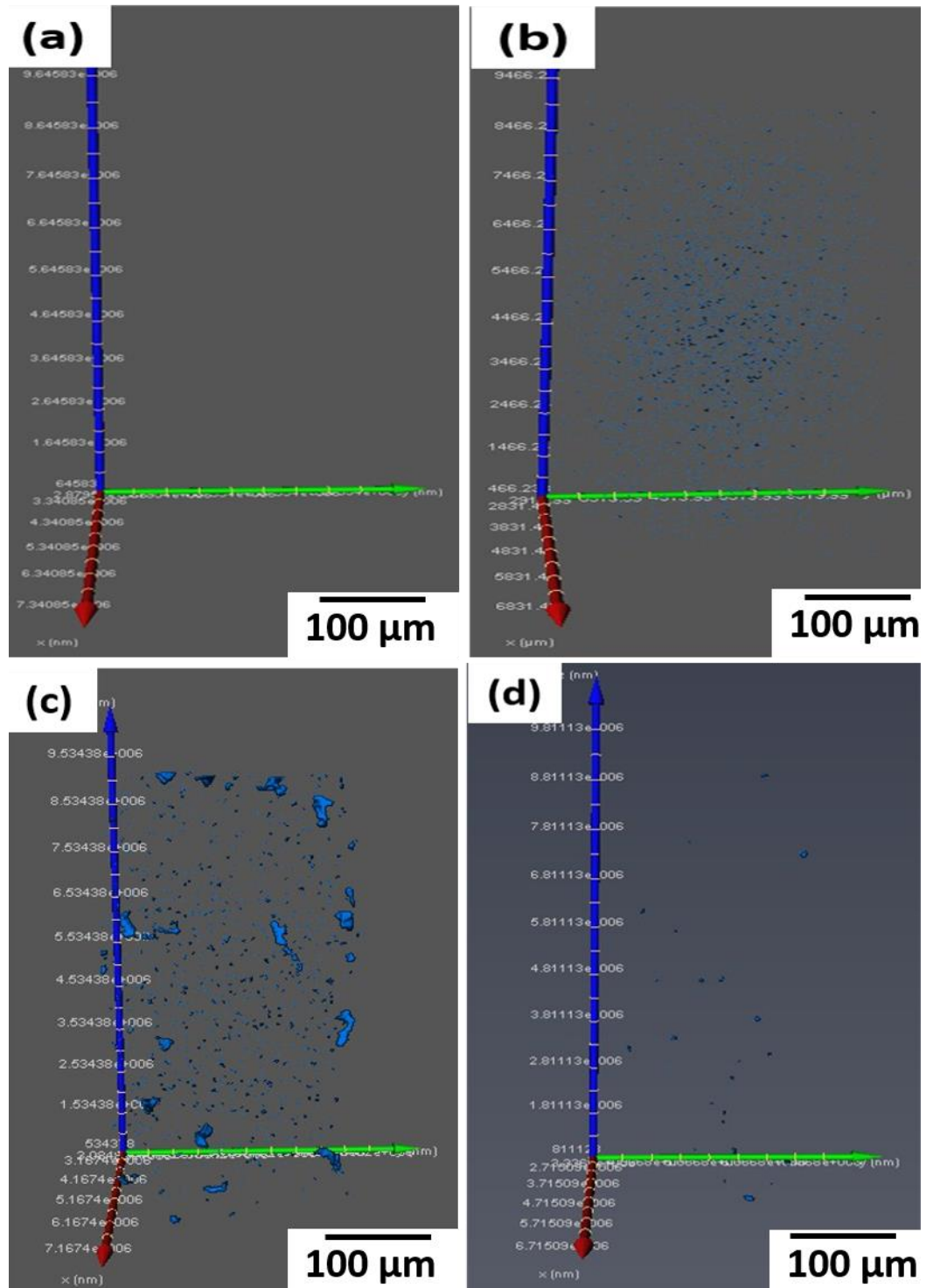


Figure 6.25 3D reconstructed CT images of porosities in Al-7Si alloy at cast in vacuum atmosphere at (a) 700°C (b) 900°C and Al-7Si-2Fe alloy at (c) 700°C (d) 900°C

Even in the vacuum conditions, there is some nano porosities left in the alloys (Figure 6.25 b). This could be due to the moisture left in the cast iron mould, or the noises formed on CT imaging or the processing errors. These pores can be neglected since it will not have any considerable effect in the mechanical properties. But the Al-7Si-2Fe alloy cast at 700°C shows large pores. This could be the casting defects formed due to the intermetallic particles. The bigger intermetallic platelets restricts the fluid flow during the solidification resulting in incomplete filling and formation of big pores.

Figure 6.26 shows the quantification of the pores formed in Al-7Si and Al-7Si-2Fe alloy cast under vacuum at melt temperatures of 700°C and 900°C respectively.

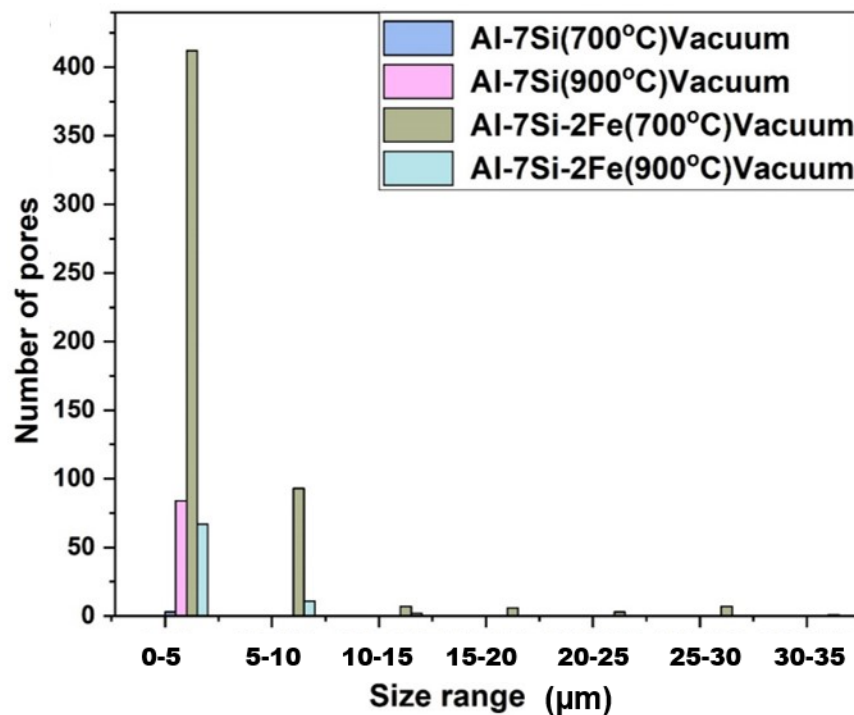


Figure 6.26 Pore size distribution of vacuum cast Al-Si and Al-Si-Fe alloys

The pores below the size range of 10 µm can be neglected as noises present in the imaging or processing. Considering the number of porosities above 15 µm size there is no reported porosities in Al-7Si-2Fe alloy at 900°C and there is more than 25 pores

for Al-7Si-2Fe alloy at 700°C. This represents the effect of intermetallic particles in the formation of pores.

6.3.2 Mechanical property analysis

The 3D tomography result shows that the intermetallic particle refinement and porosity formation on vacuum conditions is different compared to the open casting conditions. Therefore it necessary to evaluate the tensile properties in order to find the effect of vacuum conditions in defining the mechanical properties of the alloy. Figure 6.27 shows the tensile stress vs strain curves of Al-7Si alloys and Al-7Si-2Fe alloys cast at 700°C and 900°C in the vacuum conditions. The tensile curves of Al-7Si alloys shows the tensile stress for the alloy cast at 700°C is slightly better than that of 900°C. But the difference is less compared to the open casting. This may be due to the reduced porosity on vacuum casting compared to the open casting at 900°C. The tensile curves of Al-7Si-2Fe alloy shows that, the maximum tensile stress and strain is more for superheating at 900°C, compared to 700°C. This could be due to the particle refinement on 900°C and the casting defects associated with the intermetallic particles.

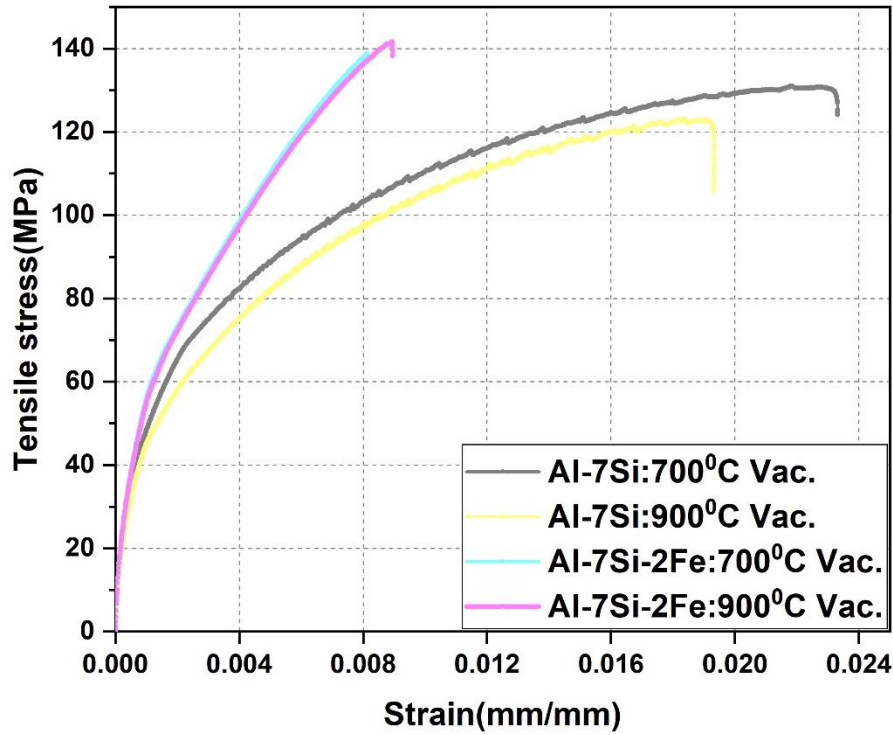


Figure 6.27 Tensile stress vs strain curve on tensile loading of vacuum cast Al-7Si and Al-7Si-2Fe alloys

The mechanical properties along with the pore size distribution analysis show that the alloy casted at 900°C in a vacuum atmosphere improved the quality of the cast compared to the 700°C. This shows that the increase in superheat temperature to 900°C, is an effective method for modification of recycled aluminium.

The experimental findings of this chapter provides an understanding of iron intermetallic formation on casting at different superheat temperatures and with different cooling rate. The increased cooling rate and higher superheat above 850°C, is found to refine the iron intermetallic particles. The increase in cooling rate controls the growth of iron intermetallic particles by reducing the total time available for the growth. Whereas in case of superheating, the high superheat temperature above 850°C results in transformation of γ -aluminium oxide to α -aluminium oxide resulting in reduced nucleation of primary iron intermetallic particles. Also the high superheat temperature increases the undercooling during solidification and thereby enhances nucleation of aluminium and intermetallic particles. In case of superheating below 850°C, the formation of γ -aluminium oxide is more, which act as a nucleating agent

for primary iron intermetallic formation. This overcomes the effects of undercooling resulting in enhanced growth of primary intermetallic particles. The intermetallic particle refinement is comparatively low in case of increased cooling rate. Even though the refinement in case of superheating is significant enough to improve the microstructure of the alloys, the mechanical properties are not improved due to increased porosity. The vacuum induction melting and casting is found to reduce the porosity and thereby improves the mechanical properties significantly. But considering the amount of aluminium recycled, vacuum induction melting and casting is incapable at an industrial level application.

Chapter 7. Chemical modification of iron intermetallic particles in aluminium alloys

This chapter discusses the main part of the project, the modification of iron intermetallic particles with addition of chemicals in to Al-Fe and Al-Si-Fe alloys. As explained detailed in the literature review section, there are many different approaches carried out in the past for the modification of the iron intermetallic particles. Among them one of the most efficient, industrially viable and cost effective way of modification is the chemical modification of the iron intermetallic particles. In this chapter the modification of iron intermetallic particles on addition of manganese, strontium and lanthanum is extensively studied.

7.1 Effect of manganese and strontium on iron intermetallic particles in Al alloy

Although few previous researches reported the modification of iron intermetallic particles in aluminium alloys on addition of manganese and strontium [20,47,51,94–96], a detailed investigation is required to analyse the effect of the modification.

7.1.1 Microstructure analysis

Figure 7.1 shows the microstructure of (a) Al-7Si-1Fe (b) Al-7Si-1Fe-0.5Mn (c) Al-7Si-1Fe-0.5Mn-400ppmSr alloys obtained from the SEM. Even with the addition of 0.5% of manganese to the Al-7Si-1Fe alloy the large β -phase intermetallic particles were shortened, but not modified in a significant amount (Figure 7.1b). The plate-like silicon particles (grey coloured) were not at all affected by the Mn addition. However, addition of Mn modified the morphology of few needle shaped β -phase compounds into sludge-like/Chinese script morphology. But the addition of Sr significantly changed the morphology of silicon particles from coarse plate-like to fine fibrous networks (Figure 7.1c). Similar observation were reported earlier [56,92,94,97].

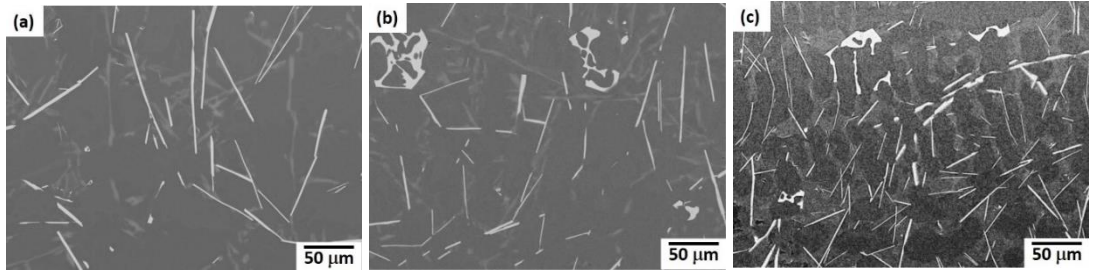


Figure 7.1 SEM images of (a) Al-7Si-1Fe (b) Al-7Si-1Fe-0.5Mn (c) Al-7Si-1Fe-0.5Mn-400ppmSr

Figure 7.2 shows the SEM microstructure of (a) Al-7Si-2Fe (b) Al-7Si-2Fe-1Mn (c) Al-7Si-2Fe-1Mn-400ppmSr alloys. For Al-7Si samples containing 2 wt% Fe content (Figure 7.2a), the iron intermetallic particles were more in number compared to the 1%Fe content. Most of these intermetallic particles were transformed into script-like morphology upon addition of 1% of Mn (Figure 7.2b). However, it also resulted in the formation of few bigger structures. This could be Al-Fe-Mn-Si structures as reported by few researches earlier[97]. Furthermore, the addition of Sr (Figure 7.2c) shows more prominent script morphologies, in comparison to those formed initially in the Al-7Si-2Fe-1Mn samples. This is because strontium breaks down large α - $\text{Al}_{15}(\text{FeMn})_3\text{Si}_2$ compounds into smaller α -phase compounds and AlSiMnSr compounds[95].

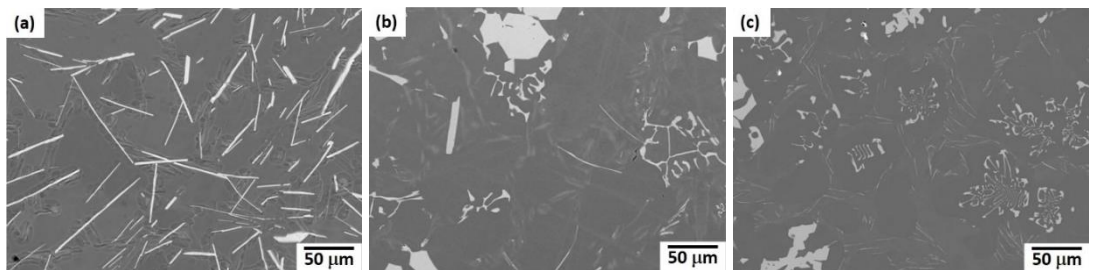


Figure 7.2 SEM images of (a) Al-7Si-2Fe (b) Al-7Si-2Fe-1Mn (c) Al-7Si-2Fe-1Mn-400ppmSr

This shows that the modification of the iron intermetallic particles mainly occurs due to the addition of manganese. This is because manganese reacts with the β -Al₅FeSi compounds resulting in the formation of α -phase iron intermetallic compounds with a script-like morphology (Figure 7.2b). However, manganese modification more than 0.5% formed very large intermetallic compounds of Al₁₅(FeMn)₃Si₂ (Figure 7.2b) which was also not desirable for better mechanical properties[69,70,94,96]. Therefore strontium was also added to further modify the morphology. Figure 7.2c shows that strontium decomposes the large intermetallic compounds of Al₁₅(FeMn)₃Si₂ compounds resulting in the formation of Al₈Si₂MnSr and Al_{8.5}Fe₃MnSi compounds. Strontium also modified other silicon particles in the Al-Si alloys. It changed their coarse needle-like morphology into a fine fibrous network of Al₂Si₂Sr particles[95,98].

Elemental mapping and point ID analysis were carried out to find the compositions of different particles present in the Al-7Si-2Fe-1Mn-400ppmSr microstructure (Figure 7.3).

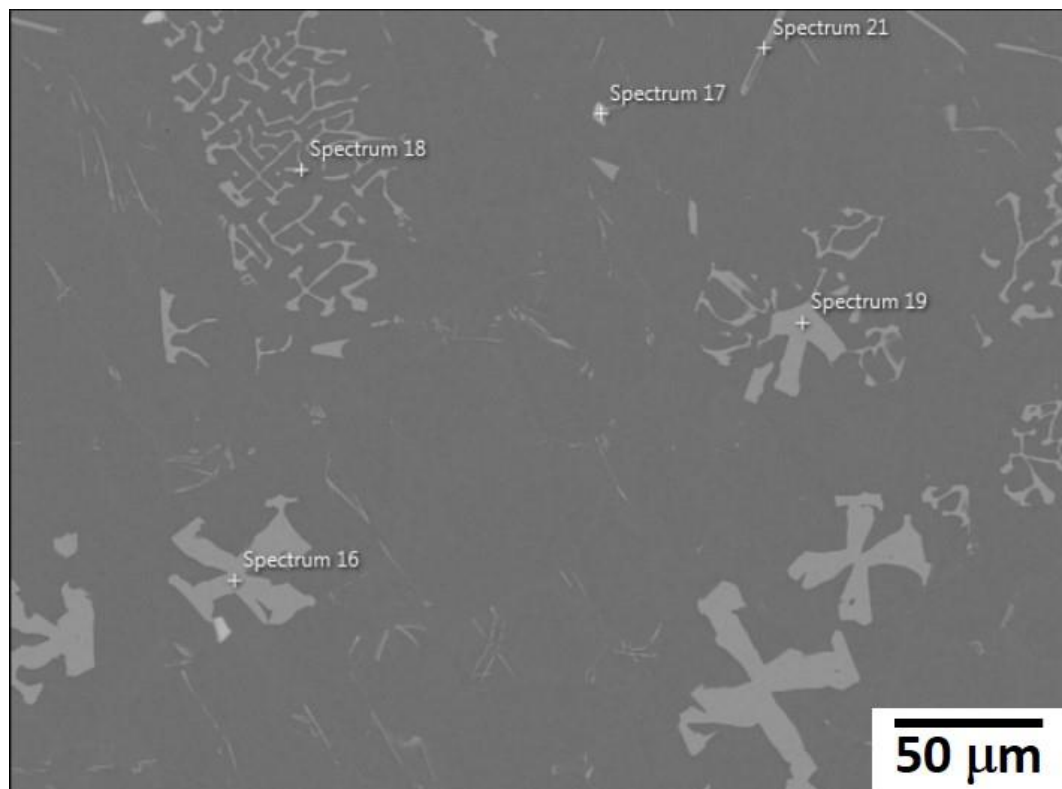


Figure 7.3 Intermetallic compounds identified through EDS analysis

The results for the spectrum analysis is depicted in table 7.1. The phase identification was carried out on the basis of mass fraction.

Table 7.1 Phase identification from spectrum data

Spectrum 16	$\text{Al}_{15}(\text{FeMn})_3\text{Si}_2$
Spectrum 17	$\text{Al}_8\text{Si}_2\text{MnSr}$
Spectrum 18	$\text{Al}_{8.5}\text{Fe}_3\text{MnSi}$
Spectrum 19	$\text{Al}_{15}(\text{FeMn})_3\text{Si}_2$
Spectrum 21	$\beta\text{-Al}_5\text{FeSi}$

In order to to understand the quantitative effect of modification, the quantified data analysis of the particle size and pore size have to be studied. An identical approach was undertaken to analyse the size of the intermetallic particles and porosity in Al-7Si alloy samples using the ImageJ software. The particle size was calculated using feret length (Maximum length of the particle in 2D image) and was plotted against the frequency (%) of particle as shown in Figure 7.4. As expected, Al-7Si-1Fe-0.5Mn had a larger proportion of particles below 10 μm than Al-7Si-1Fe (Figure 7.4a). About 89% of particles had a size less than 10 μm in Al-7Si-1Fe-0.5Mn where as only 57% of the particles in Al-7Si-1Fe had a size less than 10 μm . This showed that the modification effect of manganese which breaks down the needle-like β -phase compounds into script-like α -phase compounds with smaller size. Also, the increase in the percentage of smaller particles showed the formation of smaller particles due to breaking of bigger intermetallic compounds. Furthermore, the particles per unit area within the region of 0.4 μm -20 μm in the strontium modified alloy (Al-7Si-2Fe-1Mn-400ppmSr) is more than Al-7Si-2Fe-1Mn alloy (Figure 7.4b). This could be due to the rupture of large $\alpha\text{-Al}_{15}(\text{Fe,Mn})_3\text{Si}_2$ into smaller particles upon addition of strontium.

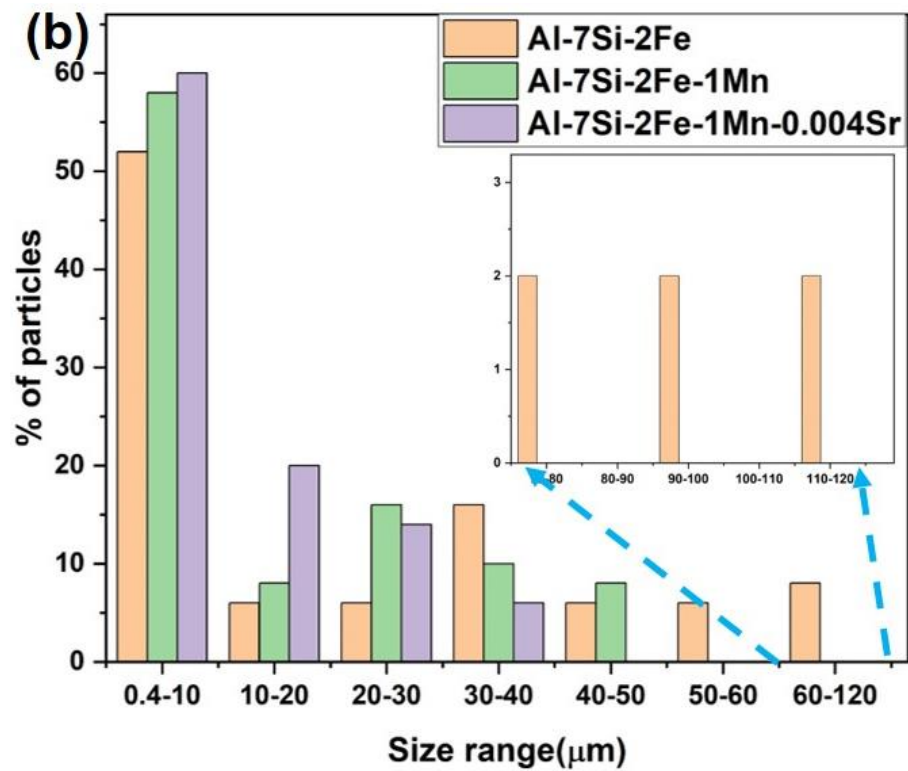
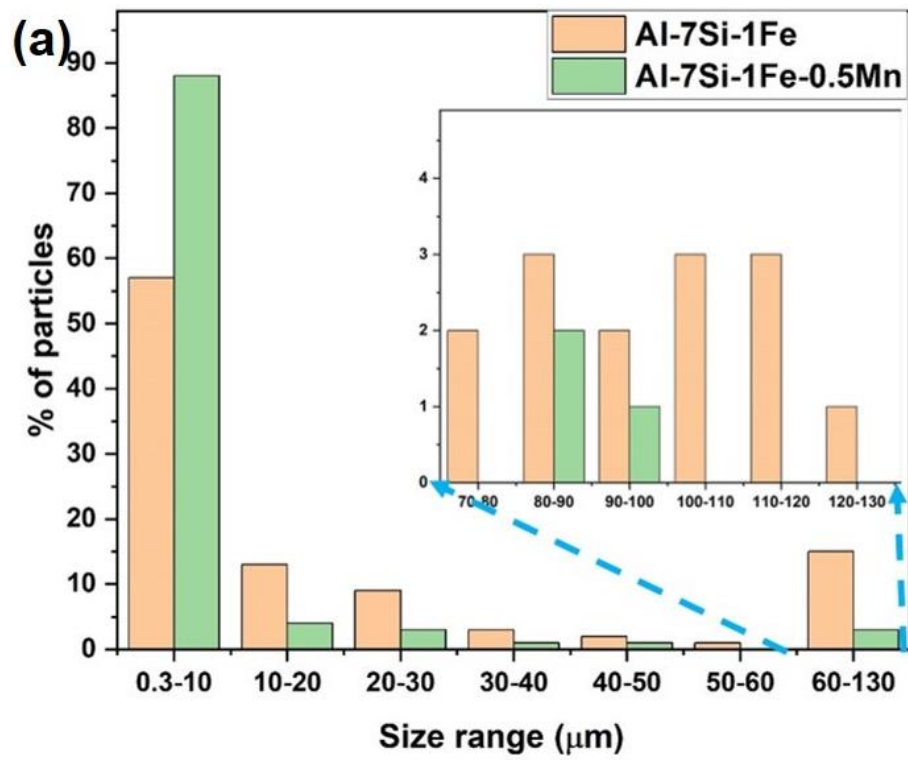


Figure 7.4 Plot showing frequency(%) vs average particle size of (a) Al-7Si-1Fe (b) Al-7Si-2Fe

The size of the largest particle observed in Al-7Si-2Fe was 115 μm , while 50 μm and 40 μm in Al-7Si-2Fe-1Mn and Al-7Si-2Fe-1Mn-400 ppm Sr samples respectively. However, some unmodified $\alpha\text{-Al}_{15}(\text{Fe}, \text{Mn})_3\text{Si}_2$ compounds still exist, but these large compounds accounted for less than 5% of the total sample area (projected area in Figure 7.4b).

The reduction in particle size showed that besides the morphology modification, addition of manganese and strontium resulted in the formation of smaller particles. It is also important to study the effect of modifying elements on the porosity of the cast alloys produced. Figure 7.5 shows the plot of average pore size to frequency of pores in Al-7Si alloy. The average pore size was analysed using ImageJ from the feret diameter calculations. Al-7Si-1Fe-0.5Mn and Al-7Si-2Fe-1Mn alloys had the largest pores whereas the Al-7Si-1Fe alloy had the smallest pores. This could be due to the morphology of the $\alpha\text{-Al}_{15}(\text{Fe}, \text{Mn})_3\text{Si}_2$ formed which restricted the flow of molten metal and thereby resulting in porosity. Although addition of strontium resulted in the reduction of average particle size in the alloy, it increased the porosity drastically. The pores in the Al-7Si-2Fe-1Mn-400ppmSr were comparatively much higher in size and more in number than the Al-7Si-2Fe-1Mn alloy. This is due to the higher oxygen affinity of strontium, resulting in the formation of strontium oxides during melting. The removal of these pores by degassing is not a possible task[99].

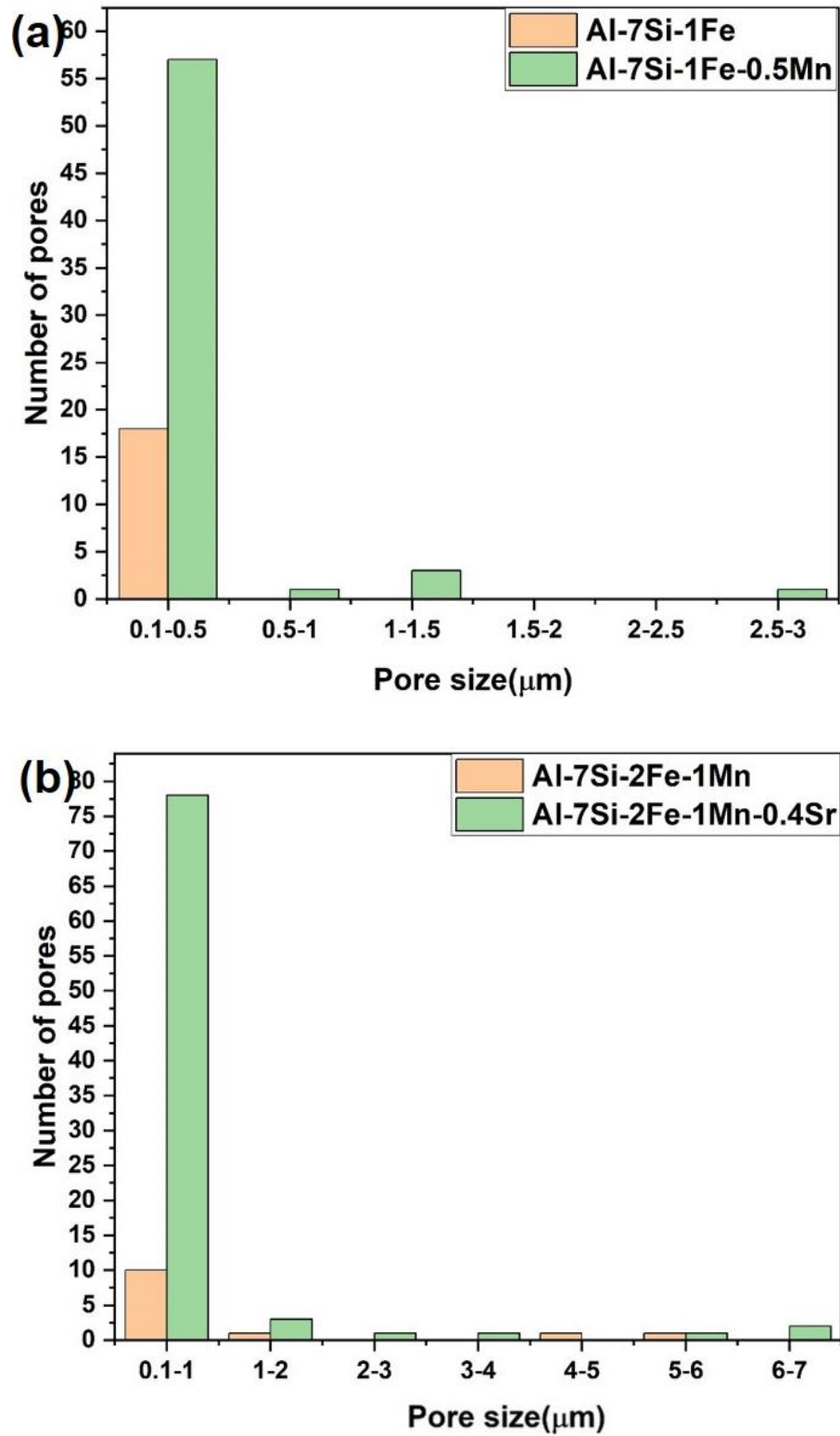


Figure 7.5 Plot showing number of pores vs average pore size of (a) Al-7Si-1Fe (b) Al-7Si-2Fe

Even though the modification of Al-Si-Fe alloys was found to be limited with the addition of Sr and Mn, their effect on Al-Fe alloys has to be studied to understand

the role of silicon in these alloys. Figure 7.6 and 7.7 shows the elemental mapping of Al, Fe and Mn, in Al-1Fe-0.5Mn alloy and Al-2Fe-1Mn alloys. The addition of Mn to the Al-2Fe-1Mn alloy resulted in the formation of AlFeMn particles, with a needle-like morphology. This shows that even in the absence of silicon, addition of Mn above 0.5% resulted in the formation of bigger intermetallic particles along with few AlFe intermetallic particles which resulted in the deterioration of mechanical properties.

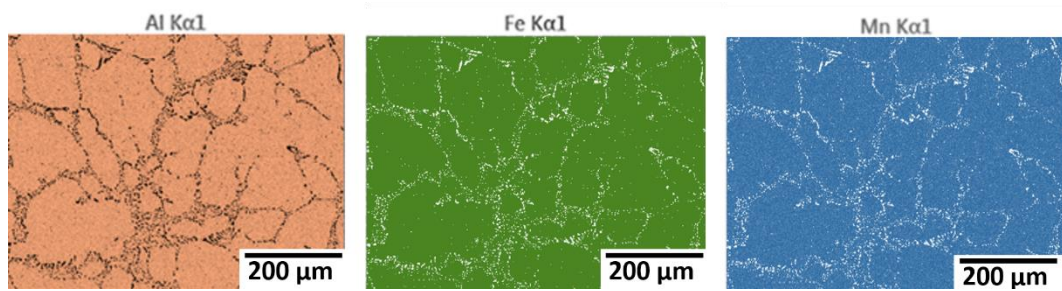


Figure 7.6 SEM-EDS elemental mapping of Al-1Fe-0.5Mn (orange colour represents distribution of Al, green colour represents distribution Fe, and blue colour represents distribution of Mn).

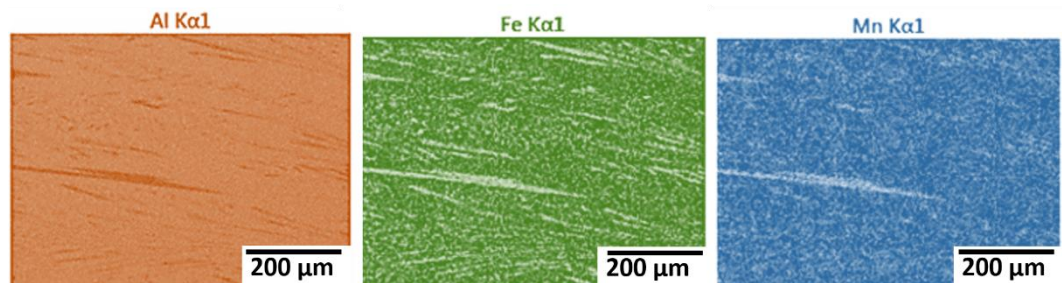


Figure 7.7 SEM-EDS elemental mapping of Al-2Fe-1Mn (orange colour represents distribution of Al, green colour represents distribution Fe, and blue colour represents distribution of Mn).

Figure 7.8 shows the elemental mapping of Al, Fe, Sr and Mn, in Al-2Fe-1Mn-400ppm Sr alloys.

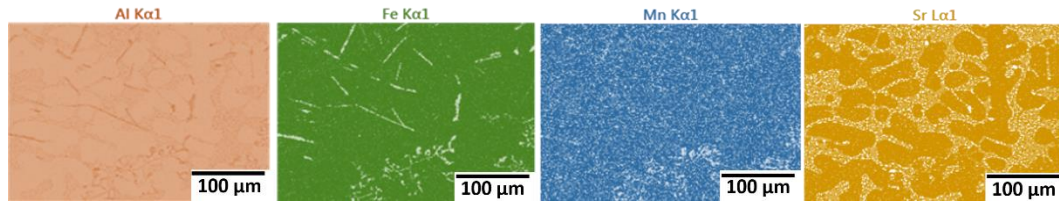


Figure 7.8 SEM-EDS elemental mapping of Al-2Fe-1Mn-400ppm Sr (orange colour represents distribution of Al, green colour represents distribution Fe, yellow colour represents Sr and blue colour represents distribution of Mn).

Figure 7.9 and 7.10 show the elemental mapping of Al, Fe, Si, Sr and Mn, in Al-7Si-1Fe-0.5Mn-400ppm Sr alloys and Al-7Si-2Fe-1Mn-400ppm Sr alloys.

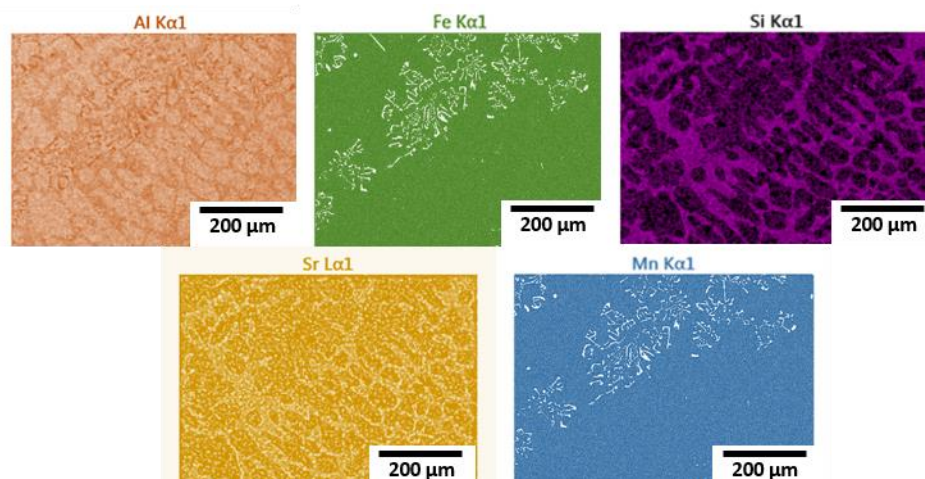


Figure 7.9 SEM-EDS elemental mapping of Al-7Si-1Fe-0.5Mn-400ppm Sr (orange colour represents distribution of Al, green colour represents distribution Fe, violet colour represents Si, yellow colour represents Sr and blue colour represents distribution of Mn).

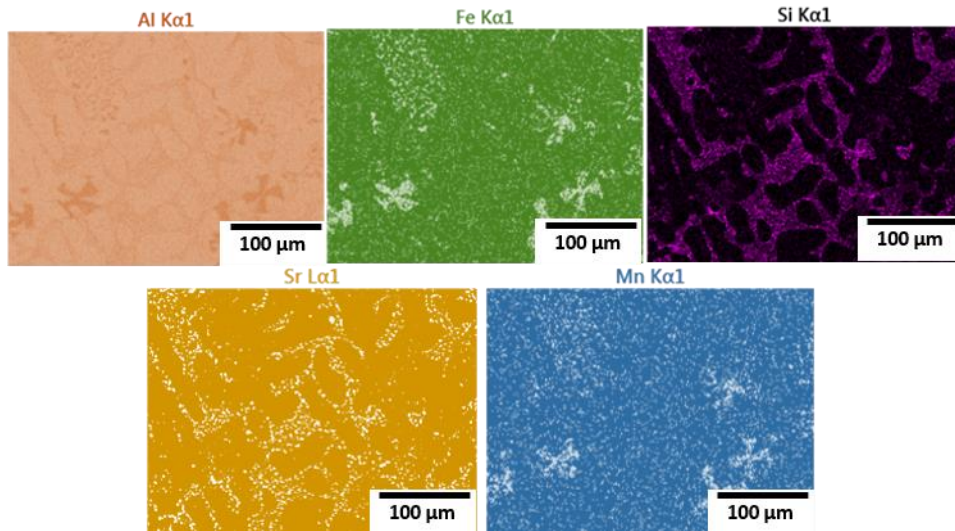


Figure 7.10 SEM-EDS elemental mapping of Al-7Si-2Fe-1Mn-400ppm Sr (orange colour represents Al, green colour represents Fe, violet colour represents Si, yellow colour represents Sr and the blue colour represents Mn).

The addition of Sr converted the manganese based intermetallic particles with platelet morphology to a Chinese script morphology, which improved the mechanical properties[69]. Even though all the AlFeMn iron intermetallic particles were modified, the AlFe intermetallic particles are not modified.

7.1.2 3-Dimensional FIB-SEM studies

Figure 7.11 shows the 3D reconstructed images of Al-7Si-2Fe-1Mn-400ppmSr alloy. The FIB-SEM scan was performed on a 50*20 micron area to observe the morphology of α -AlFeMnSi particle along with β -AlFeSi particle. Figure 10a shows the alloy with all the different particles in it. The particles were then selected individually for a better visualisation of their morphology. The third dimension of α -AlFeMnSi particles (Figure 7.11b) shows that these intermetallic particles grows as thick blocky morphology with sharp edges. The sharp edges of these blocks can act as stress raisers. Since these particles were bigger in size, this would increase the risk of failure.

The 3D reconstructed image β -AlFeSi particle (Figure 7.11c) was further separated out to analyse its morphology. The figure also shows that some of the β -AlFeSi particle still remain in the alloy with the platelet shape morphology.

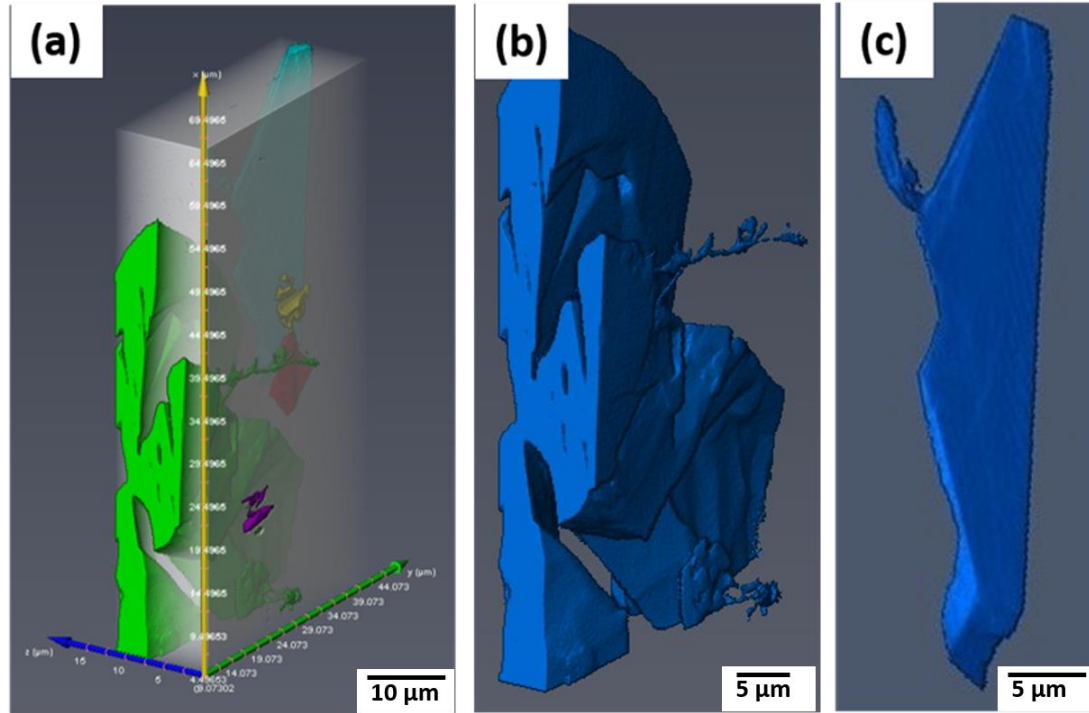


Figure 7.11 3D reconstructed image of (a) Al-7Si-2Fe-1Mn-400ppmSr alloy (b) α phase iron intermetallic distribution in Al-7Si-2Fe-1Mn-400 ppm Sr alloy (c) α phase iron intermetallic particles.

7.2 Effect of Lanthanum addition on iron intermetallic particles in Al alloy

As observed in the previous section, the modification of iron intermetallic particles in Al-Fe and Al-Si-Fe alloys were not significant with the additions of Mn and Sr. Hence they cannot be considered as an effective chemical modifier in any of the Al-Fe or Al-Si-Fe alloys with higher contents (2%) at normal casting conditions. Though there are some contradictions, the modification of iron intermetallic particles on addition of lanthanum, a rare earth element, has been reported[74]. In this section,

a detailed investigation of the effect of lanthanum addition in aluminium and aluminium alloys is studied.

7.2.1 Microstructure Analysis of Al-Fe-La alloys

Figure 7.12 shows the SEM images of Al-0.6Fe, Al-2Fe and Al-2Fe-1La alloys. The Al-2Fe results show the formation of large number of intermetallic particles in aluminium. The intermetallic particles are found to spread throughout the microstructure before the addition of lanthanum (Figure 7.12b). Figure 7.12c shows that lanthanum addition resulted in a refining of intermetallic particles. Most of the intermetallic particles were found to be at grain boundaries of the alloy matrix and the needle shape of the intermetallic particles were found to be modified. Also, it was found that the addition of lanthanum resulted in grain refinement.

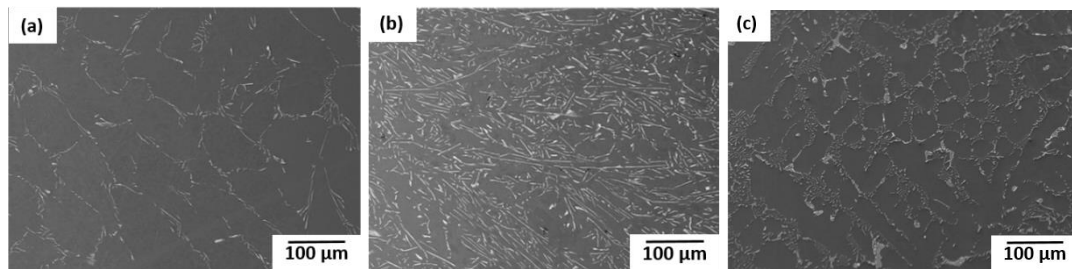


Figure 7.12 SEM-EDS images of (a) Al-0.6Fe, (b) Al-2Fe, (c) Al-2Fe-1La

Figure 7.13 shows the elemental composition of the Al-2Fe alloy in the respective images through EDS analysis. As shown in Figure 7.14, after the addition of lanthanum, iron intermetallic particles shows a different morphology compared to needle shaped morphology of iron intermetallic particles in Al-2Fe alloy. Figure 7.15 shows the elemental composition through EDS analysis at a higher magnification. Interestingly lanthanum is found to be segregated along the iron intermetallic particles which prevents the further growth or branching of these intermetallic particles.

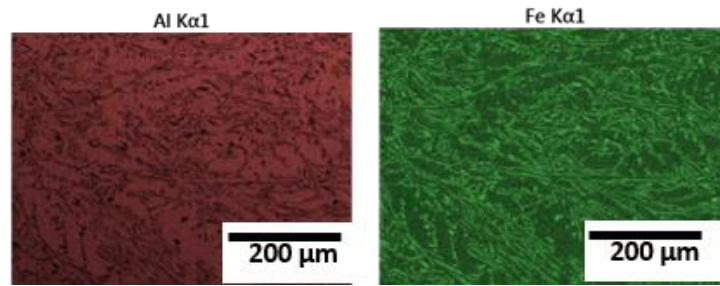


Figure 7.13 SEM-EDS elemental mapping of Al-2Fe (Red colour represents Al and green colour represents the Fe).

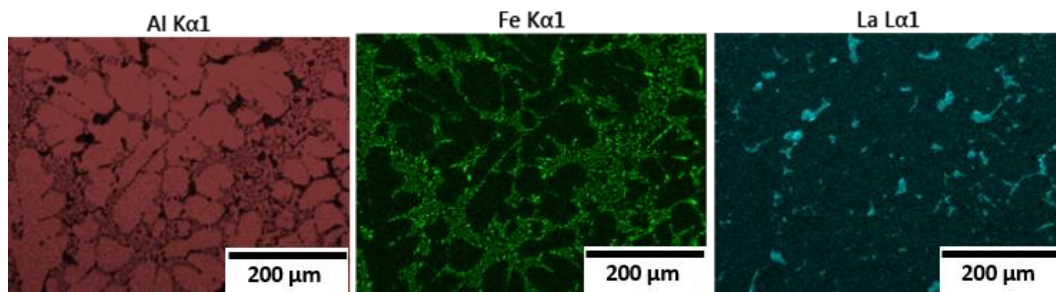


Figure 7.14 SEM-EDS elemental mapping of Al-2Fe-1La (Red colour represents Al, blue colour represents La and green colour represents Fe).

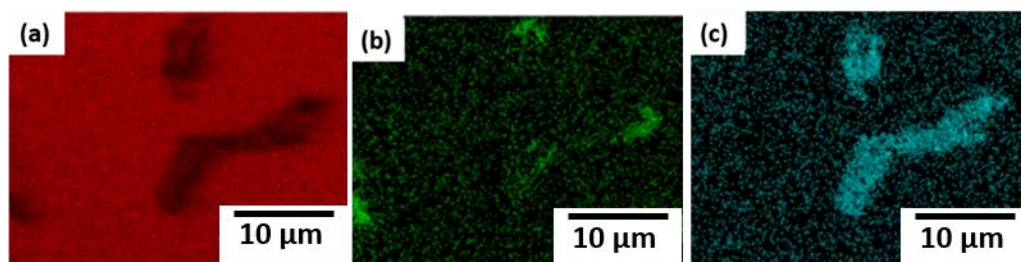


Figure 7.15 SEM-EDS elemental mapping of Al-2Fe-1La at higher magnification (a) aluminium, (b) iron, (c) lanthanum.

Figure 7.16 a and Figure 7.16 b shows the bright field images of Al-2Fe alloy and Al-2Fe-1La alloy respectively. The selected area diffraction (SAD) patterns were captured from the marked locations in these images to study the structure of the intermetallic particle phases. Figure 7.16 c shows the TEM-EDS elemental mapping of Al-2Fe-1La alloy. The EDS image was captured from the area marked in the Figure 7.16 b. Lanthanum structures and needle shaped intermetallic structures were observed distinctly under the TEM. This high magnified TEM image was used to find the mass fraction of each of the elements in the respective structures. The yellow coloured area represents the primary aluminium area. The orange colour represents the Al-Fe intermetallic particles, identified as Al_5Fe_2 and the blue colour represents the Al-La structures, identified as $\text{Al}_{11}\text{La}_3$ according to the elemental mass fraction calculation. However, only TEM diffraction patterns allow reliable phase identification. Figure 7.16 d and Figure 7.16 e, f show the selective area diffraction pattern from the particles in Al-2Fe alloy and Al-2Fe-1La alloy respectively. The diffraction pattern from the needle shaped particles in Al-2Fe alloy (Figure 7.16a) indicates that these large intermetallic platelets are $\theta\text{-Al}_{13}\text{Fe}_4$ phases (Figure 7.16d). Whereas the diffraction pattern from the Al-2Fe-1La (Figure 7.16b) alloy indicates that the needle shaped particles are $\eta\text{-Al}_5\text{Fe}_2$ phase (Figure 7.16e) and the particles with Chinese script morphology are $\text{Al}_{11}\text{La}_3$ particles (Figure 7.16f). The formation of $\eta\text{-Al}_5\text{Fe}_2$ intermetallic phases in Al-Fe-La system is explained later.

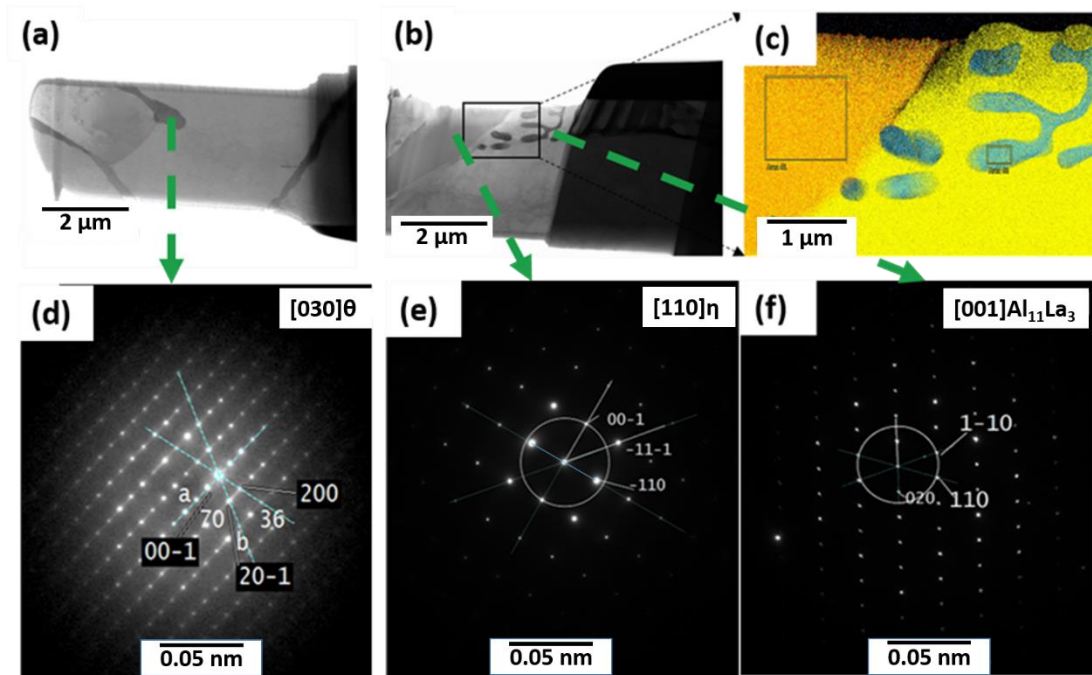


Figure 7.16 TEM bright field images of (a) Al-2Fe alloy (b) Al-2Fe-1La alloy, (c) TEM-EDS image from Al-2Fe-1La alloy (rectangular area in Figure b), TEM SAD of (d) $\text{Al}_{13}\text{Fe}_4$ in Al-2Fe alloy (Marked location in Figure a), (e) Al_5Fe_2 in Al-2Fe-1La alloy (Marked location in Figure b) and (f) $\text{Al}_{11}\text{La}_3$ in Al-2Fe-1La alloy (Marked location in Figure b).

7.2.2 3-dimensional FIB-SEM studies of Al-Fe-La alloy

Figure 7.17 shows the 3D reconstructed image of Al-2Fe and Al-2Fe-1La alloys. Yellow colour represents the $\text{Al}_{11}\text{La}_3$, red colour represents the $\text{Al}_{13}\text{Fe}_4$ iron intermetallic particles and white colour represents the aluminium matrix. In the 3D image of Al-2Fe (Figure 7.17a), $\text{Al}_{13}\text{Fe}_4$ iron intermetallic particles are found to have a platelet type morphology in third dimension. The needle type morphology which appears in the 2-dimension is found to have a third dimension and it's actually a thin platelet with very sharp edges. The $\text{Al}_{11}\text{La}_3$ particles are found to be formed on surface of the Al_5Fe_2 iron intermetallic particles (Figure 7.17b). Figure 7.17c shows the iron intermetallic particle distribution using 3D reconstructed images from FIB-SEM. Eventhough the particles are big and sharp edged in Al-2Fe (Figure 7.1c), the particles found in Al-2Fe-La are more fragmented and round edged compared to Al-2Fe (Figure 7.17d). This is due to the anisotropic growth of Al_5Fe_2 phase, which resulted in branching out and change in direction of growth of the Al_5Fe_2 iron intermetallic

particles. This resulted in the formation of rounded edges (Figure 7.17d) instead of sharp edges (Figure 7.17c).

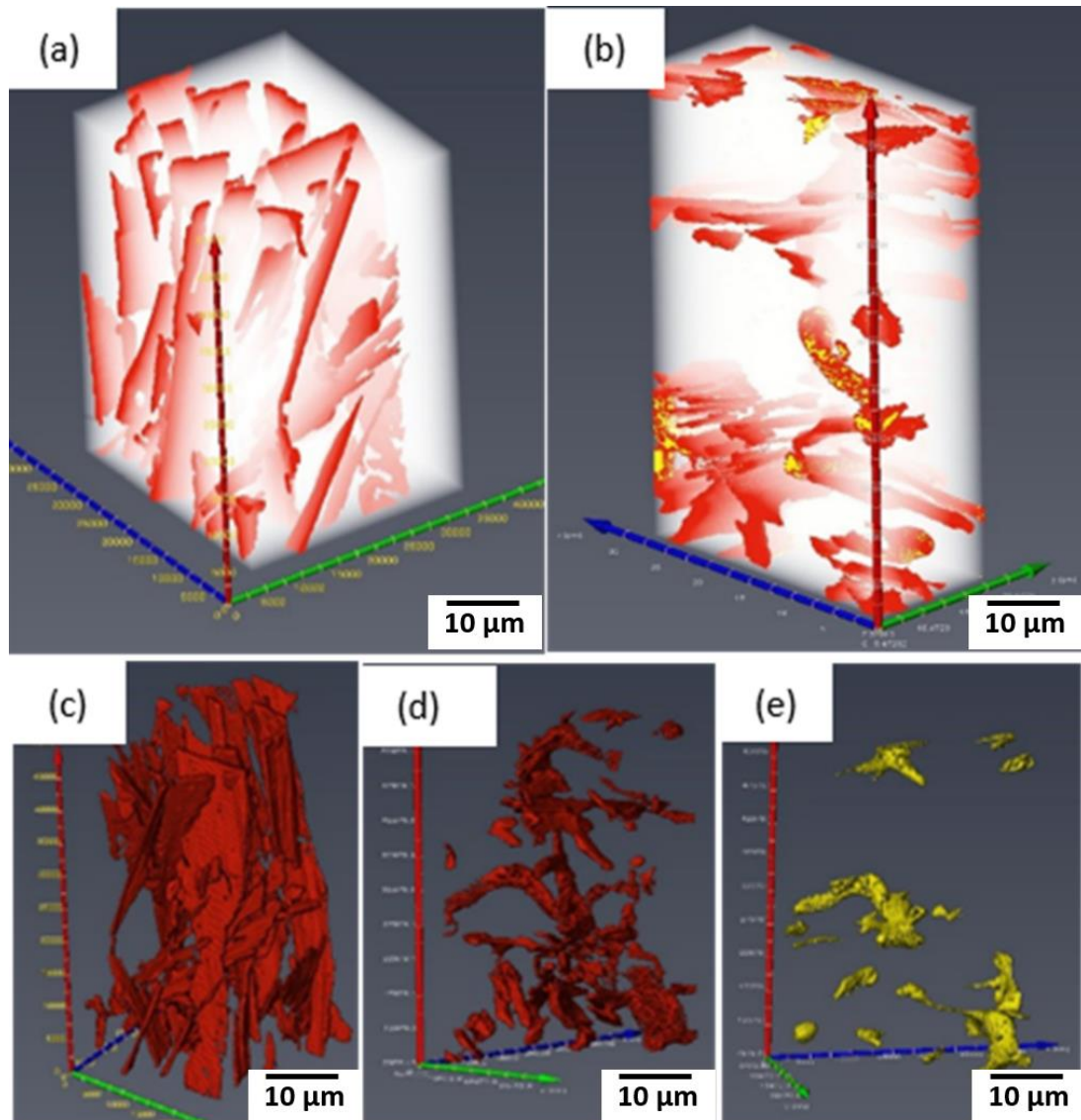


Figure 7.17 3D reconstructed image of (a) Al-2Fe, (b) Al-2Fe-1La (c) iron intermetallic distribution in Al-2Fe, (d) iron intermetallic distribution in Al-2Fe-1La (e) $Al_{11}La_3$ particles distribution in Al-2Fe-1La

Most of the particles were found to be interconnected or branched which restricted the quantitative analysis of the particles using the 3D images. Figure 7.17e shows the 3D reconstructed image of the $Al_{11}La_3$ particle. It is clear from Figure 7.17 that, after the addition of lanthanum the interconnections of the iron intermetallic particles

were broken down due to the formation of $\text{Al}_{11}\text{La}_3$ particle. However, the $\text{Al}_{11}\text{La}_3$ particles in Al-2Fe-1La were formed on the surface of the iron intermetallic particles thereby restricting the growth.

The fundamental mechanism behind the morphological modification and phase formation is still not fully understood. The mechanism can be explained based on the observed results and literature available. The aluminium rich side of Al-Fe and Al-La phase diagram is shown in figure 7.18. The major metastable phases reported in near eutectic Al-Fe alloys are Al_6Fe phase and Al_5Fe_2 phase[23,100–103]. The major metastable phase reported in Al rich side of Al-La phase diagram is $\beta\text{-Al}_{11}\text{La}_3$ which forms at higher temperatures and transforms into $\alpha\text{-Al}_{11}\text{La}_3$ particles. There are significant differences in the eutectic nucleation between Al-2Fe alloys with and without lanthanum addition based on the phase diagrams and previous literatures available. The sequence of intermetallic phase formation cannot be determined by the thermodynamics alone, the diffusion kinetics of the system has also to be considered[104].

Eventhough the modification of $\text{Al}_3\text{Fe}/\text{Al}_{13}\text{Fe}_4$ intermetallics on addition of rare earth elements was reported recently by few researchers[105,106], their experimental findings are ambiguous. Liang et al.[106] studied the effect of Er addition in Al-2Fe alloy and found that, the Er addition refines Al_3Fe intermetallic particles. They reported an enrichment of Er atoms at the solid/liquid interface which prevents the growth of Al_3Fe phase which on final stages of solidification forms $\text{Al}_{10}\text{Fe}_2\text{Er}$. The major limitaion of this study is lack of high magnified TEM images for locating the segregation on the interface and lack of TEM diffraction patterns from the iron intemetallic surface. The reported $\text{Al}_{10}\text{Fe}_2\text{Er}$ phase is having similar diffraction pattern compared to Al_5Fe_2 phase and this could be a misinterpretation. Luo et al. [105] studied the microstructure refinement of Al-5Fe alloys by addition of Ce-rich rare earth mixture and found that Al-Ce-La compounds precipiated near the Al_3Fe intermetallics are restricting their growth. The major limitaion of this finding is the lack of TEM observations and microscopy from which we could effectively understand the phases formed on the addition of rare earths. But one common observation in both the studies is increased nucleation of aluminium due to increased freezing range/depressed eutectic temperature on addition of rare earth elements.

One possible reason for the modification effect of lanthanum addition which can be explained based on the phase diagram of Al-Fe and Al-La diagrams is lowering the eutectic temperature. The eutectic temperature of Al-Fe phase diagram is 654°C. Since the formation of $\text{Al}_{11}\text{La}_3$ phase starts only at 634°C, instead of eutectic nucleation, Al continues to nucleate. It's clear from the phase diagrams, the solubility of La in aluminium is lower compared to Fe. La acts as nucleation sites for aluminium. The further nucleation of aluminium results in the enrichment of Fe and La in the interface of the aluminium and $\text{Al}_{13}\text{Fe}_4$ phases. La segregates on the Al side and Fe segregates near the $\text{Al}_{13}\text{Fe}_4$ side. La in the liquid nucleates on the aluminium side of the interface and forms $\text{Al}_{11}\text{La}_3$ in the final stages of solidification impedes the formation of metallic bond with iron and aluminium and thereby inhibit Al-Fe formation[103]. Due to this, the $\text{Fe}_4\text{Al}_{13}$ and Fe phases will react with each other and then transform to Fe_2Al_5 . Similar observations of phase transformation from $\text{Al}_{13}\text{Fe}_4$ to Al_5Fe_2 phases were reported in rapidly solidified Al-Fe alloys[102,104].

The growth of Fe-Al phase in presence of lanthanum is explained as below. Since the atom saturation in Al_5Fe_2 phase is high and the concentration of vacant sites in the C-axis direction of Al_5Fe_2 phase is high, aluminium atoms can easily diffuse to form a new compound layer and grow quickly in that direction[107]. In this case, since the Al_5Fe_2 phase was formed on the surface of $\text{Al}_{11}\text{La}_3$ phase the aluminium atoms were diffused into $\text{Al}_{11}\text{La}_3$ phase resulting in a lower Al: Fe ratio near to the Al_5Fe_2 phase. Since the Al_5Fe_2 requires a Al: Fe ratio of 2.5: 1 and the $\text{Al}_{13}\text{Fe}_4$ requires a Al: Fe ratio of 3.25: 1, at lower Al: Fe ratio the formation and growth of Al_5Fe_2 phase is prevailed than the reaction leading to the formation of $\text{Al}_{13}\text{Fe}_4$ phase [108–110]. Due to this the growth of Al_5Fe_2 intermetallic continues, preventing the formation of $\text{Al}_{13}\text{Fe}_4$ phase and resulting in anisotropic growth of Al_5Fe_2 phase with the tongue-like morphology as reported in the literature [111,112].

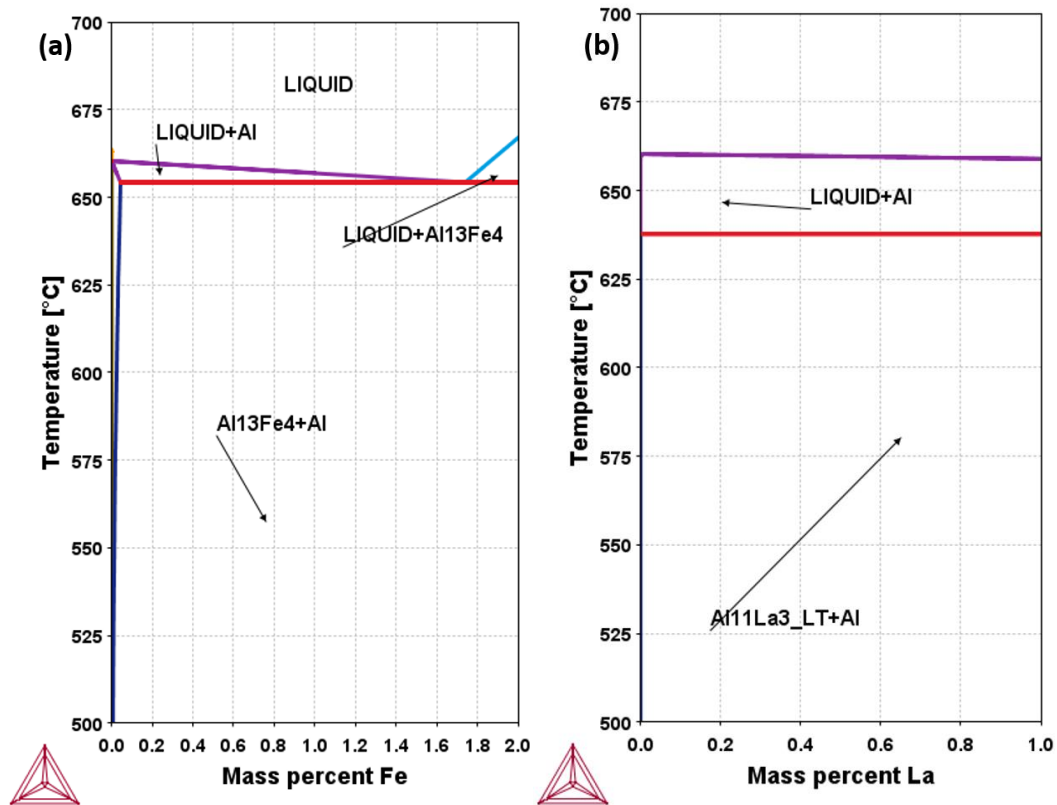


Figure 7.18 ThermoCalc computed binary phase diagrams of a) the aluminium-rich side in the Al-Fe system, (b) the aluminium-rich side in the Al-La system.

7.2.3 Mechanical properties of Al-Fe-La

Figure 7.19 shows the tensile stress vs strain curve of Al-0.6Fe alloy (red colour), Al-2Fe (blue colour) and Al-2Fe-1La (green colour) alloys. The tensile stress for Al-2Fe-1La alloy is 104.39 MPa, for Al-2Fe alloy is 95.41 MPa and for Al-0.6Fe alloy is 76.55 MPa. This shows a 9.41 % increase on addition of lanthanum.

The Al-0.6Fe alloy can bear a maximum load of 2164.65 N, Al-2Fe-1La alloy can bear a maximum load of 2761.84 N whereas Al-2Fe alloy can bear 2697.86 N. This shows that the maximum tensile load carrying capacity is increased by 9.41 % on addition of lanthanum. However, the maximum elongation after lanthanum addition is reported to increase by 51.35%. The maximum elongation for Al-0.6Fe alloy is 10.59 mm, for Al-2Fe alloy is 7.83 mm and maximum elongation for Al-2Fe-1La alloy is 11.79 mm.

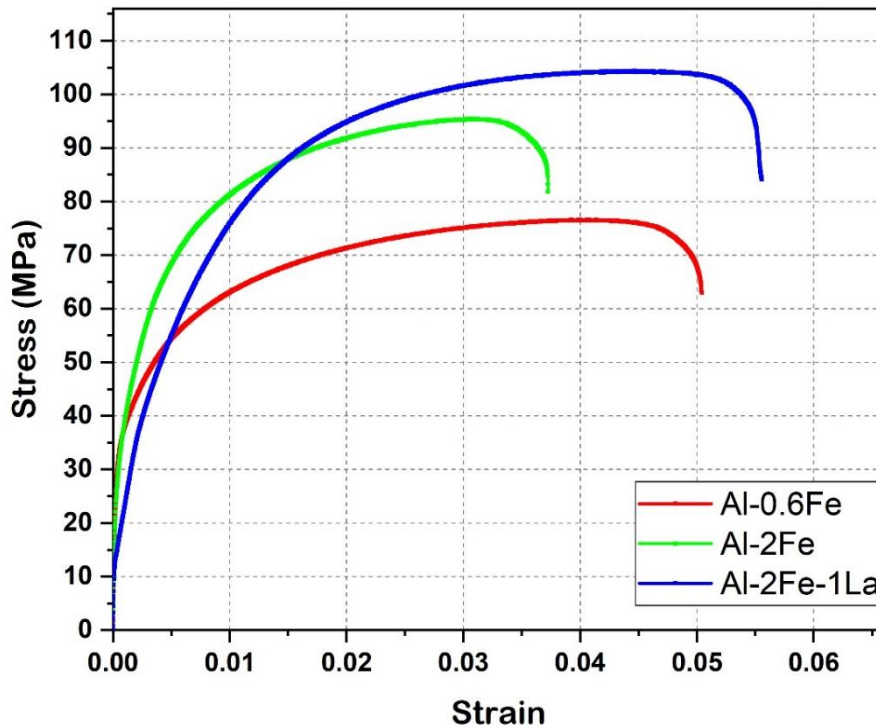


Figure 7.19 Tensile properties of Al-0.6Fe, Al-2Fe and Al-2Fe-1La alloys, Tensile stress vs strain.

Figure 7.20 shows the fracture surface in the tensile samples of Al-2Fe and Al-2Fe-1La alloys. The dimpled appearance of both surfaces indicates the ductile failure mode of the alloys[113]. The dimples are not completely formed in Al-2Fe alloy (Figure 7.20a) whereas the dimples are clearly formed in Al-2Fe-1La alloy (Figure 7.20b). The pits observed in the Al-2Fe (Figure 7.20a) surfaces could be due to the $\text{Al}_{13}\text{Fe}_4$ intermetallic particle pullout along the interfacial boundary between intermetallic particles and the aluminium matrix or the rupture of brittle $\text{Al}_{13}\text{Fe}_4$ intermetallic particles. This observation suggests that the early failure of the Al-2Fe alloy is particularly resulted by the $\text{Al}_{13}\text{Fe}_4$ intermetallic particles.

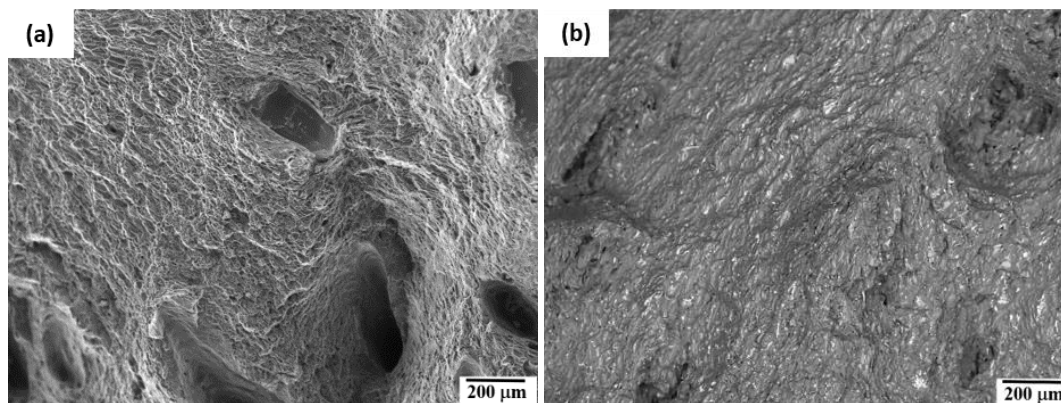


Figure 7.20 Fracture surface in the tensile samples of Al-2Fe and Al-2Fe-1La alloys cast at 740°C.

The study using the 3D FIB-SEM technique clearly showed that the addition of 1 wt% lanthanum to Al-2Fe impedes the growth of $\text{Al}_{13}\text{Fe}_4$ intermetallic particles by changing the morphology and helps in improving the mechanical properties of Al-2Fe alloy. The 3D visualisation from FIB-SEM and quantified information from TEM images were helpful not only in finding out the morphology of $\text{Al}_{13}\text{Fe}_4$ and Al_5Fe_2 intermetallic particles and $\text{Al}_{11}\text{La}_3$ particles, but also useful in finding out the reason behind the morphology change of intermetallic particles. The mechanical property analysis shows the improvement of mechanical properties on addition of 1% lanthanum. It is therefore interesting to study the effect of lanthanum in Al-Si-Fe alloys where all the contradictory results were reported.

Figure 7.21 shows the elemental mapping of Al, Si and Fe in Al-7Si-0.6Fe-1La alloy and Figure 7.22 shows the elemental mapping of Al, Si and Fe in Al-7Si-2Fe-1La alloy. It is evident from the Figure 7.21 and Figure 7.22, the addition of 1% lanthanum cannot modify the iron intermetallic particles in Al-7Si alloy. But the silicon flakes are found to be refined. This shows that the lanthanum added modifies silicon flakes instead of $\beta\text{-Al}_5\text{FeSi}$.

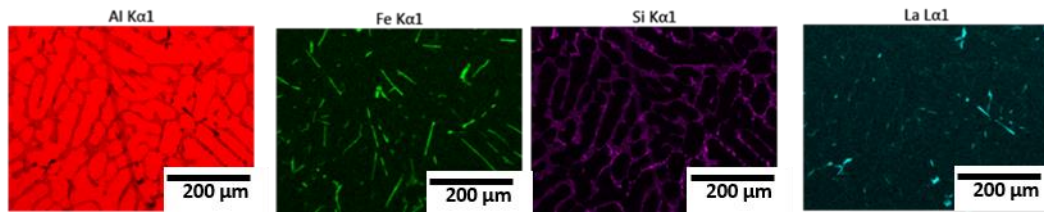


Figure 7.21 SEM-EDS elemental mapping of Al-7Si-0.6Fe-1La (red colour represents Al, green colour represents Fe, violet colour represents Si, and blue colour represents La).

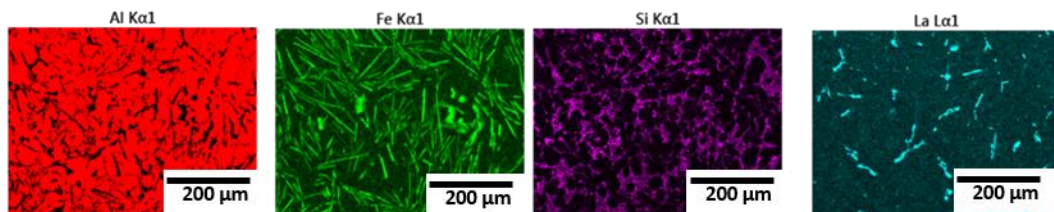
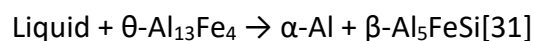


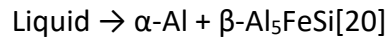
Figure 7.22 SEM-EDS elemental mapping of Al-7Si-2Fe-1La (red colour represents Al, green colour represents Fe, violet colour represents Si, and blue colour represents La).

This result showed that the lanthanum added reacted with aluminium and silicon to form $\text{La}(\text{AlSi})_2$ as reported in the literature[75–77]. The sequence of formation of harmful iron intermetallic particles in Al-Si alloys is different depending on the silicon concentration. The phase diagram shown in Figure 4.1 shows the evidence, which is the primary reason for a number of different reactions reported in the literature[30–33,111,114]. Since in case of low silicon alloys the morphology (platelet shape) and structure (monoclinic) of the $\text{Al}_{13}\text{Fe}_4$ phase and later formed $\beta\text{-AlFeSi}$ phase is similar, the formation of $\text{Al}_{13}\text{Fe}_4$ phase during solidification was left unnoticed[31]. The reason for the contradictory results in modification of iron intermetallic particles can be explained with this.

In case of low silicon Al-Si alloys, the formation of iron intermetallic particles are in the order



Whereas in high silicon Al-Si alloys, the formation of iron intermetallic particles are in the order



In case of low silicon alloy (0.5 wt% Fe and 0.8 wt% Si) reporting the lanthanum modification in the literature[74,75], the lanthanum forms $\text{Al}_{11}\text{La}_3$ phase which restricts the formation of $\text{Al}_{13}\text{Fe}_4$ phase and helps in the formation of Al_5Fe_2 phase which is not identified. The silicon available in the liquid then diffuses in to the $\text{Al}_{11}\text{La}_3$ phase forming $\text{La}(\text{Al Si})_2$, which is reported in the literature. The Fe needed for the formation of $\alpha\text{-Al}_8\text{Fe}_2\text{Si}$ phase or $\beta\text{-Al}_5\text{FeSi}$ phase is generated from the dissolution of the primary phase Al_5Fe_2 , and the Si needed is diffused from the liquid. Here, the ratio of silicon needed for the formation of $\alpha\text{-Al}_8\text{Fe}_2\text{Si}$ phase: $\beta\text{-Al}_5\text{FeSi}$ phase is 1:2. Since the silicon available in the liquid state is very low in the low silicon alloys especially after reacting with the lanthanum, the formation of $\alpha\text{-Al}_8\text{Fe}_2\text{Si}$ phase is prevailed and $\beta\text{-Al}_5\text{FeSi}$ phase is prevented. Hence the addition of lanthanum can modify the iron intermetallic particles in low silicon Al-Si alloys. However in the contradictory researches[76,77] and in this project the Al-Si alloy contains a higher silicon content (Al-12.6Si/Al-7Si). For higher silicon content, all the lanthanum added will be consumed for the formation of $\text{La}(\text{Al Si})_2$ phase, by diffusion of Si into the $\text{Al}_{11}\text{La}_3$ phase. In these alloys the $\beta\text{-Al}_5\text{FeSi}$ phase forms directly from the liquid and not by the quasi-peritectic reaction from the liquid and $\theta\text{-Al}_{13}\text{Fe}_4$ phases [115]. Hence lanthanum addition cannot modify the iron intermetallic particles in high silicon Al-Si alloys, but can refine the remaining silicon platelets.

Figure 7.23 shows the tensile stress vs strain curve for Al-7Si-0.6Fe-1La (green colour) alloy and Al-7Si-2Fe-1La (cyan colour) alloy.

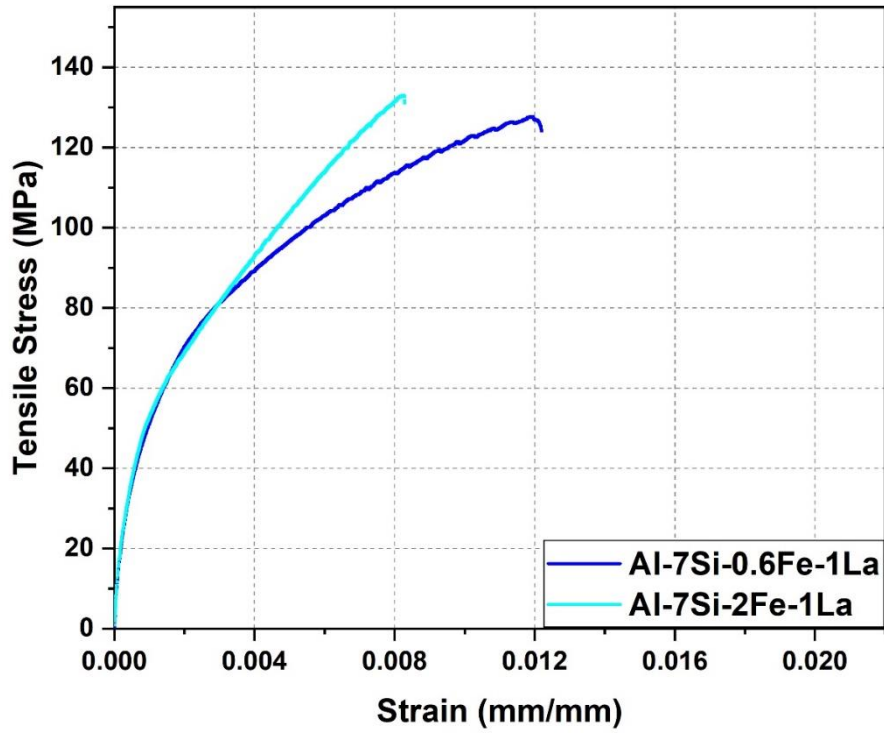


Figure 7.23 Tensile stress vs Strain curve of Al-7Si-La alloys

The tensile stress for Al-7Si-0.6Fe-1La alloy is 129.65 MPa and for Al-7Si-2Fe-1La alloy is 134.51 MPa. The Al-7Si-0.6Fe-1La alloy can bare a maximum load of 3609.15 N and Al-7Si-2Fe-1La alloy can bare a maximum load of 3790.81 N. This shows that after the addition of lanthanum the tensile stress of Al-7Si-Fe alloy is significantly increased. However, the maximum elongation for Al-7Si-0.6Fe-1La alloy is 2.58 mm, and for Al-7Si-2Fe-1La alloy is 1.76 mm. This also shows a significant increase after the addition of lanthanum. Eventhough the microstructure show not much refinement of iron intermetallics, the silicon refinement on addition of lanthanum could be the reason behind the improvement of mechanical properties. Even in the Al-7Si –2Fe alloy, the silicon is found to be refined which can contribute to the improvement of mechanical properties. This is also higher than the mechanical properties reported for melt superheated and fast cooled Al-7Si-2Fe alloys.

The addition of lanthanum is found to improve the microstructure and mechanical properties in Al-Fe alloys and Al-Si-Fe alloys. This work explains the mechanism behind the modification and quantified the improvement in mechanical properties.

Chapter 8. Conclusion and suggestions for future work

8.1 Conclusions

Modification of iron intermetallic particles by the addition of chemical additives and understanding the modification mechanisms are essential to improve the recyclability of aluminium alloys. In this project, advanced characterisation techniques are used to understand the morphology, size distribution and crystallography of various intermetallic particles formed due to the addition of chemical modifying elements such as Mn, Sr, and La. 3D imaging and other characterisation techniques such as TEM, SEM-EDS, and mechanical testing presents both qualitative and quantitative analysis of iron intermetallic particle formation, its effects on mechanical properties, modification of iron intermetallic particles with the mechanisms involved. This thesis highlights the use of chemical addition for the modification of iron intermetallic particles.

This research exposed that the major reason for the detrimental properties of the iron intermetallic particles is its platelet shaped morphology which acts as stress raisers during the tensile loading (chapter 5). This research also spotted that with the addition of 1% of lanthanum into the Al-2Fe alloy, the platelet shaped $\text{Al}_{13}\text{Fe}_4$ intermetallic particles can be prevented by stabilising the tongue shaped Al_5Fe_2 intermetallic particles (chapter 7). This finding is particularly helpful in the modification of iron intermetallic particles in low silicon Al-Si alloys where the peritectic reaction of $\text{Al}_{13}\text{Fe}_4$ phase and liquid forms the detrimental Al_5FeSi particles. Also this finding could explain the previous contradictions related to the modification effect of lanthanum.

The experimental study on Al-7Si alloy with different cooling rate and superheat (chapter 6) identified the improvement in the microstructure by refining the intermetallic particles and influence of $\beta\text{-Al}_5\text{FeSi}$ intermetallic particles on restricting the molten metal flow and porosity formation. These understandings of β -intermetallic particle formation and their relation with the solidification defects are

critical to the improvement of recycling processes. The quantified data of particle size and pore size will be helpful in the validation of predictive models related to this.

8.1.1 Major findings

The major findings from the present study in this project can be summarised as;

- Increase in iron content and silicon content results in a significant increase in size, thickness and volume fraction of iron intermetallic particles in the alloy.
- 3D XCT studies of the tensile test samples show that the fracture has occurred in a region of high intermetallic particle concentration. The extensive analysis of the fracture surface along with the XCT reconstructed image of the fracture area shows that the fracture has occurred not mainly through the brittle intermetallic particles but by the de-bonding of sharp edged particle and matrix at the interface.
- Higher the iron content in Al-7%Si alloy, higher the number of intermetallic particles, bigger the platelet boundaries, and higher the tendency for crack propagation and earlier the failure of the alloy. Increasing the iron content in the Al-7Si alloy from 0.6 % to 2 % (Al-7Si-2Fe alloy) results in a reduction in % elongation and tensile strength by ~58% and 25% respectively.
- As the cooling rate increases, the size of intermetallic particles decreases and the mechanical property increases. Al-7Si-2Fe alloy cast at 700°C, 800°C and 900°C shows that the size of the intermetallic particle reduces and the mechanical property increases with the optimum superheating of the alloy.
- The β -Al₅FeSi intermetallic compounds reduce the castability of Al-7Si alloys by increasing porosity and reducing fluidity. Their plate-like structure (observed in 3D) act as barriers to the flow of liquid metal and escape of gases during solidification.
- Addition of strontium along with manganese modifies Al-7Si-2Fe alloys by altering the β -Al₅FeSi particles, and transforming their morphology into more pronounced sludge-like/Chinese script morphology. But at higher iron

contents, large bulky $\alpha\text{-Al}_{15}(\text{Fe}, \text{Mn})_3\text{Si}_2$ particles are formed on addition of M which are deleterious to the mechanical properties.

- A detailed investigation of the Al-2Fe-1La and Al-2Fe alloys using 3D FIB-SEM shows the morphology and distribution of $\text{Al}_{13}\text{Fe}_4$ and Al_5Fe_2 intermetallic particles and $\text{Al}_{11}\text{La}_3$ particles. The $\text{Al}_{13}\text{Fe}_4$ intermetallic particles in Al-2Fe alloy is found to have a sharp edged long platelet shape morphology where as the Al_5Fe_2 intermetallic particles in Al-2Fe-1La alloy is found to be branched and have a rounded edge morphology. The $\text{Al}_{11}\text{La}_3$ particles are formed around the Al_5Fe_2 intermetallic particles preventing its growth in one direction and rounding the edges. The sharp edges generally act as stress raisers thereby debonding the particle and matrix at the interface resulting in failure of the alloy.
- Tensile test result shows the destructive effect of iron intermetallic particles on the mechanical properties in Al-2Fe alloy. The Al-2Fe-1La alloy is found to have an increase of ~51% elongation, correspondingly enhancing the strength of the alloy by 9.41%. However, increasing iron content from 0.6 % to 2 % (Al-2Fe alloy) resulted in a reduction in elongation by ~26.08% while increasing the strength by 24.63%.

8.2 Suggestions for future work

The knowledge generated from this thesis about the chemical modification of iron intermetallic particles by the addition of lanthanum, manganese and strontium is useful for the further studies in this area. The study on mechanism of failure caused by iron intermetallic particles, effect of various silicon and iron content in the formation and growth of iron intermetallic particles is a good understanding for future research works related to recycling of aluminium. Most importantly, based on the current work, further research work on lanthanum modification on iron intermetallic particles can be continued which is not very extensively studied. Based on the mechanism explained on this thesis, lanthanum can modify iron intermetallic particles in Al-Fe alloys and low silicon Al-Fe-Si alloys and cannot modify Al-Fe-Si intermetallic particles in high silicon Al-Si-Fe alloys. It will be interesting to study low

silicon alloys, especially the wrought alloys of aluminium with the addition of addition for the modification of iron intermetallic particles. Also, it will be exciting to find the addition of lanthanum along with other silicon modifiers. Moreover, these understandings of β -intermetallic particle formation and their relation with the solidification defects are inputs to the improvement of thermodynamic modelling of aluminium and aluminium silicon alloy based systems. The quantified data of particle size and pore size will be helpful in the validation of predictive models related to this.

One of the major challenging factor in the modification of iron intermetallic particles by the addition of lanthanum is the availability and cost of lanthanum. Lanthanum ingot is 4-6 times expensive than pure aluminium[116,117]. But the modification requires only very small quantities of lanthanum (1%) which makes it economically profitable compared to other processes such as melt treatments or diluting the recycled aluminium by adding pure aluminium. The scope of this research work includes further studies in this area with more extensive studies to use lanthanum in alternative forms (lanthanum oxide, misch metal) which are more cost effective and available. Actually, lanthanum is one among the least expensive rare earth elements and is abundantly available in the form of bastnaesite and monazite[118,119]. But it could not be extracted with 100% efficiency[118] which makes it scarce and hence expensive. However, the benefits of lanthanum addition shouldn't be discussed only by considering the economic benefits. The mechanical property analysis in this research work showed that the lanthanum addition improved the strength and elongation in the aluminium alloys with higher iron content compared to the aluminium alloys with low iron content. This may be due to the refinement of primary aluminium or morphological changes to the iron intermetallic particles. Thus, the addition of lanthanum not only reduces the deteriorating effects of iron in recycled aluminium but also converts the iron intermetallic particles into a beneficial constituent. Recently, there have been few studies reported with Al-Si-Fe-La alloys used as positive electrode current collectors in Lithium ion batteries[120] and Al-Ni-Fe-La alloys used as amorphous alloys[121]. Therefore the future research of this alloy also includes understanding material properties such as electrical conductivity, corrosion potential and thermal stability, which could explore maximum utilisation of these alloys.

References

- [1] J. Mathew, A. Mandal, S.D. Kumar, S. Bajpai, M. Chakraborty, G.D. West, P. Srirangam, Effect of semi-solid forging on microstructure and mechanical properties of in-situ cast Al-Cu-TiB₂ composites, *J. Alloys Compd.* 712 (2017) 460–467. <https://doi.org/10.1016/j.jallcom.2017.04.113>.
- [2] M. Javidani, D. Larouche, Application of cast Al-Si alloys in internal combustion engine components, *Int. Mater. Rev.* 59 (2014) 132–158. <https://doi.org/10.1179/1743280413Y.0000000027>.
- [3] J. Mathew, P. Srirangam, The effect of manganese and strontium on iron intermetallics in recycled al-7% si alloy, *Miner. Met. Mater. Ser.* (2019) 235–240. https://doi.org/10.1007/978-3-030-05864-7_31.
- [4] C.B. Basak, N. Hari Babu, Morphological changes and segregation of β -Al₉Fe₂Si₂ phase: A perspective from better recyclability of cast Al-Si alloys, *Mater. Des.* 108 (2016) 277–288. <https://doi.org/10.1016/j.matdes.2016.06.096>.
- [5] J. Mathew, G. Remy, M.A. Williams, F. Tang, P. Srirangam, Effect of Fe Intermetallics on Microstructure and Properties of Al-7Si Alloys, *JOM.* (2019). <https://doi.org/10.1007/s11837-019-03444-5>.
- [6] G. Gaustad, E. Olivetti, R. Kirchain, Improving aluminum recycling: A survey of sorting and impurity removal technologies, *Resour. Conserv. Recycl.* 58 (2012) 79–87. <https://doi.org/10.1016/j.resconrec.2011.10.010>.
- [7] S.J. Maggs, Intermetallic phase selection in dilute Al-Fe-Si alloys, 1996. http://etheses.whiterose.ac.uk/4711/1/uk_bl_ethos_394317.pdf.
- [8] K. Zhang, X. Bian, Y. Li, Y. Liu, C. Yang, New evidence for the formation and growth mechanism of the intermetallic phase formed at the Al/Fe interface, *J. Mater. Res.* 28 (2013) 3279–3287. <https://doi.org/10.1557/jmr.2013.345>.

- [9] X. Li, A. Scherf, M. Heilmaier, F. Stein, The Al-Rich Part of the Fe-Al Phase Diagram, *J. Phase Equilibria Diffus.* 37 (2016) 162–173.

<https://doi.org/10.1007/s11669-015-0446-7>.
- [10] R.P. Elliott, F.A. Shunk, The Al-La (Aluminum-Lanthanum) system, *Bull. Alloy Phase Diagrams.* 2 (1981) 219–221. <https://doi.org/10.1007/BF02881485>.
- [11] S.W. Kim, U.H. Im, H.C. Cha, S.H. Kim, J.E. Jang, K.Y. Kim, Removal of primary iron rich phase from aluminum-silicon melt by centrifugal separation, *China Foundry.* 10 (2013) 112–117.
- [12] P. Liu, T. Thorvaldsson, G.L. Dunlop, Formation of intermetallic compounds during solidification of dilute Al–Fe–Si alloys, *Mater. Sci. Technol. (United Kingdom).* 2 (1986) 1009–1018. <https://doi.org/10.1179/mst.1986.2.10.1009>.
- [13] W. Khalifa, F.H. Samuel, J.E. Gruzleski, Iron intermetallic phases in the Al corner of the Al-Si-Fe system, *Metall. Mater. Trans. A Phys. Metall. Mater. Sci.* 34 (2003) 807–825. <https://doi.org/10.1007/s11661-003-1009-9>.
- [14] L.F. Mondolfo, *Aluminum alloys: structure and properties*, Elsevier, 2013.
- [15] S.G. Shabestari, The effect of iron and manganese on the formation of intermetallic compounds in aluminum-silicon alloys, *Mater. Sci. Eng. A.* 383 (2004) 289–298. <https://doi.org/10.1016/j.msea.2004.06.022>.
- [16] L.A. Narayanan, F.H. Samuel, J.E. Gruzleski, Crystallization behavior of iron-containing intermetallic compounds in 319 aluminum alloy, *Metall. Mater. Trans. A.* 25 (1994) 1761–1773. <https://doi.org/10.1007/BF02668540>.
- [17] M. Cooper, The crystal structure of the ternary alloy $\alpha(\text{AlFeSi})$, *Acta Crystallogr.* 23 (1967) 1106–1107. <https://doi.org/10.1107/s0365110x67004372>.
- [18] C.Y.. L.F.M. Sun, A clarification of phases occurring in aluminium-rich aluminium-iron-silicon alloys, *J. Inst. Met.* 95 (1967) 384.
- [19] V.G. Rivlin, G. V. Raynor, 4: Critical evaluation of constitution of aluminium-iron-silicon system, *Int. Met. Rev.* 26 (1981) 133–151.

<https://doi.org/10.1179/imtr.1981.26.1.133>.

- [20] L. Lu, A.K. Dahle, Iron-rich intermetallic phases and their role in casting defect formation in hypoeutectic Al-Si alloys, *Metall. Mater. Trans. A Phys. Metall. Mater. Sci.* 36 (2005) 819–835. <https://doi.org/10.1007/s11661-005-1012-4>.
- [21] M. V. Kral, P.N.H. Nakashima, D.R.G. Mitchell, Electron microscope studies of Al-Fe-Si intermetallics in an Al-11 Pct Si alloy, *Metall. Mater. Trans. A Phys. Metall. Mater. Sci.* 37 (2006) 1987–1997. <https://doi.org/10.1007/s11661-006-0141-8>.
- [22] Y.B. Zhang, S. Kateryna, T.J. Li, Effect of ultrasonic treatment on formation of iron-containing intermetallic compounds in Al-Si alloys, *China Foundry*. 13 (2016) 307–312. <https://doi.org/10.1007/s41230-016-5066-2>.
- [23] P.R. Goulart, V.B. Lazarine, C. V Leal, Intermetallics Investigation of intermetallics in hypoeutectic Al – Fe alloys by dissolution of the Al matrix, *Intermetallics*. 17 (2009) 753–761.

<https://doi.org/10.1016/j.intermet.2009.03.003>.
- [24] J.A. Taylor, Iron-Containing Intermetallic Phases in Al-Si Based Casting Alloys, *Procedia Mater. Sci.* 1 (2012) 19–33.

<https://doi.org/10.1016/j.mspro.2012.06.004>.
- [25] C.M. Dinnis, J.A. Taylor, A.K. Dahle, As-cast morphology of iron-intermetallics in Al-Si foundry alloys, *Scr. Mater.* 53 (2005) 955–958.

<https://doi.org/10.1016/j.scriptamat.2005.06.028>.
- [26] C. Puncreobutr, A.B. Phillion, J.L. Fife, P.D. Lee, Coupling in situ synchrotron X-ray tomographic microscopy and numerical simulation to quantify the influence of intermetallic formation on permeability in aluminium–silicon–copper alloys, *Acta Mater.* 64 (2014) 316–325. <https://doi.org/10.1016/j.actamat.2013.10.044>.
- [27] S. Terzi, J.A. Taylor, Y.H. Cho, L. Salvo, M. Suéry, E. Boller, A.K. Dahle, In situ

study of nucleation and growth of the irregular α -Al/ β -Al₅FeSi eutectic by 3-D synchrotron X-ray microtomography, *Acta Mater.* 58 (2010) 5370–5380. <https://doi.org/10.1016/j.actamat.2010.06.012>.

- [28] L.A. Narayanan, F.H. Samuel, J.E. Gruzleski, Crystallization behavior of iron-containing intermetallic compounds in 319 aluminum alloy, *Metall. Mater. Trans. A*. 25 (1994) 1761–1773. <https://doi.org/10.1007/BF02668540>.
- [29] A.M. Samuel, F.H. Samuel, H.W. Doty, Observations on the formation of β -Al₅FeSi phase in 319 type Al-Si alloys, *J. Mater. Sci.* 31 (1996) 5529–5539. <https://doi.org/10.1007/BF01159327>.
- [30] C.M. Allen, K.A.Q. O'Reilly, B. Cantor, Effect of semisolid microstructure on solidified phase content in 1xxx Al alloys, *Acta Mater.* 49 (2001) 1549–1563. [https://doi.org/10.1016/S1359-6454\(01\)00056-8](https://doi.org/10.1016/S1359-6454(01)00056-8).
- [31] G. Sha, K.A.Q. O'Reilly, B. Cantor, J.M. Titchmarsh, R.G. Hamerton, Quasi-peritectic solidification reactions in 6xxx series wrought Al alloys, *Acta Mater.* 51 (2003) 1883–1897. [https://doi.org/10.1016/S1359-6454\(02\)00595-5](https://doi.org/10.1016/S1359-6454(02)00595-5).
- [32] T.J. Backerud L, Chai G, Solidification characteristics of aluminum alloys, Vol. 2, American Foundrymen's Society, 1990.

<https://books.google.co.uk/books?id=majyAAAACAAJ>.
- [33] M.H. Mulazimoglu, A. Zaluska, J.E. Gruzleski, F. Paray, Electron microscope study of Al-Fe-Si intermetallics in 6201 aluminum alloy, *Metall. Mater. Trans. A Phys. Metall. Mater. Sci.* 27 (1996) 929–936.

<https://doi.org/10.1007/BF02649760>.
- [34] Y. Liu, M. Liu, L. Luo, J. Wang, C. Liu, The solidification behavior of AA2618 aluminum alloy and the influence of cooling rate, *Materials (Basel)*. 7 (2014) 7875–7890. <https://doi.org/10.3390/ma7127875>.
- [35] Y. Osawa, S. Takamori, T. Kimura, K. Minagawa, H. Kakisawa, Morphology of intermetallic compounds in Al-Si-Fe alloy and its control by ultrasonic

vibration, *Mater. Trans.* 48 (2007) 2467–2475.

<https://doi.org/10.2320/matertrans.F-MRA2007874>.

- [36] J. a Taylor, The Effect of Iron in Al-Si Casting Alloys, 35th Aust. Foundry Inst. Natl. Conf. (2004) 148–157.
- [37] S. Zajac, L.O. Gullman, A. Johansson, B. Bengtsson, Hot ductility of some Al-Mg-Si alloys, *Mater. Sci. Forum.* 217–222 (1996) 1193–1198.
<https://doi.org/10.4028/www.scientific.net/msf.217-222.1193>.
- [38] S.G. Irizalp, N. Saklakoglu, Effect of Fe-rich intermetallics on the microstructure and mechanical properties of thixoformed A380 aluminum alloy, *Eng. Sci. Technol. an Int. J.* 17 (2014) 58–62.
<https://doi.org/10.1016/j.jestch.2014.03.006>.
- [39] S.G. Shabestari, M.M. Tavakoli, M. Ghanbari, Effect of semi-solid processing on iron-bearing intermetallic compounds in A380 aluminum alloy, *Solid State Phenom.* 217–218 (2014) 397–404.
<https://doi.org/10.4028/www.scientific.net/SSP.217-218.397>.
- [40] S. Shivkumar, S. Ricci, C. Keller, D. Apelian, Effect of solution treatment parameters on tensile properties of cast aluminum alloys, *J. Heat Treat.* 8 (1990) 63–70. <https://doi.org/10.1007/BF02833067>.
- [41] T.O. Mbuya, B.O. Odera, S.P. Ng’ang’a, Influence of iron on castability and properties of aluminium silicon alloys: Literature review, *Int. J. Cast Met. Res.* 16 (2003) 451–465. <https://doi.org/10.1080/13640461.2003.11819622>.
- [42] Q. Han, H. Xu, Fluidity of alloys under high pressure die casting conditions, *Scr. Mater.* 53 (2005) 7–10. <https://doi.org/10.1016/j.scriptamat.2005.03.025>.
- [43] M. Di Sabatino, L. Arnberg, S. Rørvik, A. Prestmo, The influence of oxide inclusions on the fluidity of Al-7 wt% Si alloy, *Mater. Sci. Eng. A.* 413–414 (2005) 272–276. <https://doi.org/10.1016/j.msea.2005.08.175>.

- [44] E. Taghaddos, M.M. Hejazi, R. Taghiabadi, S.G. Shabestari, Effect of iron-intermetallics on the fluidity of 413 aluminum alloy, *J. Alloys Compd.* 468 (2009) 539–545. <https://doi.org/10.1016/j.jallcom.2008.01.079>.
- [45] J.A. Taylor, G.B. Schaffer, D.H. Stjohn, The role of iron in the formation of porosity in Al-Si-Cu-based casting alloys: Part III. A microstructural model, *Metall. Mater. Trans. A Phys. Metall. Mater. Sci.* 30 (1999) 1657–1662. <https://doi.org/10.1007/s11661-999-0103-z>.
- [46] N. Roy, A.M. Samuel, F.H. Samuel, Porosity formation in Al-9 wt% Si-3 wt% Cu alloy systems: Metallographic observations, *Metall. Mater. Trans. A Phys. Metall. Mater. Sci.* 27 (1996) 415–429. <https://doi.org/10.1007/BF02648419>.
- [47] M. Dash, M. Makhlof, Effect of key alloying elements on the feeding characteristics of aluminum-silicon casting alloys, *J. Light Met.* 1 (2001) 251–265. [https://doi.org/10.1016/S1471-5317\(02\)00002-0](https://doi.org/10.1016/S1471-5317(02)00002-0).
- [48] M.M. Haque, A.F. Ismail, Effect of superheating temperatures on microstructure and properties of strontium modified aluminium-silicon eutectic alloy, *J. Mater. Process. Technol.* 162–163 (2005) 312–316. <https://doi.org/10.1016/j.jmatprotec.2005.02.049>.
- [49] L.A. Narayanan, F.H. Samuel, J.E. Gruzleski, Crystallization behavior of iron-containing intermetallic compounds in 319 aluminium alloy, *Met. Mat. Trans. A.* 25 (1994) 1761–1773. <https://doi.org/10.1007/BF02668540>.
- [50] R. Ahmadi, R.I. Marshall, Effect of superheating on iron-rich plate-type compounds in aluminium-silicon alloys, *Int. J. Cast Met. Res.* 15 (2003) 497–504. <https://doi.org/10.1080/13640461.2003.11819535>.
- [51] L. Zhang, J. Gao, L.N.W. Damao, D.G. Robertson, Removal of iron from aluminum: A review, *Miner. Process. Extr. Metall. Rev.* 33 (2012) 99–157. <https://doi.org/10.1080/08827508.2010.542211>.
- [52] M. Ravi, U.T.S. Pillai, B.C. Pai, A.D. Damodaran, E.S. Dwarakadasa, Mechanical properties of cast Al-7Si-0.3Mg (LM 25/356) alloy, *Int. J. Cast Met. Res.* 11

(1998) 113–125. <https://doi.org/10.1080/13640461.1998.11819265>.

- [53] A. Flores, J.C. Escobedo, M. Mendez, J. Mendez, Kinetics of the Formation, Growth, and Sedimentation of the $\text{Al}_{15}(\text{Fe}, \text{Mn})_3\text{Si}_2$ Phase in Al–Si–Cu Alloys, in: Trans. 16 Th Int. Die Cast. Congr. Expo., 1991: pp. 293–297.
- [54] S.G. Shabestari, J.E. Gruzleski, The Effect of Solidification Condition and Chemistry on the Formation and Morphology of Complex Intermetallic Compounds in Aluminium–Silicon Alloys, Cast Met. 6 (1994) 217–224. <https://doi.org/10.1080/09534962.1994.11819153>.
- [55] A. Couture, Iron in aluminum casting alloys-a literature survey, Int. Cast Met. J. 6 (1981) 9–17.
- [56] S. Murali, K.S. Raman, K.S.S. Murthy, Effect of trace additions (Be, Cr, Mn and Co) on the mechanical properties and fracture toughness of Fe-containing Al-7Si-0.3 Mg alloy, Cast Met. 6 (1994) 189–198.
- [57] K.G. Wickle, K. Bery, Improving Aluminum Castings with Beryllium, in: 82nd Annu. Meet. Am. Foundrymen's Soc., 1978.
- [58] Y. Wang, Y. Xiong, Effects of beryllium in Al-Si-Mg-Ti cast alloy, Mater. Sci. Eng. A. 280 (2000) 124–127. [https://doi.org/10.1016/S0921-5093\(99\)00677-2](https://doi.org/10.1016/S0921-5093(99)00677-2).
- [59] Y.H. Tan, S.L. Lee, H.Y. Wu, Effects of beryllium on fatigue crack propagation of A357 alloys containing iron, Int. J. Fatigue. 18 (1996) 137–147. [https://doi.org/10.1016/0142-1123\(95\)00034-8](https://doi.org/10.1016/0142-1123(95)00034-8).
- [60] P.S. Warng, Y.J. Liauh, S.L. Lee, J.C. Lin, Effects of Be addition on microstructures and mechanical properties of B319.0 alloys, Mater. Chem. Phys. 53 (1998) 195–202. [https://doi.org/10.1016/s0254-0584\(98\)00007-8](https://doi.org/10.1016/s0254-0584(98)00007-8).
- [61] U. Patakham, J. Kajornchaiyakul, C. Limmaneevichitr, Grain refinement mechanism in an Al – Si – Mg alloy with scandium, J. Alloys Compd. 542 (2012) 177–186. <https://doi.org/10.1016/j.jallcom.2012.07.018>.
- [62] W. Prukkanon, N. Srisukhumbowornchai, C. Limmaneevichitr, Modification of

- hypoeutectic Al-Si alloys with scandium, *J. Alloys Compd.* 477 (2009) 454–460.
<https://doi.org/10.1016/j.jallcom.2008.10.016>.
- [63] U. Patakham, C. Limmaneevichitr, Effects of Iron on Intermetallic Compound Formation in Scandium Modified Al-Si-Mg Alloys, *J. Alloys Compd.* (2014).
<https://doi.org/10.1016/j.jallcom.2014.07.037>.
- [64] K. Chanyathunyaroj, U. Patakham, S. Kou, C. Limmaneevichitr, Microstructural evolution of iron-rich intermetallic compounds in scandium modified Al-7Si-0.3Mg alloys, *J. Alloys Compd.* 692 (2017) 865–875.
<https://doi.org/10.1016/j.jallcom.2016.09.132>.
- [65] J. Røyset, J.R. Leinum, H.G. Øverlie, O. Reiso, An investigation of the solubility of scandium in iron-bearing constituent particles in aluminium alloys, *Mater. Sci. Forum.* 519–521 (2006) 531–536.
<https://doi.org/10.4028/www.scientific.net/msf.519-521.531>.
- [66] A.M. Samuel, F.H. Samuel, S. Valtierra, Effect of Fe , Sr , P , Ti And Undercooling on the precipitation of β -Al₅FeSi in A319 . 2 type alloys, *Int. J. Met.* (2016).
<https://doi.org/10.1007/s40962-016-0116-5>.
- [67] A.M. Samuel, P. Ouellet, F.H. Samuel, H.W. Doty, Microstructural interpretation of thermal analysis of commercial 319 Al alloy with Mg and Sr additions, *Am. Foundrymen's Soc. Inc, Trans. Am. Foundrymen's Soc.* 105 (1998) 951–962.
- [68] A.M. Samuel, F.H. Samuel, Influence of oxides on porosity formation in Sr-treated alloys, *Int. J. Met.* (2016). <https://doi.org/10.1007/s40962-016-0118-3>.
- [69] P. Ashtari, H. Tezuka, T. Sato, Influence of Li addition on intermetallic compound morphologies in Al-Si-Cu-Fe cast alloys, *Scr. Mater.* 51 (2004) 43–46. <https://doi.org/10.1016/j.scriptamat.2004.03.022>.
- [70] M.F. Ibrahim, S.A. Alkahtani, K.A. Abuhasel, F.H. Samuel, Effect of

intermetallics on the microstructure and tensile properties of aluminum based alloys: Role of Sr, Mg and Be addition, *Mater. Des.* 86 (2015) 30–40. <https://doi.org/10.1016/j.matdes.2015.07.019>.

- [71] V.S. Zolotarevsky, A.A. Axenov, N.A. Belov, Neutralization of the negative influence of iron and silicon on the mechanical properties of aluminium casting alloys, *Mech. Corros. Prop. Ser. A, Key Eng. Mater.* 44–45 (1990) 347–363. <https://doi.org/10.4028/www.scientific.net/kem.44-45.347>.
- [72] M. Ravi, U.T.S. Pillai, B.C. Pai, A.D. Damodaran, E.S. Dwarakadasa, A study of the influence of mischmetal additions to Al-7Si-0.3Mg (LM 25/356) alloy, *Metall. Mater. Trans. A Phys. Metall. Mater. Sci.* 27 (1996) 1283–1292. <https://doi.org/10.1007/BF02649865>.
- [73] M. Ravi, U.T.S. Pillai, B.C. Pai, A.D. Damodaran, E.S. Dwarakadasa, The Effect of mischmetal Addition on the Structure and Mechanical Properties of a Cast Al-7Si-0.3Mg Alloy Containing Excess Iron (up to 0.6 Pct), *Metall. Mater. Trans. A.* 33 (2002) 391–400.
- [74] M. Hosseinifar, D. V. Malakhov, Effect of Ce and La on microstructure and properties of a 6xxx series type aluminum alloy, *J. Mater. Sci.* 43 (2008) 7157–7164. <https://doi.org/10.1007/s10853-008-3022-2>.
- [75] M. Hosseinifar, D. V. Malakhov, The sequence of intermetallics formation during the solidification of an Al-Mg-Si alloy containing La, *Metall. Mater. Trans. A Phys. Metall. Mater. Sci.* 42 (2011) 825–833. <https://doi.org/10.1007/s11661-010-0453-6>.
- [76] E.M. Elgallad, M.F. Ibrahim, H.W. Doty, F.H. Samuel, Microstructural characterisation of Al–Si cast alloys containing rare earth additions, *Philos. Mag.* 98 (2018) 1337–1359. <https://doi.org/10.1080/14786435.2018.1435917>.
- [77] D. Li, C. Cui, X. Wang, Q. Wang, C. Chen, S. Liu, Microstructure evolution and enhanced mechanical properties of eutectic Al–Si die cast alloy by combined

alloying Mg and La, Mater. Des. 90 (2016) 820–828.

<https://doi.org/10.1016/j.matdes.2015.10.078>.

- [78] W.C. Oliver, G.M. Pharr, Measurement of hardness and elastic modulus by instrumented indentation: Advances in understanding and refinements to methodology, J. Mater. Res. 19 (2004) 3–20.

<https://doi.org/10.1557/jmr.2004.19.1.3>.
- [79] W.C. Oliver, G.M. Pharr, An improved technique for determining hardness and elastic modulus using load and displacement sensing indentation experiments, J. Mater. Res. 7 (1992) 1564–1583. <https://doi.org/10.1557/JMR.1992.1564>.
- [80] E. Frutos, D.G. Morris, M.A. Muñoz-Morris, Evaluation of elastic modulus and hardness of Fe-Al base intermetallics by nano-indentation techniques, Intermetallics. 38 (2013) 1–3.

<https://doi.org/10.1016/j.intermet.2013.02.012>.
- [81] M. Zamanzade, H. Vehoff, A. Barnoush, Effect of chromium on elastic and plastic deformation of Fe₃Al intermetallics, Intermetallics. 41 (2013) 28–34. <https://doi.org/10.1016/j.intermet.2013.04.013>.
- [82] K.M. Mussert, A nano-indentation study on the mechanical behaviour of the matrix material in an AA6061 -Al₂O₃ MMC, J. Mater. Sci. 37 (2002) 789–794. <https://doi.org/10.1023/A:1013896032331>.
- [83] ASTM Int., Standard Test Methods for Tension Testing of Metallic Materials 1, Astm. (2009) 1–27. <https://doi.org/10.1520/E0008>.
- [84] S. Shankar, Y.W. Riddle, M.M. Makhlof, Nucleation mechanism of the eutectic phases in aluminum-silicon hypoeutectic alloys, Acta Mater. 52 (2004) 4447–4460. <https://doi.org/10.1016/j.actamat.2004.05.045>.
- [85] S. Hegde, K.N. Prabhu, Modification of eutectic silicon in Al-Si alloys, J. Mater. Sci. 43 (2008) 3009–3027. <https://doi.org/10.1007/s10853-008-2505-5>.

- [86] C.L. Chen, A. Richter, R.C. Thomson, Mechanical properties of intermetallic phases in multi-component Al-Si alloys using nanoindentation, *Intermetallics*. 17 (2009) 634–641. <https://doi.org/10.1016/j.intermet.2009.02.003>.
- [87] S.W. Youn, P.K. Seo, C.G. Kang, A study on nano-deformation behavior of rheo-formed Al-Si alloy based on depth-sensing indentation with three-dimensional surface analysis, *J. Mater. Process. Technol.* 162–163 (2005) 260–266. <https://doi.org/10.1016/j.jmatprotec.2005.02.026>.
- [88] M. Sacinti, E. Cubuklusu, Y. Birol, Effect of iron on microstructure and mechanical properties of primary AlSi7Mg0.3 alloy, *Int. J. Cast Met. Res.* 30 (2017) 96–102. <https://doi.org/10.1080/13640461.2016.1250035>.
- [89] M. Ravi, U.T.S. Pillai, B.C. Pai, A.D. Damodaran, E.S. Dwarakadasa, Mechanical properties of cast Al-7Si-0.3Mg (LM 25/356) alloy, *Int. J. Cast Met. Res.* 11 (1998) 113–125. <https://doi.org/10.1080/13640461.1998.11819265>.
- [90] J.Z. Yi, Y.X. Gao, P.D. Lee, T.C. Lindley, Effect of Fe-content on fatigue crack initiation and propagation in a cast aluminum-silicon alloy (A356-T6), *Mater. Sci. Eng. A*. 386 (2004) 396–407. <https://doi.org/10.1016/j.msea.2004.07.044>.
- [91] K. Gall, N. Yang, M. Horstemeyer, D.L. McDowell, J. Fan, The debonding and fracture of Si particles during the fatigue of a cast Al-Si alloy, *Metall. Mater. Trans. A Phys. Metall. Mater. Sci.* 30 (1999) 3079–3088.

<https://doi.org/10.1007/s11661-999-0218-2>.
- [92] F. Wang, Z. Zhang, Y. Ma, Y. Jin, Effect of Fe and Mn additions on microstructure and wear properties of spray-deposited Al-20Si alloy, *Mater. Lett.* 58 (2004) 2442–2446. <https://doi.org/10.1016/j.matlet.2004.02.027>.
- [93] X. Cao, J. Campbell, Effect of melt superheating on convection-free precipitation and sedimentation of primary α -Fe phase in liquid al-11.5Si-0.4Mg alloy, *Int. J. Cast Met. Res.* 15 (2003) 595–608. <https://doi.org/10.1080/13640461.2003.11819546>.
- [94] S.G. Shabestari, M. Mahmudi, M. Emamy, J. Campbell, Effect of Mn and Sr on

- intermetallics in Fe-rich eutectic Al-Si alloy, *Int. J. Cast Met. Res.* 15 (2002) 17–24. <https://doi.org/10.1080/13640461.2002.11819459>.
- [95] F.H. Samuel, A.M. Samuel, H.W. Doty, S. Valtierra, Decomposition of Fe-intermetallics in Sr-modified cast 6XXX type aluminum alloys for automotive skin, *Metall. Mater. Trans. A Phys. Metall. Mater. Sci.* 32 (2001) 2061–2075. <https://doi.org/10.1007/s11661-001-0018-9>.
- [96] J.M. Yu, N. Wanderka, G. Miehe, J. Banhart, Intermetallic phases in high purity Al-10Si-0.3Fe cast alloys with and without Sr modification studied by FIB tomography and TEM, *Intermetallics*. 72 (2016) 53–61. <https://doi.org/10.1016/j.intermet.2016.02.003>.
- [97] C.M. Dinnis, J.A. Taylor, A.K. Dahle, As-cast morphology of iron-intermetallics in Al-Si foundry alloys, *Scr. Mater.* 53 (2005) 955–958. <https://doi.org/10.1016/j.scriptamat.2005.06.028>.
- [98] M. De Giovanni, J.M. Warnett, M.A. Williams, P. Srirangam, 3D imaging and quantification of porosity and intermetallic particles in strontium modified Al-Si alloys, *J. Alloys Compd.* 727 (2017) 353–361. <https://doi.org/10.1016/j.jallcom.2017.08.146>.
- [99] L. Liu, A.M. Samuel, F.H. Samuel, H.W. Doty, S. Valtierra, Influence of oxides on porosity formation in Sr-treated Al-Si casting alloys, *J. Mater. Sci.* 38 (2003) 1255–1267. <https://doi.org/10.1023/A:1022870006721>.
- [100] S.S. Nayak, B.S. Murty, S.K. Pabi, Structure of nanocomposites of Al-Fe alloys prepared by mechanical alloying and rapid solidification processing, *Bull. Mater. Sci.* 31 (2008) 449–454. <https://doi.org/10.1007/s12034-008-0070-9>.
- [101] A. Griger, V. Stefaniay, Equilibrium and non-equilibrium intermetallic phases in Al-Fe and Al-Fe-Si alloys, *J. Mater. Sci.* 31 (1996) 6645–6652. <https://doi.org/10.1007/BF00356274>.
- [102] S.S. Nayak, H.J. Chang, D.H. Kim, S.K. Pabi, B.S. Murty, Formation of metastable phases and nanocomposite structures in rapidly solidified Al-Fe alloys, *Mater.*

Sci. Eng. A. 528 (2011) 5967–5973.

<https://doi.org/10.1016/j.msea.2011.04.028>.

- [103] G. Li, X. Bian, K. Song, J. Guo, X. Li, C. Wang, Effect of Si addition on glass forming ability and thermal stability of Al-Fe-La alloys, *J. Alloys Compd.* 471 (2009) 1–4. <https://doi.org/10.1016/j.jallcom.2008.04.011>.
- [104] B. Liu, Q. Yang, Y. Wang, Interaction and intermetallic phase formation between aluminum and stainless steel, *Results Phys.* 12 (2019) 514–524. <https://doi.org/10.1016/j.rinp.2018.11.076>.
- [105] S.X. Luo, Z.M. Shi, N.Y. Li, Y.M. Lin, Y.H. Liang, Y.D. Zeng, Crystallization inhibition and microstructure refinement of Al-5Fe alloys by addition of rare earth elements, *J. Alloys Compd.* 789 (2019) 90–99. <https://doi.org/10.1016/j.jallcom.2019.03.071>.
- [106] Y.H. Liang, Z.M. Shi, G.W. Li, R.Y. Zhang, G. Zhao, Effects of Er addition on the crystallization characteristic and microstructure of Al-2 wt% Fe cast alloy, *J. Alloys Compd.* 781 (2019) 235–244. <https://doi.org/10.1016/j.jallcom.2018.12.063>.
- [107] H. Springer, A. Kostka, E.J. Payton, D. Raabe, A. Kaysser-pyzalla, G. Eggeler, On the formation and growth of intermetallic phases during interdiffusion between low-carbon steel and aluminum alloys, *Acta Mater.* 59 (2011) 1586–1600. <https://doi.org/10.1016/j.actamat.2010.11.023>.
- [108] M. Krasnowski, T. Kulik, Nanocrystalline and amorphous Al-Fe alloys containing 60-85% of Al synthesised by mechanical alloying and phase transformations induced by heating of milling products, *Mater. Chem. Phys.* 116 (2009) 631–637. <https://doi.org/10.1016/j.matchemphys.2009.05.003>.
- [109] S.S. Nayak, H.J. Chang, D.H. Kim, S.K. Pabi, B.S. Murty, Formation of metastable phases and nanocomposite structures in rapidly solidified Al-Fe alloys, *Mater. Sci. Eng. A.* 528 (2011) 5967–5973.

<https://doi.org/10.1016/j.msea.2011.04.028>.

- [110] M. Abbasi, M. Dehghani, H. Guim, D. Kim, Investigation of Fe-rich fragments in aluminum-steel friction stir welds via simultaneous Transmission Kikuchi Diffraction and EDS, *Acta Mater.* 117 (2016) 262–269.
- [111] F.C. Yin, M.X. Zhao, Y.X. Liu, W. Han, Z. Li, Effect of Si on growth kinetics of intermetallic compounds during reaction between solid iron and molten aluminum, *Trans. Nonferrous Met. Soc. China (English Ed.)* 23 (2013) 556–561. [https://doi.org/10.1016/S1003-6326\(13\)62499-1](https://doi.org/10.1016/S1003-6326(13)62499-1).
- [112] G. Pasche, M. Scheel, R. Schäublin, C. Hébert, M. Rappaz, A. Hessler-Wyser, Time-resolved X-ray microtomography observation of intermetallic formation between solid Fe and liquid Al, *Metall. Mater. Trans. A Phys. Metall. Mater. Sci.* 44 (2013) 4119–4123. <https://doi.org/10.1007/s11661-013-1788-6>.
- [113] A. Griebel, Technical brief: Fatigue dimples, *J. Fail. Anal. Prev.* 9 (2009) 193–196. <https://doi.org/10.1007/s11668-009-9228-z>.
- [114] V. Stefániay, A. Griger, T. Turmezey, Intermetallic phases in the aluminium-side corner of the AlFeSi-alloy system, *J. Mater. Sci.* 22 (1987) 539–546. <https://doi.org/10.1007/BF01160766>.
- [115] C. Puncreobutr, A.B. Phillion, J.L. Fife, P. Rockett, A.P. Horsfield, P.D. Lee, In situ quantification of the nucleation and growth of Fe-rich intermetallics during Al alloy solidification, *Acta Mater.* 79 (2014) 292–303. <https://doi.org/10.1016/j.actamat.2014.07.018>.
- [116] Current prices of base metals | Institute of Rare Earths and Strategic Metals eV, (n.d.). <https://en.institut-seltene-erden.de/current-prices-of-base-metals/>(accessed July 11, 2020).
- [117] Current prices for rare earths | Institute of Rare Earths and Strategic Metals eV, (n.d.). <https://en.institut-seltene-erden.de/aktuelle-preise-von-seltenen-erden/>(accessed July 11, 2020).
- [118] I.S. Sen, B. Peucker-Ehrenbrink, Anthropogenic disturbance of element cycles

at the Earth's surface, *Environ. Sci. Technol.* 46 (2012) 8601–8609.
<https://doi.org/10.1021/es301261x>.

- [119] Y. Yu, L. Yu, K.Y. Koh, C. Wang, J.P. Chen, Rare-earth metal based adsorbents for effective removal of arsenic from water: A critical review, *Crit. Rev. Environ. Sci. Technol.* 48 (2018) 1127–1164.

<https://doi.org/10.1080/10643389.2018.1514930>.

- [120] X. Yang, D. Ding, Y. Xu, W. Zhang, Y. Gao, Z. Wu, G. Chen, R. Chen, Y. Huang, J. Tang, Al–Fe–Si–La alloys for current collectors of positive electrodes in lithium ion batteries, *Metals (Basel)*. 10 (2020) 1–10.

<https://doi.org/10.3390/met10010109>.

- [121] N.D. Bakhteeva, E. V. Todorova, P.A. Volkov, A.L. Vasil'ev, Thermal stability of Al–Ni–Fe–La aluminum amorphous alloys, *Russ. Metall.* 2012 (2012) 404–414.
<https://doi.org/10.1134/S0036029512050035>.